Majorana Fermions in Mesoscopic Topological Superconductors: From Quantum Transport to Topological Quantum Computation

Inaugural-Dissertation

zur Erlangung des Doktorgrades
der Mathematisch-Naturwissenschaftlichen Fakultät
der Heinrich-Heine-Universität Düsseldorf

vorgelegt von

Stephan Plugge

aus Warstein

Düsseldorf, April 2018

Aus dem Institut für Theoretische Physik, Lehrstuhl IV
der Heinrich-Heine-Universität Düsseldorf

Gedruckt mit der Genehmigung der
Mathematisch-Naturwissenschaftlichen Fakultät
der Heinrich-Heine-Universität Düsseldorf

Berichterstatter:

1. Prof. Dr. Reinhold Egger
2. PD Dr. Hermann Kampermann
3. Prof. Felix von Oppen, PhD

Tag der mündlichen Prüfung: 15. Juni 2018

List of included publications

S. Plugge, A. Zazunov, P. Sodano, and R. Egger, *Majorana entanglement bridge*, Phys. Rev. B **91**, 214507 (2015). [Selected as *Editors' Suggestion*]

L.A. Landau, S. Plugge, E. Sela, A. Altland, S.M. Albrecht, and R. Egger, *Towards realistic implementations of a Majorana surface code*, Phys. Rev. Lett. **116**, 050501 (2016).

S. Plugge, A. Zazunov, E. Eriksson, A.M. Tsvelik, and R. Egger, *Kondo physics from quasiparticle poisoning in Majorana devices*, Phys. Rev. B **93**, 104524 (2016).

S. Plugge, L.A. Landau, E. Sela, A. Altland, K. Flensberg, and R. Egger, *Roadmap to Majorana surface codes*, Phys. Rev. B **94**, 174514 (2016). [Selected as *Editors' Suggestion*]

S. Plugge, A. Rasmussen, R. Egger, and K. Flensberg, *Majorana box qubits*, New J. Phys. **19** 012001 (2017). [Fast-Track Communication; selected for *Highlights of 2017* collection]

T. Karzig, C. Knapp, R. Lutchyn, P. Bonderson, M. Hastings, C. Nayak, J. Alicea, K. Flensberg, S. Plugge, Y. Oreg, C. Marcus, and M. H. Freedman, *Scalable Designs for Quasiparticle-Poisoning-Protected Topological Quantum Computation with Majorana Zero Modes*, Phys. Rev. B **95**, 235305 (2017). [Featured in *Physics*]

M. Sekania, S. Plugge, M. Greiter, R. Thomale, and P. Schmitteckert, *Braiding errors in interacting Majorana quantum wires*, Phys. Rev. B **96**, 094307 (2017).

M. Gau, S. Plugge, and R. Egger, *Quantum transport in coupled Majorana box systems*, Phys. Rev. B **97**, 184506 (2018). [Selected as *Editors' Suggestion*]

Abstract

In condensed-matter physics, Majorana fermions are realized as emergent quasi-particle excitations in the effective low-energy description of topological superconducting systems. Majorana bound states harbor much potential, both from a fundamental-physics viewpoint and for applications in quantum information processing, and their non-Abelian exchange statistics are fundamentally different from those of conventional fermions or bosons.

We start by introducing Majorana systems that afford the topologically protected storage and manipulation of quantum information. A braiding of Majorana fermions may reveal their hallmark non-Abelian statistics, and forms the basic operation that is crucial for applications in quantum information processing. We discuss both an ideal braid scenario and corrections to this toy model view for interacting Kitaev chains. Next, the inclusion of charging energy effects allows for charge transport to access the non-local character of Majorana bound states in mesoscopic topological superconductors. The relevant physics of charge conservation are captured by a simple capacitor model, and we investigate how entanglement spreads between quantum dots tunnel-coupled by such Majorana boxes. Phase-coherent transport in coupled Majorana box devices also facilitates the formation of strongly-correlated low-energy states in simply-coupled islands contacted by normal leads. We here explain core solution strategies for quantum transport phenomena in Majorana networks while reviewing the topological Kondo effect, followed by an investigation of multi-junction geometries that go beyond the simple junctions considered before. In the Majorana box and loop qubit devices that comprise basic hardware units towards quantum computing applications, simple conductance or spectroscopic measurements can be used to characterize the ensuing Majorana-based qubits. We then discuss fundamental concepts and requirements for quantum information processing, starting from single- and two-qubit operations all the way to large-scale and fault-tolerant quantum error correcting codes. An extension of our basal hardware units to small networks allows for measurement-based protected quantum computations with Majoranas, up to and including Clifford-complete code networks that can run arbitrary quantum error-correction protocols. A promising example for Majorana-based quantum error-correction is the Majorana surface code shown in the last part of this thesis. Finally, we give an outlook of the current experimental progress on phase-coherent Majorana networks, and mention interesting directions of future research.

Zusammenfassung

In der Festkörperphysik findet man Majorana-Fermionen als nieder-energetische Quasiteilchen in der effektiven Beschreibung von topologischen Supraleitern. Die hier realisierten Majorana-Zustände haben viele interessante Anwendungen, sowohl vom Blickpunkt fundamentaler Physik als auch in der Quanteninformationsverarbeitung. Ihre nicht-Abelsche Austauschstatistik unterscheidet sie grundlegend von normalen Fermionen oder Bosonen.

Wir beginnen mit einer Einleitung zu Majorana-Systemen, die eine topologisch geschützte Speicherung und Manipulation von Quantenzuständen ermöglichen. Durch den Austausch von Majorana-Fermionen kann man ihre nicht-Abelsche Statistik nachweisen, die für Anwendungen in Quanten-Computern grundlegend ist. Zur Veranschaulichung betrachten wir zuerst ideale Austauschprozesse, und diskutieren dann Korrekturen in realistischen Systemen. Als nächstes betrachten wir Majorana-Boxen mit endlicher Ladungsenergie, in denen Ladungstransport den nicht-lokalen Charakter von Majorana-Zuständen detektieren kann. Die relevante Physik in ladungserhaltenden Systemen kann durch einfache Kondensator-Modelle beschrieben werden. Durch korrelierten Ladungstransport kann so ein verschränkter Zustand in mehreren an die Box gekoppelten Quantenpunkten entstehen. Genauso erlaubt phasen-kohärentes Tunneln in Majorana-Boxen die Formation von korrelierten Niederenergie-Zuständen in normalleitenden Kontakten, die an das System gekoppelt sind. In diesem Zusammenhang erläutern wir allgemeine Lösungsstrategien für Quantentransportprobleme in Majorana-Netzwerken anhand des topologischen Kondo-Effekts, und gehen danach auf kompliziertere Kontakt-Geometrien ein. Majorana-Boxen und verwandte Systeme stellen grundlegende Bausteine für Majorana-basierte Quantenarchitekturen dar, in denen Transport- oder spektroskopische Messungen zur Charakterisierung von Quanten-Bits eingesetzt werden können. Hier diskutieren wir zuerst grundlegende Konzepte der Quanteninformationsverarbeitung, angefangen mit einzelnen oder kleinen Gruppen von Quanten-Bits bis hin zu skalierbaren Quantenfehler-korregierenden Kodes. Die Erweiterung einzelner System-Bausteine zu Netzwerken erlaubt dann eine Messungsbasiert geschütze Implementation von Quanten-Computern mit Majorana-Fermionen, bis hin zu Kode-Netzwerken die beliebige Protokolle zur Quantenfehler-Korrektur realisieren können. Ein vielversprechendes Beispiel für Majorana-basierte Quantenfehler-Korrektur ist der Majorana surface code, den wir im letzten Teil der Arbeit diskutieren. Zum Abschluss geben wir einen Ausblick auf aktuelle experimentelle Fortschritte zu phasen-kohärenten Majorana-Netzwerken, und erwähnen einige interessante zukünftige Forschungsrichtungen.

Contents

Chapter 1

Introduction

More than eighty years ago, the Italian physicists Majorana (1937) proposed to separate the complex equations of Dirac (1934) and Heisenberg (1934) into real and imaginary parts. What at first may seem like a mathematical exercise, indeed has profound implications for the quantum-mechanical particles described by Majoranas' and Diracs' equations. A single Dirac fermion with complex-valued wave function is split into *two* Majorana fermions with real wave functions. Among other things, this implies that Majorana fermions are their own anti-particle: taking the Hermitian adjoint of a Majorana operator gives back the same, and creation or annihilation of Majorana particles are equivalent physical processes. Consequently, if found at all, Majorana fermions should be charge-neutral and spin-less.

Aside from a few stints in particle physics, Majorana fermions (MFs) in form of Majorana bound states (MBSs) can arise as low-energy quasi-particles in condensed-matter systems. The topological superconductors (TSs) harboring such exotic particles in the past decades have become an active and rapidly progressing area of research. Read and Green (2000) showed that MBSs are hosted in vortices of p-wave superconductors, where electronic spin does not play a role and charge conservation is broken. The low-energy excitations of this system indeed are MFs, and Ivanov (2001) suggested that their non-Abelian exchange statistics – a hallmark feature of MFs – can be tested by moving and braiding vortices. Around the same time, Kitaev (2001) introduced his model for one-dimensional p-wave superconductors, where MBSs appear naturally and are hosted at the edges of a TS phase.

Following these developments, Fu and Kane (2008) showed how MBSs can be engineered as emergent quasi-particle excitations in the low-energy theory of hybrid semiconductor-superconductor systems. Soon thereafter, the ideas of Kitaev (2001) were extended to a concrete materials system by Oreg *et al.* (2010); Lutchyn *et al.* (2010). Rapid progress ensued, and an experimental observation of MBSs was reported in Mourik *et al.* (2012). The exponential ground-state degeneracy (Albrecht *et al.*, 2016) and resonant transport signatures (Nichele *et al.*, 2017; Zhang *et al.*, 2018) that are hallmarks of MBSs were subsequently observed, cf. the review by Lutchyn *et al.* (2017). Still, a conclusive braiding experiment (Ivanov, 2001; Alicea *et al.*, 2011; Aasen *et al.*, 2016), revealing the most interesting and crucial non-Abelian statistics of MFs, remains to be achieved.

The strong recent interest in Majorana bound states (MBSs) stems from their potential for quantum information processing applications. Freedman *et al.* (2003); Kitaev (2003) showed how anyons become useful tools for quantum computation, and related anyon fusion to the braiding of excitations in quantum error correcting codes, cf. Nayak *et al.* (2008). Beyond serving as protected quantum storage, adiabatic (Ivanov, 2001; Alicea *et al.*, 2011) or measurement-based braiding (Bonderson *et al.*, 2008a) of Majorana fermions allows to implement some quantum gates in a protected manner. The use of topological qubits then incites hope for a reduced overhead in quantum error correction compared to conventional-qubit implementations (Fowler *et al.*, 2012; Terhal, 2015). This may become a powerful tool on the long road towards large-scale, fault-tolerant and universal quantum computers.

Core parts of this work concern different levels of basic Majorana devices, Majorana-based qubits or code-network architectures. The thesis is organized in according topical blocks:

- In Chapter 2 we introduce how Majorana bound states can arise in condensed-matter systems. After an encoding of quantum information into Majorana fermions, braiding is used to manipulate the stored quantum states. Finally, mesoscopic Majorana boxes are topological superconductors with a large single-electron charging energy. Quantum dots coupled to this system become entangled due to the phase-coherent, non-local electron transport processes mediated by pairs of Majorana states.

- In Chapter 3 we analyze Majorana boxes coupled by normal-conducting leads. The phase-coherent tunneling of electrons generates strongly-correlated states in leads that reveal themselves in exotic low-energy physics, including unconventional Kondo effects and quantum transport resonances. Setups with multi-junctions of leads and Majorana bound states are instrumental to the operation of Majorana-based qubits.

- In Chapter 4 we engineer Majorana-based qubits and small-scale Majorana networks towards the realization of measurement-based topological quantum computation. Some of the few-qubit architectures we consider represent near-term experimental setups that already are realized in the lab. We then extend such Majorana networks to hardware platforms that are capable of running quantum error-correcting codes, i.e., that in principle can implement large-scale universal quantum computers.

- In Chapter 5 we summarize our contributions to quantum transport and computation in Majorana box systems. We review some of the recent experimental progress in this rapidly evolving field, and conclude with an outlook on interesting future research.

In each chapter, we give a short introduction to the concepts and technical aspects that are relevant to an understanding of our research. To this end, we review some relevant earlier works, and discuss an embedding of our results into the bigger scientific context. We then summarize our main contributions, and mention interesting ongoing research in the field. All eight publications that are included in this thesis can be found in the attachment.

Chapter 2

Majorana fermions in condensed matter and quantum information

In this Chapter we give a basic introduction to Majorana fermions in condensed-matter systems and their potential for quantum-information processing applications. Rather than providing an exhaustive overview of this manifold and rapidly progressing field, we here focus on the most important aspects towards a self-contained understanding of this thesis.

As starter, in Sec. 2.1 we discuss a simple lattice Hamiltonian introduced by Kitaev (2001) in one of his many seminal works. The *Kitaev chain* harbors two distinct physical phases which are conveniently described through the introduction of Majorana fermions (MFs). We then explain how quantum information is encoded in Majorana zero-modes (MZMs), and how one can represent MFs by sets of Pauli operators in Sec. 2.2. Following works of Ivanov (2001); Alicea *et al.* (2011), in Sec. 2.3 we discuss how braiding of MFs – one of the hallmark features of these exotic particles – can be understood in the context of quantum-information processing (QIP). We here also review our investigation Sekania *et al.* (2017) of braiding in *interacting* Kitaev chain systems. Finally, in Sec. 2.4 we introduce a toy-model description of mesoscopic topological superconductors, cf. Fu (2010); Hützen *et al.* (2012). Phase-coherent electron transport through such *Majorana islands* allows for generation of correlations and entanglement between quantum dots, cf. Sec. 2.4.2, a system hence dubbed *Majorana entanglement bridge* in Plugge *et al.* (2015). In Sec. 2.5, we conclude with a short summary of results that are most important for later parts of the thesis.
As we will see, phase-coherent tunneling also facilitates the formation of strongly-correlated states in leads attached to multi-terminal Majorana islands. Such scenarios are subject of Chapter 3, where the presence of MZMs on the island has profound influences on the low-energy and quantum transport behavior of the system. Further, quantum dots and leads coupled to Majorana islands are of strong interest in recent proposals for Majorana-based topological qubits and QIP-schemes, some of which are reviewed in Chapter 4.

For much of this chapter, we follow reviews by Alicea (2012); Leijnse and Flensberg (2012b); Beenakker (2013) and the excellent online course by TU Delft *et al.* (2018).

2.1 A toy model for topological superconductors

Following Kitaev (2001) and the review by Alicea (2012), the second-quantized Hamiltonian of a 1D spinless p-wave superconductor described by an N-site Kitaev chain is given as

$$H_{\text{chain}} = -\sum_{j=1}^{N} \mu_j c_j^\dagger c_j - \sum_{j=1}^{N-1} \left(t c_{j+1}^\dagger c_j + \Delta e^{i\phi} c_{j+1} c_j + \text{h.c.} \right) \ . \tag{2.1}$$

Here μ_j is a chemical potential controlling the occupation $n_j = c_j^\dagger c_j$ of site j, where the position-dependence of this parameter is a handle to control the system. Hopping and pairing of electrons along the chain is described by a nearest-neighbor hopping amplitude t and p-wave superconducting pairing strength Δ with phase ϕ. While anisotropies in both hopping and pairing parameters can be easily included, we assume them to be uniform and positive along the chain, $t \geq 0$ and $\Delta \geq 0$. In order to access the physics of this system, it is convenient to introduce two Majorana fermion (MF) operators $\gamma_{A,j}$ and $\gamma_{B,j}$ per lattice site j by writing

$$c_j = \frac{e^{-i\phi/2}}{2} (\gamma_{B,j} + i\gamma_{A,j}) \ , \tag{2.2}$$

and conversely

$$\gamma_{B,j} = e^{i\phi/2} c_j + e^{-i\phi/2} c_j^\dagger \quad , \quad \gamma_{A,j} = -i \left(e^{i\phi/2} c_j - e^{-i\phi/2} c_j^\dagger \right) \ . \tag{2.3}$$

Since the original fermion operators c_j and $c_j^\dagger$ fulfill the Dirac fermion algebra, $\{c_i, c_j^\dagger\} = \delta_{ij}$, it is easy to check that the Majorana operators fulfill a Clifford algebra, $\{\gamma_i, \gamma_j\} = 2\delta_{ij}$. This implies $\gamma_j^2 = 1$, and we obtain the defining self-adjoint property $\gamma_j = \gamma_j^\dagger$ of a MF (operator); MFs are their own anti-particles (Majorana, 1937), and creation or annihilation describe the same physical processes. Writing the Kitaev chain Hamiltonian H_{chain} in Eq. (2.1) in MF representation, we find (up to a constant)

$$H_{\text{chain}} = \frac{1}{2} \sum_{j=1}^{N} \mu_j (i\gamma_{A,j}\gamma_{B,j}) - \frac{1}{2} \sum_{j=1}^{N-1} \left[\Delta_+ (i\gamma_{B,j}\gamma_{A,j+1}) - \Delta_- (i\gamma_{A,j}\gamma_{B,j+1}) \right] \ , \tag{2.4}$$

with $\Delta_\pm = t \pm \Delta$. The decomposition of fermion sites into MFs with different pairings is shown and discussed in Fig. 2.1 below. MF parity-pairs have eigenvalues ± 1, as seen by reinserting a complex-fermion representation, $i\gamma_{A,j}\gamma_{B,j} = 1 - 2c_j^\dagger c_j = 1 - 2n_j$ with $n_j = 0,\ 1$.

Contributions $\sim \mu_j,\ \Delta_\pm$ in Eq. (2.4) favor different types of MF pairing. After recombining MFs to complex fermions, these correspond to the differing suitable eigenbases of the problem, depending on which pairing terms dominate. It is instructive to consider two limiting cases of the Kitaev chain that describe physically distinct phases. First, in the absence of hopping- or pairing-terms, $\Delta_\pm = 0$, with chemical potential $\mu_j = \mu$ we find

$$H'_{\text{chain}} = \frac{1}{2} \mu \sum_{j=1}^{N} (i\gamma_{A,j}\gamma_{B,j}) \simeq -\mu \sum_{j=1}^{N} c_j^\dagger c_j \ . \tag{2.5}$$

Negative chemical potential ($\mu < 0$) now penalizes occupation of the original fermion sites. The ground state of the chain then is identified with fermion occupation numbers $n_j = 0$, i.e., with the locally paired even fermion-parity state, $i\gamma_{A,j}\gamma_{B,j} = +$ for $j = 1, ..., N$.
A drastically different state is realized at zero chemical potential, $\mu_j = 0$, with equal hopping- and pairing-strengths $\Delta = t$, translating to $\Delta_+ = 2t$ and $\Delta_- = 0$. We note

$$H''_{\text{chain}} = -t\sum_{j=1}^{N-1}(i\gamma_{B,j}\gamma_{A,j+1}) \simeq 2t\sum_{j=1}^{N-1} d_j^\dagger d_j \ . \tag{2.6}$$

This situation is shown in the left part of Fig. 2.1. Importantly, only $N-1$ fermion-parity pairs appear in the Hamiltonian, identified with the shifted fermion operators $d_j = (\gamma_{A,j+1} + i\gamma_{B,j})/2$. These reflect non-local pairing in terms of the original sites of the chain, and occupation of each state costs energy $2t$, where the ground state has $n_{d,j} = 0$ for $j = 1, ..., N-1$. A single fermion state $f = (\gamma_{B,N} + i\gamma_{A,1})/2$ can either be occupied or empty, $i\gamma_{A,1}\gamma_{B,N} = \pm$ with corresponding states $|0_f\rangle$ and $|1_f\rangle$, at no additional energy cost. This state is maximally nonlocal in that it contains one MF $\gamma_{A,1}$ from the first, and one MF $\gamma_{B,N}$ from the last site of the chain.
Non-locality and the fractionalization of fermionic states into MFs allows for protection of Majorana-based qubits against decoherence. However, the Majorana non-locality also makes it difficult to access and manipulate Majorana systems, as discussed extensively in Sec. 2.4 and Chapters 3 and 4. Any physical process affecting the combined fermionic state $|n_f\rangle$ has to act on the system in a non-local fashion, where Hamiltonian-level terms $\sim f^{(\dagger)}$ imply a coupling both to first and last sites in the original local-fermion basis.

We denote phases with or without Majorana edge states as topological and (topologically) trivial, or *topological superconductor* (TS) and trivial superconductor, respectively. Here the latter phase, even if pairing $\Delta_\pm \neq 0$ is active, for large enough $\mu \to -\infty$ is directly connected to the (trivial) vacuum with $n_{j=1,...,N} = 0$. In contrast, in the topological phase the existence of Majorana edge states $\gamma_{A,1}$ and $\gamma_{B,N}$ depends only on the presence of boundaries/edges in the system (i.e., on its topology). To this end, consider deformation of the chain to a ring with site $j = N+1 \equiv 1$. We introduce additional MF pairings as

$$H_{\text{ring}} = H_{\text{chain}} - \frac{1}{2}\left[\bar{\Delta}_+(i\gamma_{B,N}\gamma_{A,1}) - \bar{\Delta}_-(i\gamma_{A,N}\gamma_{B,1})\right] \ . \tag{2.7}$$

For $\bar{\Delta} = \bar{t}$, with $\bar{\Delta}_+ = 2\bar{t}$ and $\bar{\Delta}_- = 0$, these terms gap the previously non-local fermion-parity pair $i\gamma_{B,N}\gamma_{A,1} = \pm$ in H''_{chain}, leaving no free Majoranas in the system. Instead choosing $\bar{t} = -\bar{\Delta}$, with $\bar{\Delta}_- = -2\bar{t}$ (and $\bar{\Delta}_+ = 0$), corresponds to anti-periodic boundary conditions identified with the insertion of a virtual flux π in the Kitaev ring. (Imagine an electron tunneling once around the ring – it experiences a phase-shift π upon crossing the final link with coupling $t_{1,N} = -\bar{t}$). In this case the Majorana pair $i\gamma_{B,N}\gamma_{A,1}$ remains free.

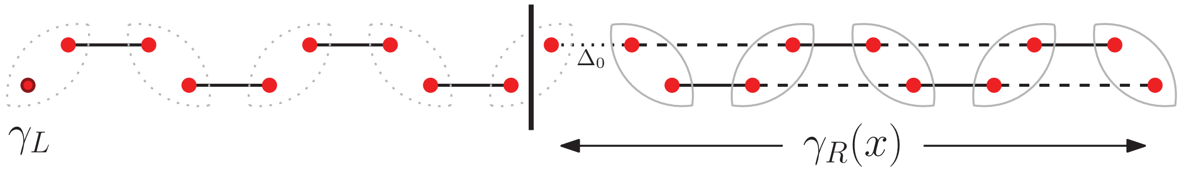

Figure 2.1: Kitaev chain system with anisotropic couplings, cf. Eqs. (2.4) and (2.8). On each original fermion site (ovals), left and right MFs are of A- and B-type, respectively. Dotted (solid) ovals indicate absence (presence) of chemical potentials that favor local MF pairing. Solid and dashed lines denote inter-site Majorana pairings $\Delta_\pm$. In the left part (separated by vertical bold line), strong pairing Δ_+ leaves behind one localized MZM γ_L. The right side then contains 11 MFs in Eq. (2.8), where a single MZM $\gamma_R(x)$ is localized somewhere along the right chain, depending on pairings $\Delta_\pm$ and chemical potentials μ_x.

2.1.1 About the localization of Majorana bound states

In this section, we discuss the localization of Majorana bound states (MBSs) in Kitaev chains, and how it is affected by non-ideal parameter settings, i.e., taking $\mu_j \neq 0$ and $t \neq \Delta$ in Sec. 2.1. From there we also learn about the nature of the trivial-topological phase transition, and how to manipulate the position of Majoranas in these systems, e.g., via chemical-potential manipulation protocols $\mu_j \to \mu_j(t)$. Ultimately this allows us to braid MFs through sequential manipulations of local parameters, see Section 2.3 below.

Consider a Kitaev chain with sites $j' = -N', ..., 0$ (left) and $j = 1, ..., N$ (right) in H_{chain}, cf. Eq. (2.4) and Fig. 2.1. The left part is at the Kitaev point with $\mu_{j'} = 0$, $\Delta'_+ = 2t'$ and $\Delta'_- = 0$, whereby all its Majorana pairs are frozen out into the even-parity state, $i\gamma_{B,j'}\gamma_{A,j'+1} = +$ at $j' < 0$. Any excitation in the left chain then costs energy $2t'$ apart from the free MF $\gamma_{A,-N'} \equiv \gamma_L$ at the boundary, and we have a single central Majorana $\gamma_{B,0}$ coupling to the right chain at $j > 0$, cf. Fig. 2.1. This system is described by

$$H_{2\text{ch}} = -\frac{\Delta_0}{2}(i\gamma_{B,0}\gamma_{A,1}) + \frac{1}{2}\sum_{j=1}^{N}\mu_j(i\gamma_{A,j}\gamma_{B,j}) - \frac{1}{2}\sum_{j=1}^{N-1}[\Delta_+(i\gamma_{B,j}\gamma_{A,j+1}) - \Delta_-(i\gamma_{A,j}\gamma_{B,j+1})] \ . \tag{2.8}$$

We now are interested in the physics and localization of the rightmost free MF $\gamma_R(x)$. Because there is a free MF γ_L at the left end of the chain, and since we are dealing with a finite system, there must exists such a mode that is localized at zero energy, i.e., it commutes with the Hamiltonian, $[H_{2\text{ch}}, \gamma_R(x)]_- = 0$. Alternatively, observe that the reduced Hamiltonian above contains an odd number of MFs (exactly $2N + 1$).
The right, non-ideal Majorana operator $\gamma_R(x)$ can be constructed following Fendley (2012). We start with a guess, e.g. $\gamma_R^{(0)}(x) = \gamma_{B,0}$ representing the Majorana zero-mode (MZM) at $\Delta_0 = 0$ (decoupled chains), and then iteratively add corrections $\gamma_R^{(1)}(x) = \gamma_{B,0} + \cdots$ that eliminate non-vanishing contributions in the commutator with $H_{2\text{ch}}$. Since γ_L is an A-type MF, the operator $\gamma_R(x)$ can have support only on B-type Majorana sites of the chain.

With the ansatz $\gamma_R(x) = \sum_{n=0}^{N} \beta_n \gamma_{B,n}$ and from $[H_{2\text{ch}}, \gamma_R(x)]_- = 0$, we find

$$\begin{aligned} 0 &= (\Delta_0\beta_0 + \mu_1\beta_1 + \Delta_-\beta_2)\,\gamma_{A,1} + (\mu_N\beta_N + \Delta_+\beta_{N-1})\,\gamma_{A,N} \\ &\quad + \sum_{n=2}^{N-1} (\mu_n\beta_n + \Delta_+\beta_{n-1} + \Delta_-\beta_{n+1})\,\gamma_{A,n} \end{aligned} \tag{2.9}$$

We here sorted contributions according to their A-type Majorana operator content. Since the operators $\gamma_{A,j}$ act on distinct local-fermion basis states $n_j = 0,\ 1$, from the N prefactors in Eq. (2.9), we obtain a recursive set of equations for the coefficients $\beta_{n=0,\ldots,N}$. With normalization $\gamma_R^2 = 1$, this recursion then fully determines the zero-mode operator $\gamma_R(x)$.

It now is instructive to investigate two limiting cases. First, we consider a vanishing chemical potential also in the right chain ($\mu_j = 0$). Taking $\Delta_0 \equiv \Delta_+$, we obtain

$$\beta_k = \left(-\frac{\Delta_-}{\Delta_+}\right)^{(N-k)/2} \beta_N \quad , \quad \text{for } k = N,\ N-2,\ \ldots\ , \tag{2.10}$$

and $\beta_{k-1} = 0$. The zero-mode operator has support on every second site of the chain, counting from the right-most site. With $\Delta_\pm = t \pm \Delta$, and taking $\Delta < t$, we find $\Delta_+ > \Delta_- > 0$. Coefficients β_k then constitute a decreasing series, and the support on the last site (β_N) becomes dominant for $\Delta \to t$ ($\Delta_- \to 0$). We can interpret this in terms of a topological phase that has extended across, where $\gamma_R(x) \to \gamma_{B,N}$ becomes (perfectly) localized as one approaches the Kitaev point for the full chain. The envelope of this series matches an exponential decay function $\sim e^{-x/\xi}$, with MBS localization length ξ. The latter often is used to quantify the protection and residual overlaps of near-localized MBSs in topological phases. With distance $x = N - k$ from the right end of the chain, one finds $\xi = 1/\ln\sqrt{\Delta_+/\Delta_-}$ in Eq. (2.10), which correctly gives perfect localization ($\xi \to 0$) at the Kitaev point $\Delta \to t$.

A π-shift of the sc phase ϕ is introduced by switching $\Delta \to -\Delta$ from middle to right end, which implies $\Delta_\pm \to \Delta_\mp$ in Eqs. (2.9) and (2.10). With the new $\Delta_\pm$, one finds coefficients $\tilde{\beta}_{2m} = (-\Delta_-/\Delta_+)^m \beta_0$ that constitute a decreasing series at $m \geq 0$. The MBS $\gamma_R(x)$ then is located at site "0", with exponentially decaying tail into the right chain. By symmetry, also the right segment generates a set of MBSs γ_L' (at $x \approx 0$) and γ_R' (at the right end).

Chains with distinct pairing symmetries hence can host "accidental" MZMs at their junction that do not gap out. This situation is equivalent to that of the Kitaev ring under anti-periodic boundary conditions, cf. Eq. (2.7), where a pair of MFs remains gapless even though there is no (physical) boundary in the system. In this sense, the Kitaev chain hosts two distinct topological phases for $\Delta > 0$ and $\Delta < 0$. The phase-transition point at $\mu = 0$ is given by $|\Delta_+| = |\Delta_-|$, and for finite superconducting pairing $\Delta \neq 0$ (and hopping $t \neq 0$) one finds either of the topological phases with dominant $\Delta_\pm$-pairing.

Finally we consider a spatially varying chemical potential, as used in the Majorana braiding protocols of Sec. 2.3. With $\Delta = t$, we have $\Delta_+ = \Delta_0 = 2t$ and $\Delta_- = 0$ in Eq. (2.9), but now allow $\mu_x \neq 0$. With ansatz $\gamma_R(x) = \sum_{n\geq 0}^{N} \beta_n \gamma_{B,n}$, we find the series coefficients via

$$\beta_n = \prod_{j>0}^{n} \left(-\frac{\Delta_+}{\mu_j} \right) \beta_0 \quad , \quad n = 1, ..., N \ . \tag{2.11}$$

MZM $\gamma_R(x)$ now has finite operator support on all sites $n \geq 0$, again with sign-fluctuations between consecutive occupied sites. Taking isotropic $\mu_n = \mu$ yields $\beta_n = (-2t/\mu)^n \beta_0$, where the MZM γ_R is exponentially localized in the middle (at the right end) of the chain for $|\mu| > \mu_c = 2t$ (for $|\mu| < \mu_c$). Unlike before, for $|\mu| > \mu_c$ the right segment is not in a topological phase anymore, but rather experiences a trivial pairing connected to the case $\mu \to \pm\infty$, cf. Eq. (2.5) and discussion. We hence have identified the (full) phase diagram of the Kitaev chain with the interesting topological phase(s) at $|\mu| < 2t$ hosting MFs, cf. the reviews by Alicea (2012); Leijnse and Flensberg (2012b); Beenakker (2013).

Last, introducing a spatially varying chemical potential μ_x allows to localize the MZM $\gamma_R(x)$ in an arbitrary way in region $x \geq 0$ of the chain. In principle one may imprint a complicated spatial profile according to Eq. (2.11). We are more interested in simple cases and choose, e.g., a linear ramp $\mu_n \simeq \alpha\mu_c n$ with inclination $\alpha \ll 1$. The wave-function weights β_n in $\gamma_R(x)$ will increase up to the point $\mu_x = \mu_c$, up till where the factor $|\Delta_+/\mu_n| > 1$ is large. Afterwards, as $\mu_{n>x} > \mu_c$ drives the system out of the topological phase, the weights $\beta_{n>x}$ decline. Put together, we then observe a localization of the MZM around point $\mu_x \simeq \mu_c$. Taking a logarithm and switching to continuous variables $n, j \to x, x'$, for the envelope function of the prefactor in Eq. (2.11) we find

$$\ln\left(\beta(x)/\beta_0\right) \simeq -\int_0^x dx' \ln\left(\frac{\mu(x')}{\mu_c}\right) \ . \tag{2.12}$$

These weights are subject to normalization $\int_0^L dx[\beta(x)]^2 = 1$, with $L \equiv N$. As example, for the linear ramp $\mu(\tilde{x}') = \mu_c(1+\alpha\tilde{x}')$ one finds a super-exponential decay $\beta(\tilde{x}) \sim e^{-\alpha\tilde{x}^2/2}$. Here $\tilde{x} = x - \alpha^{-1}$ is measured from the phase transition point at $\mu(x = \alpha^{-1}) = \mu_c$.

We conclude by noting that slow (adiabatic) manipulations of chemical potentials should allow to shift around MBSs localized at distant points in Kitaev chains and networks. Since the MZM wave-functions are exponentially decaying into both the topological and trivially gapped regimes, moderate separations on scale of a few times the MBS localization length ξ should suffice to consider them as independent. We hence proceed to introduce their ideal-braiding properties in an independent single-particle picture below, cf. Sec. 2.3, where corrections to this toy-model view are discussed in our work Sekania *et al.* (2017).

2.2 Encoding qubits in Majorana zero-modes

Throughout this work, we extensively use the Majorana operator representation in both condensed-matter and quantum-information related context. A very helpful way to rephrase a system of $2N$ MFs is then not in terms of N complex fermions, see Sec. 2.1, but through N qubits with associated Pauli operators $\sigma_{a=x,y,z}^{n=1,...,N}$. In condensed-matter context, this way of rewriting complex fermions or MFs into Pauli operators is known as the Jordan-Wigner transformation (Altland and Simons, 2010). In group-theoretical terms, the rephrasing relies on realization of a $2N$-component real Majorana "spin" $\vec{S}$ with entries $S_{jk} = i\gamma_j\gamma_k$ that belongs to the special orthogonal group SO(M). What is used below is the spinor irreducible representation of the group SO(M) for even $M = 2N$ (Zee, 2016).
Evidently, this representation or *encoding* of N qubits in $2N$ MFs reproduces the correct Hilbert space dimension 2^N; the quantum dimension of Majorana operators is $\sqrt{2}$. As an additional bonus, in the spin- or qubit-language, often it is more familiar to deal with ambiguities of basis choice. There is no ad-hoc preferred way to pair the $2N$ MFs into fermion states or spins, since they all belong to the low-energy sector of the system.

We now make contact between MFs with their underlying Clifford algebra and a description via "conventional" qubits and qubit operators obeying a Pauli algebra. For Majoranas γ_j and Pauli operators σ_a^n, recall part of their respective Clifford and Pauli algebras as

$$\{\gamma_i, \gamma_j\} = \gamma_i\gamma_j + \gamma_j\gamma_i = 2\delta_{ij}I_2 \ , \quad \{\sigma_a^n, \sigma_b^m\} = 2\delta_{ab}\delta_{nm}I_2 \ . \tag{2.13}$$

Henceforth identity matrices $I_2 = \mathrm{diag}(1,1)$ are suppressed in our notation. We now start an iterative construction of the Pauli representation for Majorana operators. Because of anti-commutativity and since each Majorana should square to one, $\gamma_j^2 = 1$, we write

$$\gamma_1 = \sigma_x^1 \ , \quad \gamma_2 = \sigma_y^1 \ . \tag{2.14}$$

In order to anti-commute with γ_1 and γ_2, any further Majorana operators now have to contain σ_z^1. By analogy to the first two Majoranas above, we therefore continue as

$$\gamma_3 = \sigma_x^2\sigma_z^1 \ , \quad \gamma_4 = \sigma_y^2\sigma_z^1 \ . \tag{2.15}$$

Evidently these operators fulfill the Clifford algebra above. We hence identify the iterative structure of representation for Majorana operators as

$$\gamma_{2j-1} = \sigma_x^j \prod_{n<j} \sigma_z^n \ , \quad \gamma_{2j} = \sigma_y^j \prod_{n<j} \sigma_z^n \ , \qquad \text{for } j = 1, ..., N \ . \tag{2.16}$$

For each two Majoranas we have to add one additional set of Pauli operators, as expected on grounds of their Hilbert-space dimensions. We also observe that the chains of Pauli operators become increasingly non-local in terms of spins or fermion-sites as we keep adding Majorana fermions that are to be represented. Luckily, in many cases that are of interest below, there exist local fermion-parity constraints for Majorana operators,

$$\hat{\mathcal{P}}_m = \prod_{j=1}^{m} (i\gamma_{2j}\gamma_{2j-1}) = \prod_{j=1}^{m} \sigma_z^j \ , \tag{2.17}$$

such that the fermion parity $\mathcal{P}_m = \pm$ for a subgroup of Majoranas $\gamma_{j=1,\dots,2m}$ stays fixed. Physically, this implies that there is either an even or odd number of fermions hosted in the low-energy sector of the $2m$-Majorana subsystem (with $m \leq N$). A Hamiltonian obeying this constraint contains only terms that commute with $\hat{\mathcal{P}}_m$, which necessarily comprise an even number of operators $\gamma_{j=1,\dots,2m}$. For sites beyond this subsector, the extending strings of Pauli-z matrices in Eq. (2.16) then square out.
In general TS setups, fixing only the fermion parity but not the fermion number itself is warranted since pairs of electrons are freely (at zero energy cost) absorbed and emitted by the host superconductor. A BCS superconductor like the Kitaev chain in Sec. 2.1 hosts a Cooper-pair condensate and breaks fermion-number in favor of fermion-parity conservation.

As discussed extensively in Chapter 4, the most relevant setups for qubit applications contain parity-constrained groups of four or six Majoranas. From our general construction above, we understand that each such device realizes a single- or double-qubit, respectively. In the minimal four-Majorana setting, with operators $\gamma_{1,2,3,4}$ in Eqs. (2.14) and (2.15) fulfilling the parity constraint $\mathcal{P}_{\mathrm{box}} = \sigma_z^1 \sigma_z^2 = +$ in Eq. (2.17), we then define Pauli operators

$$\begin{aligned} \sigma_z = i\gamma_2\gamma_1 \equiv i\gamma_4\gamma_3 \ , \quad \sigma_x = i\gamma_3\gamma_2 \equiv i\gamma_4\gamma_1 \ , \quad \sigma_y = i\gamma_1\gamma_3 \equiv i\gamma_4\gamma_2 \ , \\ \sigma_z = \sigma_z^1 \equiv \sigma_z^2 \ , \quad \sigma_x = \sigma_x^1\sigma_x^2 \equiv -\sigma_y^1\sigma_y^2 \ , \quad \sigma_y = \sigma_x^1\sigma_y^2 \equiv \sigma_y^1\sigma_x^2 \ . \end{aligned} \tag{2.18}$$

For illustration, we here show both the Majorana representation and the reduction of two Pauli-sets to a single Pauli-set due to the parity-constraint. The qubit eigenstates are given as $|0\rangle = |0_1 0_2\rangle$ and $|1\rangle = |1_1 1_2\rangle$, representing occupation of neither (both) combined-fermion states n_1 and n_2 of Majoranas γ_1, γ_2 and γ_3, γ_4. As one can easily check, the Pauli operators $\sigma_{x,y,z}$ indeed have the correct action on these states.

2.3 Majorana braiding in wire networks

We now introduce the concept of braiding for Majorana fermions. The exchange statistics and inherent braid-properties of Majoranas are of adamant importance for their potential in quantum-information processing and -computing applications, and behind much of the interest in their realization. For the moment, we here mean braiding by slow and adiabatic manipulations of local parameters that allow to spatially dislocate and move around (viz. braid) Majorana zero-modes, following the principles of Ivanov (2001); Alicea *et al.* (2011). In contrast, Chapter 4 focuses on measurement-based braiding and measurement-based topological quantum computation, see Bonderson *et al.* (2008a); Nayak *et al.* (2008). While these approaches are different in implementation and operation of the underlying Majorana devices, they are practically equivalent in terms of (quantum) computational power.

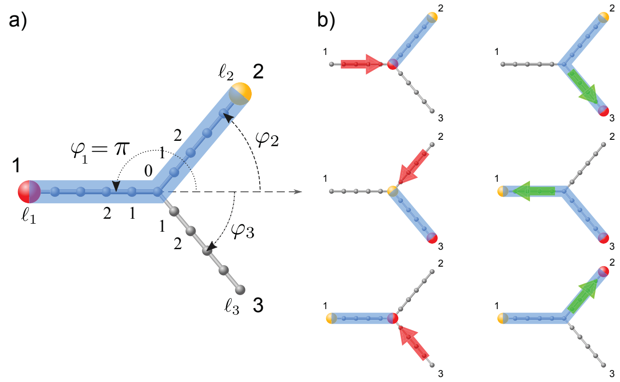

Figure 2.2: (a) Y-junction of three Kitaev chains that allows for braiding of MZMs. In the initial state, two Majorana bound-states (MBSs), depicted by red and yellow spheres, reside at the ends of a TS segment (blue tube). (b) Braid sequence for exchange of the two MBSs. Red (green) arrows indicate displacements of the MBSs by contraction (extension) of the TS segment, implemented by ramping local chemical potentials above (below) the critical value $\mu_c = 2t$. By end of the braid protocol, the TS segment is in the same position as before, but the MBSs are exchanged. Figure from Sekania *et al.* (2017).

2.3.1 Ideal Majorana braiding and statistics

We start with an introduction of ideal Majorana braiding that is independent of the specific hardware or system considered. Still, for concreteness, we may think of networks of 1D TSs, e.g. Kitaev chains as in Sec. 2.1, see also Fig. 2.2 and Sec. 2.3.2. For illustrative purposes, it is sufficient to consider the two-fold degenerate Hilbert space of only two MZMs $\gamma_{n,m}$ described by a low-energy Hamiltonian $H(t)$. All higher-energy excited states are discarded based on the existence of an excitation gap Δ_{topo}, as present in the Kitaev chain example. Operations employed to *move* and *braid* MZMs then have to be adiabatic with respect to the protective gap Δ_{topo}, meaning that e.g. chemical-potential manipulations $\mu(x,t)$ are performed slow with respect to an adiabaticity time-scale $\tau_{\text{ad}} \sim \Delta_{\text{topo}}^{-1}$.
In addition, strictly one-dimensional systems do not support braiding of MFs, since the MZMs that should be exchanged cannot pass through each other. As one moves domain walls hosting MBSs $\gamma_{n,m}$ closer to each other, the two MBSs become gapped and one ends up removing the topological phase altogether. Fortunately it is possible to use branched TS structures, e.g. the T- or Y-junctions of Alicea *et al.* (2011), to build quasi-one-dimensional systems that support the exchange of MZMs. We investigate braiding in such branched topological systems in Sekania *et al.* (2017), cf. Sec. 2.3.2 and Fig. 2.2.

Following TU Delft *et al.* (2018), we now consider a time-dependent but cyclic evolution of Hamiltonian parameters $H(t = 0) \to H(T) = H(0)$ that recovers the original Hamiltonian after operation time T. During this evolution, since it is performed in an adiabatic way, we assume that no excitations beyond the MZM sector $\gamma_{n,m}$ are created. By virtue of the adiabatic theorem, at each step of the operation we can characterize the state of the system by the unitarily evolved ground-state

$$|\psi(t)\rangle = U(t)\,|\psi(0)\rangle \ , \quad |\psi(0)\rangle = \alpha\,|0\rangle + \beta\,|1\rangle \ . \tag{2.19}$$

Here the time evolution is described by a unitary matrix $U(t)$, obtained from a reduced Schrödinger equation acting on the 2-dimensional ground state Hilbert space of $H(t)$. The initial state $|\psi(0)\rangle$ is given by an arbitrary superposition of the Majorana-parity eigenstates $i\gamma_n\gamma_m = \pm$, denoted $|0\rangle$ and $|1\rangle$. Similarly, we can characterize the state of the system by the time-dependent positions of its MZMs $\gamma_{n,m}[x_{n,m}(t)]$. Each MZM is bound to a domain wall between topological and trivial phases, cf. Eq. (2.12) and discussion. The MZMs can therefore be moved by slowly shifting Hamiltonian parameters that adjust location and extent of trivial and TS-segments, cf. Fig. 2.2. After the cyclic evolution has passed, and since we return to the initial Hamiltonian $H(T) = H(0)$, we therefore expect to have domain walls and MZMs located in the same spots as for the initial state of the system. The only option by which a unitarily evolved state $|\Psi(T)\rangle$ can differ from the initial state then is given by an exchange of the two indistinguishable MZMs, $x_{n,m}(0) \to x_{m,n}(T)$.

The form of the resulting unitary transformation U_{nm}, acting on the ground state sector of our system in Eq. (2.19), can be deduced on quite general grounds and without explicit knowledge of the Hamiltonian $H(t)$. First, adiabatic manipulations should not change the fermion parity $\hat{\mathcal{P}} = i\gamma_n\gamma_m$ in the ground-state sector. By definition, if the MZM parity is changed during the braiding protocol, somewhere in between there must have been an excitation out of the ground-state sector or an out-tunneling event of fermions from the system. Such processes would contain only a single MZM γ_n or γ_m, and therefore anti-commute with the MZM parity operator, $\{\gamma_{n,m}, \hat{\mathcal{P}}\} = 0$. Next, if only MZMs γ_n and γ_m are affected by the braiding process, the net unitary operation achieved at final time $t = T$ should depend only on their Majorana operators $\gamma_{n,m}$. Even if other parts of the system were involved, the MZM sector is energetically separated and therefore should be described by a product state of $|\psi(t)\rangle$ in Eq. (2.19) and some unknown, unimportant state for the remaining system. Together with the even-parity constraint, the only possible Hermitian operator appearing in U_{nm} is thus given by their fermion-parity $i\gamma_n\gamma_m$. Inserting into a unitary exponential-operator form, we obtain

$$U_{nm} = e^{-i\alpha(i\gamma_n\gamma_m)} = e^{\alpha\gamma_n\gamma_m} = \cos(\alpha) + \gamma_n\gamma_m\sin(\alpha) \ , \tag{2.20}$$

with a real phase-parameter α, and we used $(i\gamma_n\gamma_m)^2 = 1$. Of course we can insert additional phase factors $e^{i\alpha_0}$ which do not change any observables. Switching to the Heisenberg picture, the action of $U(T) = U_{nm}$ on the Majorana operators $\gamma_{n,m}(0) \to \gamma_{n,m}(T)$ reads

$$\begin{aligned} \gamma_n &\to U_{nm}\gamma_n U_{nm}^\dagger = \cos(2\alpha)\gamma_n - \sin(2\alpha)\gamma_m \ , \\ \gamma_m &\to U_{nm}\gamma_m U_{nm}^\dagger = \cos(2\alpha)\gamma_m + \sin(2\alpha)\gamma_n \ . \end{aligned} \tag{2.21}$$

Since at time T we return to the initial configuration of domain walls and MZMs up to exchanges of Majoranas, the only options for the acquired exchange phase are $\alpha = 0,\ \pm\pi/4$.

The trivial result $\alpha = 0$ corresponds to no exchange of Majoranas at all, where $\gamma_{n,m} \to \gamma_{n,m}$. The more interesting case is that of a finite braid phase $\alpha = \pm\pi/4$, where we have

$$\begin{aligned} \alpha = +\pi/4 \ : \quad & \gamma_n \ \to \ -\gamma_m \ , \quad \gamma_m \ \to \ \gamma_n \ , \\ \alpha = -\pi/4 \ : \quad & \gamma_n \ \to \ \gamma_m \ , \quad \gamma_m \ \to \ -\gamma_n \ . \end{aligned} \tag{2.22}$$

The different options can be identified with the two possible braid paths of the two MZMs: a clockwise exchange giving transformation U_{nm} followed by a counter-clockwise exchange should retrace the unitary evolution, and yield back the initial state. In terms of the unitary transformation in Eq. (2.20), we denote $B_{nm} = U_{nm}^{\pi/4} = (1 + \gamma_n\gamma_m)/\sqrt{2}$ by convention, and for the inverse braid find $U_{nm}^{-\pi/4} = (1 - \gamma_n\gamma_m)/\sqrt{2} = B_{nm}^\dagger = B_{mn}$ as expected.
In terms of quantum computations, consider the effect of a braid operation B_{nm} on a qubit defined by the MZMs pair $\gamma_{n,m}$, as encoded in state $|\psi(t)\rangle$ in Eq. (2.19). We find

$$|\psi(T)\rangle = B_{nm} |\psi(0)\rangle = \frac{1}{\sqrt{2}}(1 + \gamma_n\gamma_m) [\alpha |0\rangle + \beta |1\rangle] \simeq \alpha |0\rangle + i\beta |1\rangle \ , \tag{2.23}$$

up to an overall phase. A braid operation $B_{nm} = e^{(\pi/4)\gamma_n\gamma_m} = e^{-i\pi\sigma_z/4}$ with MZM parity operator $\sigma_z = i\gamma_n\gamma_m$ hence produces the so-called S-gate $\hat{S}_z = e^{-i\pi\sigma_z/4} \simeq \mathrm{diag}(1, i)$ in terms of the Majorana-encoded qubit, cf. Nielsen and Chuang (2010) and Chapter 4.

2.3.2 Braiding errors in interacting Majorana quantum wires

We now give a short overview on braiding of two MBSs in a Y-junction with interactions, cf. Sekania *et al.* (2017) and Fig. 2.2. Motivated by Alicea *et al.* (2011), a wealth of earlier research is available, and for an extensive discussion we refer to our publication.
We here aim at a general understanding of braid fidelity and exchange statistics without any assumptions on the outcome of a MBS braiding operation. This includes a calculation of the many-body exchange phase $\Phi(t)$ between even and odd total-parity states due to cyclic manipulations of the time-dependent Hamiltonian $H(t)$. We consider the full Hilbert space of excited states, unlike in the two-MBSs toy model above, and hence can understand how abstract braiding relates to an exchange of Majorana quasi-particles (MBSs) in non-ideal TS condensed-matter systems. Further we take general measures for the performance of quantum operations as conventionally used in quantum-information related context.

We first include interactions in the Kitaev chain model of Sec. 2.1. On a Hamiltonian level, this can be done by adding terms $\sim V n_j n_{j+1}$ to the chain in Eq. (2.1), with interaction strength V. The fermion densities in nearest-neighbor interactions enter through occupation number operators $n_j = c_j^\dagger c_j$. Previous work on the ground-state phase diagram of interacting Kitaev models (Gangadharaiah *et al.*, 2011; Stoudenmire *et al.*, 2011) shows breakdown of superconductivity and the TS phase for strong interactions of either sign.
To allow braiding, we now arrange three chains into a Y-shape junction in Fig. 2.2, where we also show the braid protocol. The movement of the trivial-TS domain walls and their attached MBSs, leading to a braid transformation on the ground-state sector as in Sec. 2.3,

is achieved by ramping local chemical potentials above or below the phase transition threshold $\mu_c = 2t$, cf. Sec. 2.1. During and after the braiding is carried out, we now track two measures to characterize the braid performance of our protocol.
First we calculate the fidelity of state evolution. With instantaneous ground state $|\psi(t_0)\rangle$ at time t_0 before the braid operation as reference, we define the "loss function"

$$w_{\rm loss}(t_{\rm f}) = 1 - [F(t_{\rm f})]^2 = 1 - |\langle\psi(t_{\rm f})|\psi(t_0)\rangle|^2 \ . \tag{2.24}$$

Here $F(t_{\rm f})$ is the fidelity for pure states (Nielsen and Chuang, 2010), taken between the initial and time-evolved (final) state $|\psi(t_{\rm f})\rangle$. The system is parity-conserving, and there are no transitions between total even- and odd-parity sectors. Since at $t = t_{\rm f}$ we returned to the initial state but for the braid transformation, under purely adiabatic evolution, the loss functions in both parity sectors should be zero, $w_{\rm loss}^{e/o} = 0$. If one finds $w_{\rm loss}^{e/o} > 0$, this indicates excitations above the even/odd ground-state sectors due to non-adiabacity.

For small (zero) loss, the only effect of the braid operation is an exchange phase *between* states of both sectors, which does not show in the intra-sector loss functions. We here quote the result by Samuel and Bhandari (1988); Mukunda and Simon (1993) as

$$\phi_g(t) = \arg\langle\psi(t_0)|\psi(t)\rangle - \mathrm{Im}\int_{t_0}^{t}\langle\psi(t')|\dot{\psi}(t')\rangle\, dt' \ . \tag{2.25}$$

The first component describes the full phase acquired during the braid operation $t' \in [t_0, t]$, and with the second term we subtract dynamical phase contributions explicitly. As defined in Eq. (2.25), $\phi_g(t)$ thus encodes the *geometric* many-body phase acquired by state $|\psi(t)\rangle$. In our numerics, we employ a discretized variant of the functional in Eq. (2.25). Further we calculate only the geometric exchange or *braid phase* between even and odd ground-states, $\Phi(t_{\rm f}) = \phi_g^o(t_{\rm f}) - \phi_g^e(t_{\rm f})$, that supposedly is a detail-independent and topologically protected quantity. We expect $|\Phi_{\rm id}| = \pi/2$ from ideal Majorana exchange statistics, cf. Sec. 2.3.

Some results are shown in Fig. 2.3. The braid protocol in Fig. 2.2(b) has finished at time $t_{\rm f} = 6T$, after six individual chemical-potential ramping steps, each with ramp time T. All parameters are given in units of the (inverse) hopping strength t, cf. Eq. (2.1).
We observe that increasing the ramp time T reduces non-adiabatic losses, as found by many other authors. However, the smoothness of ramp protocols has a more dramatic effect on non-adiabatic errors. We here implement a "guillotine" (red) and "sine-squared" (black) ramp that have discontinuities in first and second derivative, respectively. As also shown in Knapp *et al.* (2016), the degree of smoothness is much more critical to avoiding non-adiabatic errors than the ramp time T itself. We verify their result of an approximately exponential reduction of losses $w_{\rm loss}^{e/o}$ upon increasing the smoothness by one order. Next, for the exchange phase Φ in Fig. 2.3, we find a systematic deviation from ideal braiding statistics with $|\Phi_{\rm id}| = \pi/2$ upon departing from perfect localization ($\xi = 0$). While in principle it is expected that MF statistics are recovered only for (fully) localized MBSs, before our work this effect had not been systematically quantified. We here essentially observe

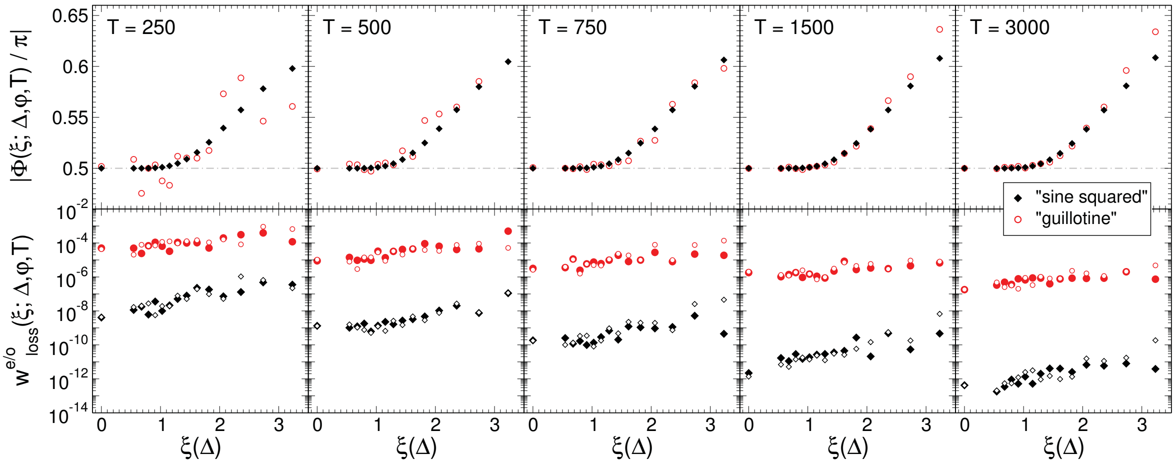

Figure 2.3: Exchange phase Φ (top row) and loss of fidelity $w^{e/o}_{\text{loss}}$ (bottom row) after the braid vs MBS localization length ξ, for two distinct ramp protocols. Plots from left to right correspond to ramping time periods of $T = 250, ..., 3000$ as indicated. Data points (left to right) are for pairing amplitudes $\Delta = 1.0, ..., 0.3$, which translates to increasing MBS localization length $\xi(\Delta)$ from left to right. Figure from Sekania *et al.* (2017).

an onset of the topological-trivial phase transition in our system of Fig. 2.2, through a shift of exchange phase (statistics) from $\pi/2$ (Majorana) to multiples of π (regular fermions). Remarkably, the non-adiabatic losses are almost completely uncorrelated with this shift of exchange statistics: rapid braiding with strongly localized MBSs gives results much closer to the ideal braid phase value than slow braid routines at larger hybridization length.
Finally, the effect of interactions on exchange statistics is discussed in Sekania *et al.* (2017). As before, braid performance and MBSs localization length are strongly correlated, where the latter is influenced by interactions that reduce or enhance the effective superconducting pairing in the chain, cf. Gangadharaiah *et al.* (2011); Stoudenmire *et al.* (2011).

Our work in Sekania *et al.* (2017) contrasts the approach of other authors for the analysis of braiding in Majorana systems, cf. Cheng *et al.* (2011); Clarke *et al.* (2011); Karzig *et al.* (2013); Scheurer and Shnirman (2013); Karzig *et al.* (2015a,b); Amorim *et al.* (2015).
Time scales of near-adiabacity can give hints for a promising operation regime, but should not be considered conclusive for a good braiding performance. Instead the smoothness of the ramp protocols is a much more crucial indicator for the generation and propagation of non-adiabatic errors, cf. Pedrocchi and DiVincenzo (2015); Knapp *et al.* (2016).
From the viewpoint of Majorana exchange statistics in the adiabatic limit, the localization length and residual overlaps are simple but important figures of merit. Our results caution to differentiate between "real" MFs (Majorana, 1937) and MBSs as low-energy excitations in TSs (Kitaev, 2001; Ivanov, 2001). For the latter, only under near-perfect localization, ideal braid statistics are realized and one can think of a "toy-model system" of independent MZMs. Else one should consider the full many-body eigenstates of the underlying TS.

2.4 Mesoscopic Majorana islands

In this section we introduce mesoscopic topological superconductors, also referred to as *(mesoscopic) Majorana islands* or *Majorana boxes*. In contrast to grounded TSs, these systems have a finite (large) charging energy and obey charge conservation in in- and out-tunneling events. Floating (non-grounded) Majorana islands are interesting in many ways, including for the generation of correlations in charge transport between quantum dots, cf. Sec. 2.4.2. Further, Majorana boxes are important towards the formation of (topological) Kondo effects, see Chapter 3, or as basis for topological qubits, see Chapter 4.
Multi-terminal coupled Majorana boxes were studied in Fu (2010); Zazunov *et al.* (2011); Hützen *et al.* (2012) and Béri and Cooper (2012); Altland and Egger (2013); Béri (2013).

2.4.1 Charge conservation in Majorana boxes

A general mesoscopic Majorana island is described by a set of charge-neutral, fermionic MZMs $\gamma_{j=1,\ldots,M}$ and a single pair of bosonic phase- and charge-variables. While the MZMs are as before, charge conservation due to a finite charging energy on the island implies a promotion of the conjugate bosonic phase- and charge-variables to operators. We write

$$[\varphi, Q]_- = i \ , \quad e^{\pm i\varphi} |Q\rangle = |Q \pm 1\rangle \ , \tag{2.26}$$

where $\varphi = \phi/2$ is half the superconducting phase and Q counts charges in units of the electron charge e. The phase-exponential operator $e^{\pm i\varphi}$ describes creation (annihilation) of one charge or half a Cooper-pair, and above we denoted its action on charge states $|Q\rangle$. (Operators and eigenvalues φ, Q share symbols; the distinction follows from context.)
Now recall the Kitaev chain Hamiltonian in Eq. (2.1). The superconducting pairing term here comes with an amplitude Δ and phase ϕ, and the latter corresponds to the bosonic variable appearing above. If one considers a charge conserving system, the attached phase exponential $e^{i\phi} = e^{2i\varphi}$ in sc pairing terms $\Delta e^{i\phi} c_j c_{j+1}$ explicitly accounts for the creation of a charge $2e$ Cooper pair upon pairing two electrons on sites j and $j+1$. The Cooper pair condensate of a BCS superconductor thus enables free absorption and emission of electron pairs (with charge $2e$) from its fermionic sector, cf. Bruus and Flensberg (2016).

A Hamiltonian term describing charging energy effects, depending on the overall charge Q of the mesoscopic (topological) superconductor, can now be introduced as

$$H_c = E_c (Q - n_g)^2 \ , \quad E_c = \frac{e^2}{2C} \ . \tag{2.27}$$

Here E_c is a single-electron charging energy that is inversely proportional to the geometric capacitance C of the island. The parameter $n_g \sim V_g$ describes tuning of the equilibrium box charge due to a nearby electrostatic gate with applied gate voltage V_g. In contrast to a grounded island with fixed (superconducting) phase variable φ, a *floating* box with pinned equilibrium charge $\langle Q \rangle = n_g$ shows strong fluctuations of the conjugate phase-variable.

A second characteristic term for charge transport in Majorana boxes describes the contact to a bulk superconducting reservoir with phase φ_0. It is captured by a Josephson term

$$H_J = -E_J \cos[2(\varphi - \varphi_0)] = -\frac{E_J}{2}\left[e^{2i(\varphi-\varphi_0)} + e^{-2i(\varphi-\varphi_0)}\right] , \tag{2.28}$$

where E_J is the Josephson coupling that depends on details of the contact. The above phase exponential operators describe transport of Cooper pairs (charge $2e$) between the mesoscopic island and the bulk sc with phase φ_0. By definition, the reservoir is large and its single-electron charging energy is negligible, such that φ_0 enters as classical parameter. A *grounded* Majorana island is recovered for $E_J \gg E_c$, where the islands sc phase becomes pinned to that of the reservoir, $\varphi \approx \varphi_0$, and returns to being a classical instead of quantum variable, cf. Sec. 2.1. The conjugate charge variable on the island then fluctuates strongly in units $2e$ and the charging energy in Eq. (2.27) is suppressed (Hyart *et al.*, 2013).

Another option for contacting Majorana boxes are leads or single-level quantum dots (QDs), as used to probe MBSs by transport in Albrecht *et al.* (2016); Deng *et al.* (2016). For a qualitative understanding, it often is sufficient to consider Majorana-dot or -lead tunnel-junctions in terms of simple tunnel Hamiltonians (Fu, 2010; Hützen *et al.*, 2012)

$$H_t = \lambda d^\dagger \gamma e^{-i\varphi} \ + \ \text{h.c.} \ . \tag{2.29}$$

Here λ is the (complex) tunnel-matrix element between a MBS with MF operator γ and the dot- or lead-fermion state annihilated by the fermion operator d. We assume point-like tunneling, where (e.g.) a lead-fermion operator $\psi(x)$ is taken at the contact point, with $d \equiv \psi(x=0)$. All additional structure of wave-function overlaps that enable the tunneling events is absorbed in the tunnel-coupling λ. At low energies $\lambda, \omega, ... \ll \Delta_{\text{topo}}$ (excitation gap Δ_{topo} on the box), the only fermionic states available for in- or out-tunneling are MBSs, and no further contributions to H_t arise. Charge tunneling events thus have to involve the charge-neutral Majorana operators, and an out-tunneling event $\sim d^\dagger\gamma$ is accompanied by annihilation of a single charge on the island, captured by the phase-exponential $e^{-i\varphi}$.

Re-inserting the complex-fermion representation of Sec. 2.1, we note $\gamma = e^{i\varphi} f + e^{-i\varphi} f^\dagger$ and a secondary Majorana $\gamma' = -i\left(e^{i\varphi} f - e^{-i\varphi} f^\dagger\right)$. Majorana operators are gauged such that they explicitly appear as charge-neutral, where annihilation (creation) by the fermion operator $f^{(\dagger)}$ comes with creation (annihilation) of a single charge in the bosonic sector. In the charged-fermion language, we obtain (Fu, 2010; Hützen *et al.*, 2012)

$$H_t = \lambda d^\dagger \left(f + e^{-2i\varphi} f^\dagger\right) \ + \ \text{h.c.} \ . \tag{2.30}$$

Tunneling out of MBSs on a TS box implies an equal superposition of out-tunneling from a fermion state (f), or in-tunneling into that state ($f^\dagger$) under simultaneous splitting of a Cooper pair ($e^{-2i\varphi}$), and out-tunneling into the attached dot/lead ($d^\dagger$). For an extensive discussion of charge transport in resonant or co-tunneling regimes of two-terminal Majorana islands, we refer to the introductory works of Fu (2010); Hützen *et al.* (2012).

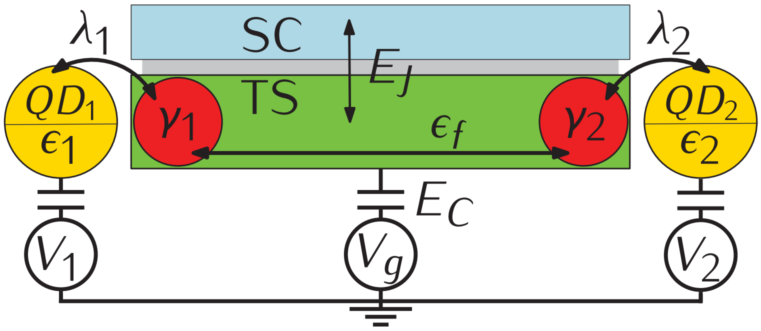

Figure 2.4: Two-terminal Majorana island (TS, green) with two MBSs $\gamma_{1,2}$ (red) contacted by tunnel-coupling $\lambda_{1,2}$ to left/right single-level quantum dots $\mathrm{QD}_{1,2}$ (yellow). In addition we include a Josephson coupling E_J to a bulk superconductor (SC, teal). Gate potentials $V_{1,2}$ allow to adjust level energies $\epsilon_{1,2}$ on dots $\mathrm{QD}_{1,2}$, and the box equilibrium charge is controlled by the gate parameter $n_g \sim V_g$. A residual Majorana hybridization ϵ_f enters as level-energy for the composite-fermion state f. Figure from Plugge *et al.* (2015).

2.4.2 The Majorana entanglement bridge

We now review the Majorana-mediated generation of entanglement between distant single-level quantum dots. To this end, consider a two-terminal island hosting MBSs $\gamma_{1,2}$, tunnel-coupled with strength $\lambda_{1,2}$ to two quantum dots $\mathrm{QD}_{1,2}$ in Fig. 2.4. The low-energy eigenstates, projected or truncated perturbative Hamiltonians and resulting entanglement and correlations between the two quantum dots, with a detailed discussion of this setting, are given in Plugge *et al.* (2015). A similar investigation, for a strongly reduced parameter setting in near charge-degenerate islands, is published in Wang *et al.* (2013).
Here we summarize the concepts and results that are most relevant for later chapters. In particular, the co-tunneling regime of Majorana boxes is accessible by perturbation theory in scales $\sim \lambda_j/E_c,\ E_J/E_c$. All Majorana-dot or Majorana-lead couplings λ_j or Josephson couplings E_J are assumed to be small against the charging energy E_c in Eq. (2.27), while the (topological) gap is always assumed to be large, i.e. $\lambda_j,\ E_J,\ \ldots \ll E_c \lesssim \Delta_{\text{topo}}$.

A practical and systematic approach to implement co-tunneling perturbation theory is the generalized Schrieffer-Wolff (SW) transformation of Bravyi *et al.* (2011). This method projects Hamiltonian terms that are off-diagonal matrix elements in the charge basis $|Q\rangle$, e.g. $e^{\pm i\varphi}$ or $e^{\pm 2i\varphi}$ in Eq. (2.26), onto the box charge ground state with $\langle Q\rangle = n_g$. Under Coulomb blockade conditions, with gate parameter n_g close to integer values, macroscopic fluctuations of the box charge are then traded off against effective co-tunneling rates. The latter take the form $\Gamma \sim t^n/E_c^{n-1}$ for a n-th order tunneling event, where amplitudes t comprise both single-charge and Cooper-pair tunnel-processes. Charge transport in this picture takes place via $n-1$ intermediate, excited charge states $Q \to Q \pm 1,\ Q \pm 2$, etc., that are virtually occupied for short times $\tau_c \sim E_c^{-1}$. The scale $1/E_c$ hence supplies a short-time cutoff, and enters as energy denominator in the effective coupling amplitude Γ.

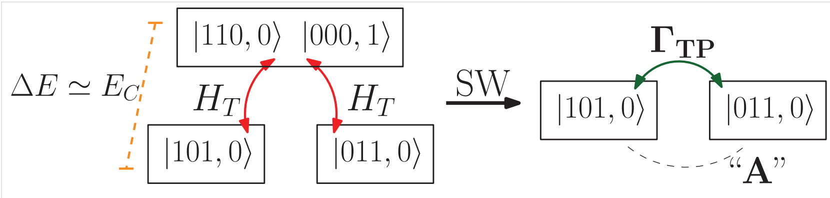

Figure 2.5: TP-mediated coupling of QDs, from co-tunneling perturbation theory for small $\lambda_{1,2} \ll E_c$ in H_T. After a SW transformation, the low-energy projected theory with island charge $Q_A = 1$ contains only two states $|101, 0\rangle$ and $|011, 0\rangle$. These are connected by a second-order process with effective coupling amplitude $\Gamma_{\mathrm{TP}} \sim \lambda_1 \lambda_2^* / E_c$, cf. Eq. (2.32).

We denote occupation number states of the system as $|n_1 n_2 n_f, N_c\rangle$, where $n_{1,2}$ are fermionic single-level states on $\mathrm{QD}_{1,2}$, n_f is the combined fermion f of MFs $\gamma_{1,2}$, and N_c counts Cooper pairs. The total box charge follows as $Q = 2N_c + n_f$, where we explicitly switched to the charged-fermion language in Eq. (2.30). Assuming a conserved overall fermion parity, we can focus on the even-parity states with two different gate parameter settings $n_g = 0,\ 1$. (We disregard an unimportant offset $n_g \to n_g + 2N_c$ by some number of Cooper pairs N_c.)

A projection to the box charge ground state with $Q_{A(B)} = 0(1)$ yields two sets of states

$$A = \{|10\rangle\,, |01\rangle\}_{n_1 n_2} \otimes |1, 0\rangle_{n_f, N_c} \ , \qquad B = \{|00\rangle\,, |11\rangle\}_{n_1 n_2} \otimes |0, 0\rangle_{n_f, N_c} \ . \tag{2.31}$$

As depicted in Fig. 2.5, for states of same fermion number and charge in set "A", MBS-QD tunnel couplings $\lambda_{1,2}$ in a tunneling Hamiltonian H_T similar to Eq. (2.30) can transport an electron across the island. These processes take place via excited charge-states with no (two) charges on the island which are gapped by the charging energy, $\Delta E \simeq E_c$. The choice of excited state here depends on the order of tunneling events. An effective co-tunneling rate results after SW-projection to the box charge ground-state $Q_A = 1$, and connects the two low-energy states of sector "A''. The reduced Hamiltonian of box-coupled QDs is

$$H_{\mathrm{TP}} = \Gamma_{\mathrm{TP}} d_1^\dagger d_2 + \mathrm{h.c.} \ + \ H_{\mathrm{QDs}} \ , \qquad \Gamma_{\mathrm{TP}} \sim \lambda_1 \lambda_2^* / E_c \ , \tag{2.32}$$

where $d_j^{(\dagger)}$ annihilates (creates) one electron on quantum dot $\mathrm{QD}_{j=1,2}$, and H_{QDs} encodes the remaining level-energies of the dots. Since the Majorana island facilitates non-local electron transport, this process has been dubbed "electron teleportation" by Fu (2010).

One can also perform a SW projection for the ground-state sector with equilibrium charge $Q_B = 0$ in Eq. (2.31). However, since the QD states in set "B" have different total charge, a co-tunneling event connecting the two states has to comprise a Cooper-pair tunneling between the bulk sc and Majorana island in Fig. 2.4. The latter is mediated by a Josephson coupling $\sim E_J$ as in Eq. (2.28). The full third-order co-tunneling event then combines a Cooper-pair tunneling with in- or out-tunneling of electrons at both quantum dots, $\sim \lambda_{1,2}$. The reduced Hamiltonian describing the box-coupled QDs now reads

$$H_{\mathrm{CAR}} = \Gamma_{\mathrm{CAR}} d_1^\dagger d_2^\dagger + \mathrm{h.c.} \ + \ H_{\mathrm{QDs}} \ , \qquad \Gamma_{\mathrm{CAR}} \sim \lambda_1 \lambda_2 E_J / E_c^2 \ . \tag{2.33}$$

This effective Hamiltonian describes pairing of electrons in the QDs under simultaneous emission of Cooper pairs into the bulk sc, and vice versa. Such processes were investigated for grounded devices with strong Majorana hybridization by Nilsson *et al.* (2008), and dubbed crossed Andreev-reflection (CAR) in contrast to local Andreev-reflection (AR) of a Cooper pair at a single QD or lead-contact.

After the basic introduction to co-tunneling perturbation theory for Coulomb-blockaded Majorana boxes that will be used throughout this thesis, we now summarize the main results of Plugge *et al.* (2015). Here we were interested in relating entanglement of box-coupled QDs to the effective low-energy theories in Eqs. (2.32) and (2.33). For a detailed discussion of entanglement and quantum correlations, see Nielsen and Chuang (2010) and the review by Horodecki *et al.* (2009).

Based on the simple effective Hamiltonians above, if level energies and other contributions in H_{QDs} are negligible against the inter-dot coupling ($\Gamma_{\mathrm{TP/CAR}} \gg \epsilon_{1,2}$), diagonalization yields eigenstates of the two coupled QDs as

$$|\psi^A_\pm\rangle = \frac{1}{\sqrt{2}}\left(|10\rangle \pm |01\rangle\right)_{n_1 n_2} \ , \quad |\psi^B_\pm\rangle = \frac{1}{\sqrt{2}}\left(|00\rangle \pm |11\rangle\right)_{n_1 n_2} \ . \tag{2.34}$$

The TP-generated states $|\psi^A_\pm\rangle$ are even and odd superpositions in subset A, cf. Eq. (2.31). Eigenstates $|\psi^A_\pm\rangle$ are gapped by hybridization $\pm\Gamma_{\mathrm{TP}}$, where the odd superposition becomes the true ground state of the double-QD system. Since the box charge state is projected to a fixed value $Q_A = (2N_c + n_f)_A$, the full eigenstates are product states $|\Psi^A_\pm\rangle = |\psi^A_\pm\rangle \otimes |Q_A\rangle$. An analogous discussion follows for CAR-mediated states in set B.

We now observe that the QD eigenstates in Eq. (2.34) are nothing but the well-known Bell states, where the entangled degrees of freedom are the occupation numbers $n_{1,2}$ of $\mathrm{QD}_{1,2}$ in Fig. 2.4. Bell states are maximally entangled, as measured for example by the concurrence (Horodecki *et al.*, 2009) of the two QDs. With $H_{\mathrm{QDs}} \to 0$ in Eqs. (2.32) and (2.33), phase-coherent electron teleportation (TP) or crossed Andreev-reflection (CAR) thus facilitates full entanglement and maximum correlations between two distant quantum dots.

For a detailed discussion and further results, see Plugge *et al.* (2015). There we also consider the dynamical problem after an initial switch-on of couplings, $\Gamma_{\mathrm{TP}}(t) = \Gamma_{\mathrm{TP}}$ for $t \geq 0$, and confirm that the simple effective Hamiltonian in Eq. (2.32) does not only capture static ground-state properties, but likewise the time-dependent generation of correlations. A related study, but for a grounded Majorana island, was presented in Li *et al.* (2014).

2.5 Summary: basics of Majorana fermions

We now give a summary of results that are most relevant towards the following chapters.

MBSs can be generated at the edges of TS systems like the Kitaev chain, cf. Sec. 2.1. Implementations of 1D TSs in semiconductor-superconductor quantum wires have shown promising signatures of MBSs in quantum transport experiments, see Mourik *et al.* (2012); Albrecht *et al.* (2016); Deng *et al.* (2016); Nichele *et al.* (2017); Zhang *et al.* (2018) and the review by Lutchyn *et al.* (2017). Such systems combine several ingredients, including magnetic Zeeman fields, strong spin-orbit coupling and (induced) s-wave superconducting pairing in low-density semiconductor wires, to achieve an effective low-energy TS phase (Oreg *et al.*, 2010; Lutchyn *et al.*, 2010; Alicea, 2012). Nevertheless, for energies well below the topological gap Δ_{topo}, a toy-model description of TS systems in terms of localized MBSs plus Cooper pairs is valid. The discussion in the following chapters can thus be considered as universal and independent of a specific Majorana platform, though for concreteness we may sketch 1D TS wire systems as promising experimental candidates.

In Sec. 2.2 we learned how to reformulate the ground-state sector of a Majorana box in a language suitable for QIP applications. Majorana-based qubits are highly unconventional in the sense that different Pauli operators become spatially non-local distributed objects due to their origin from Majorana operators and MZMs, cf. Chap. 4. The underlying topological character validates the notion of topologically protected qubits on Majorana islands, and their highly degenerate ground states should allow to *store* quantum information for rather long times; the protection of Majorana-based qubits and quantum memories against decoherence and noise is inherited from the MZMs that serve as their building blocks.

A possible route to protected manipulation of a two-MZM system was shown in Sec. 2.3. Unfortunately, the hardware platform of Alicea *et al.* (2011) is difficult to realize, and alternative schemes for Majorana-fusion experiments were proposed in Aasen *et al.* (2016). In our work, we investigate alternative *access*- and *manipulation*-protocols for Majorana systems that respect the inherent protection of Majorana-based qubits, and benefit from the underlying Majorana non-locality. This includes a detailed analysis of quantum transport in Majorana boxes, cf. Chapter 3, and leads to the development of protected manipulation protocols for Majorana qubits and code networks in Chapter 4.

As mentioned in Sec. 2.2, most schemes that are under discussion recently do not encode qubits into the total-parity state of a TS system. Instead it is desirable to work in a fixed total-parity sector and define qubits within the residual degenerate ground state space. The braid protocols in Sec. 2.3 also work in subsectors, and by exchanging different MZMs in a system with $M = 4$ or 6 Majoranas, one can employ protected S-gate rotations around arbitrary Pauli axes, $\hat{S}_{a=x,y,z} = e^{-i(\pi/4)\sigma_a}$. As a consequence, the full single-qubit Clifford group for quantum computations can be realized by braiding. Supplementing this with two-qubit (4-MZM) measurements, the full Clifford group including e.g. the two-qubit controlled-NOT gate can be realized in a protected manner, cf. Chapter 4. This is a good basis for quantum storage and information processing, but not yet sufficient for universal quantum computations. We discuss strategies on how to extend Majorana qubits to code networks, and how to implement quantum error-correcting codes and reach code-based universality (Preskill, 2018; Terhal, 2015) in these networks in much of Chapter 4.

In mesoscopic Majorana islands, charge-conservation on the device and in tunneling to its MBSs becomes crucial, cf. Sec. 2.4. In addition to MFs as charge-neutral fermions, one then includes a dual pair of bosonic phase- and charge-variables on the box. The most important aspect of Majorana boxes is that charging energy facilitates *phase-coherent single-electron transport* across the island. In non-TS context, this is known for tunneling in mesoscopic metallic islands or QDs with large fermionic level spacing (Bruus and Flensberg, 2016). To this end, we remark that a Majorana island with two MBSs essentially behaves like a single-level QD (occupation $n_f = 0,\ 1$) with charging energy E_c and level spacing Δ_{topo}, by which all other fermionic states are gapped, cf. Fu (2010) and Sec. 2.4.2.

In Plugge *et al.* (2015), we extend earlier work on transport (Fu, 2010; Hützen *et al.*, 2012) and correlations (Wang *et al.*, 2013; Li *et al.*, 2014) mediated by such islands to general parameter regimes. We then show how the generation of entanglement in quantum dots attached to Majorana boxes can be understood in terms of simple effective Hamiltonians. By employing similar peturbative methods, in the following this allows to reduce the complexity of charge tunneling and quantum transport phenomena in general Majorana devices. Our findings give confidence that – at least on a qualitative level – strongly correlated quantum states in Majorana networks with multiple tunnel-coupled islands, leads and quantum dots, cf. Chapters 3 and 4, are well-described by effective co-tunneling theories.

Finally, remark that the requirement of large topological gaps and adiabatic operations, e.g. in braiding, in practice poses serious constraints on the viability of (topological) quantum computation with MZMs. A significant part of the experimental efforts towards realization of Majorana-based topological quantum computation (TQC) hence focuses on engineering and materials design for larger protective gaps. We gave some references to Majorana experiments above, and review more recent experimental advances on the fabrication of Majorana platforms in the concluding Chapter 5 of this thesis. For the remainder of our discussion, unless explicitly stated otherwise, we cast aside materials engineering problems and assume large protective gaps and a clean isolation of MZMs in the topological superconducting structures under investigation.

Chapter 3

Quantum transport in Majorana boxes

In this Chapter we discuss low-energy quantum transport phenomena in Majorana boxes. Since this is an almost endlessly manifold field, we here focus on effective toy-models of mesoscopic Majorana islands, see the introduction in Chapter 2. This is in contrast to detailed studies of "realistic" and microscopically-modeled systems that aim toward the experimental-realization and materials-engineering part of Majorana research. Therefore most of our results and conclusions, while robust against some degree of error in Majorana realization, should be considered as qualitative instead of precise quantitative statements. At the same time, this approach allows us to go well beyond "simple" single-wire devices, and to unveil qualitatively new effects emerging in more general Majorana networks.

An example of exotic quantum transport in Majorana networks is the *topological Kondo effect* (TKE), cf. Béri and Cooper (2012); Altland and Egger (2013); Béri (2013), which in Secs. 3.1 and 3.2 we take as a basic setup to introduce concepts and techniques used in our later works. In Plugge *et al.* (2016b); Gau *et al.* (2018) we aim at an understanding of general Majorana-Majorana and lead-Majorana junction geometries, where we present two important examples in Sec. 3.3. Finally, in Sec. 3.4, we summarize the main ideas and solution strategy for tackling quantum transport problems in general Majorana networks. We note that multi-junctions between Majoranas, leads and quantum dots are of adamant importance in quantum-information processing applications, e.g., for the development of Majorana-based qubit and network architectures in Chapter 4. Recent progress towards the experimental realization of network devices is reviewed in the concluding Chapter 5.

In much of this Chapter we use books by Gogolin *et al.* (2004); Altland and Simons (2010); Bruus and Flensberg (2016) and the excellent review of Von Delft and Schoeller (1998).

3.1 Junctions in Majorana networks

We start with the most essential ingredients for quantum transport in Majorana networks: simple and multi-junction tunnel contacts between islands, leads and quantum dots (QDs). While here we focus on the case of Majorana boxes coupled to normal non-interacting leads, many aspects also transfer to islands in contact with QDs. First, for uncoupled boxes and leads, the basic Hamiltonian describing such a system is given by

$$H_0 = H_{\text{boxes}} + H_{\text{leads}} = \sum_{j\in\text{boxes}} H_{\text{box},j} + \sum_{k\in\text{leads}} H_{\text{lead},k} \ . \tag{3.1}$$

Here $H_{\text{box},j}$ encodes charging energy effects on a Majorana box, cf. Eq. (2.27), and depends only on variables of island j. Similarly, $H_{\text{lead},k}$ contains kinetic energy terms of the lead fermions in the normal lead k. By definition, H_0 above does not contain any off-diagonal terms that facilitate charge transport between different leads or boxes of the system. The physical implications of charge conservation on H_0 are minimal, in particular H_{leads} is as in the non-conserving setting (Altland and Simons, 2010). In contrast, for tunneling *between* different parts of the system, charge conservation becomes an important ingredient.

We now recapitulate a few basic types of tunnel-Hamiltonians for Majorana networks, cf. Sec. 2.4. Tunneling between MBSs on distinct islands can be described by

$$H_t = t_{jk}\gamma_j\gamma_k e^{i(\varphi_j-\varphi_k)} \ + \ \text{h.c.} \ , \tag{3.2}$$

where $\gamma_{j,k}$ is hosted on the island with phase $\varphi_{j,k}$. On a microscopic level, point-like tunneling amplitudes as t_{jk} are determined from propagation of the transferred electron through an intermediate non-topological segment that separates the islands. Here we take them as simple phenomenological parameters that enter our effective description. H_t then describes transfer of a single charge under simultaneous effect on the islands fermion-sector encoded by Majoranas $\gamma_{j,k}$. Two consecutive tunnel events yield a transferred Cooper pair, where the Majorana-part squares out, $\gamma_j^2 = \gamma_k^2 = 1$. Therefore single-charge transfer processes in Eq. (3.2) also facilitate Josephson coupling between islands, cf. Eq. (2.28).
Next, tunneling between Majoranas and leads is given by (cf. Eq. (2.29))

$$H_\lambda = \lambda_{jk}\Psi_j^\dagger\gamma_k e^{-i\varphi_k} \ + \ \text{h.c.} \ , \tag{3.3}$$

where $\Psi_j = \psi_j(x=0)$ is the lead fermion operator at the contact point $x=0$, and λ_{jk} is the tunneling amplitude connecting MBS γ_k and the lead. H_λ above describes transport of a single charge, through the MBSs, into a charged fermion of the attached lead.
Finally, we do not consider direct tunneling between distinct leads, i.e., terms $\sim J_{jk}\Psi_j^\dagger\Psi_k$. In principle they could be present, but in the systems below are forbidden by spatial distance between lead contacts; the latter is overcome only by tunneling through the MBSs.

3.1.1 Bosonization and Majorana-Klein fusion

A basic motivation behind field-theoretical bosonization is that 1D fermion systems, much unlike their higher-dimensional counterparts, harbor long-lived, low-energy bosonic quasi-particle excitations. These manifest in charge-density waves that propagate through the system, where individual fermions cannot move past each other due to the constrained dimensionality. Exchange statistics thus do not become apparent in 1D systems, instead fermions behave like hard-core colliding bosons. Based on the wave-like collective excitations, in seminal work Haldane (1981a,b) coined the term *Luttinger liquids* for such systems that are equivalently described by a fermionic or bosonic theory.
We now reduce the above Hamiltonians by applying field-theoretical bosonization to the lead-fermion operators. This method allows for significant technical simplifications in the analysis of low-energy properties and quantum transport in Majorana networks. Details are delegated to introductory chapters of our works Plugge *et al.* (2016b); Gau *et al.* (2018) and books by Altland and Simons (2010) and Gogolin *et al.* (2004). Here we recall only the most important "recipes" for switching between fermionic and bosonic languages.

Throughout our discussion, we consider leads as half-infinite, non-interacting normal wires (coordinate $x \leq 0$) that terminate at the Majorana island, $x = 0$. Each lead contains right- and left-moving electrons that represent in- and out-going fermions for the island, respectively. The lead fermion operator for a given lead j can be written as

$$\psi^\dagger_{j,R/L}(x) \sim \kappa_j e^{i[\phi_j(x) \pm \theta_j(x)]} \ . \tag{3.4}$$

The dual boson-fields $\phi_j(x)$ and $\theta_j(x)$ obey an algebra $[\phi_j(x'), \partial_x \theta_k(x)]_- = i\pi\delta(x'-x)\delta_{jk}$, and κ_j is a Klein factor that ensures anti-commutation between different lead-fermions and with Majoranas. It can be represented by a MF, where $\kappa_j = \kappa_j^\dagger$ fulfill a Clifford algebra between each other and with the island Majoranas γ_n. The dual pairs of one-dimensional boson fields are the phase- and charge-variables for the original electrons, while the Klein-factors capture their fermionic statistics. With the above algebra, and in close analogy to the island phase- and charge-variables in Eq. (2.26), a phase-exponential operator $e^{\pm i\phi_j(x)}$ describes creation (annihilation) of a charge in lead j. This charge is centered at position x, and after integration over the lead-charge density $\rho_j(x) \sim \partial_x \theta_j(x)$, the total lead-charge field $\sim \theta_j(x' \geq x)$ experiences a shift by one unit.
The description of lead fermions via bosonization in Eq. (3.4) thus is in full analogy to the separation of phase- and charge-variables from the fermionic sector on Majorana islands. By switching to this analogue language for islands and leads, the physical processes coupling both often become more transparent. A remaining difference is that lead variables $\phi(x), \theta(x)$ are given as one-dimensional bosons, while those on the islands are local, zero-dimensional objects φ, Q in Eq. (2.26). Instead of charging energy, the only Hamiltonian term appearing for lead bosons then is a kinetic energy contribution, where we write

$$H_{\mathrm{lead,j}} = \frac{v_F}{2\pi} \int_{-\infty}^{0} dx [(\partial_x \phi_j)^2 + (\partial_x \theta_j)^2] \ . \tag{3.5}$$

Here v_F is the Fermi velocity in lead j, and integration runs over the full lead at $x \leq 0$. At $x = 0$, for decoupled leads, we have open boundary conditions where left- and right-movers coincide, $\psi_{j,R}(0) = \psi_{j,L}(0)$. In Eq. (3.4) this condition implies $\theta_j(x = 0) = 0$, which physically means that there is no net charge accumulation at the contact point where the lead terminates. The lead boundary-fermion operators in Eqs. (3.3) hence are written as

$$\Psi_j^\dagger \sim \kappa_j e^{i\Phi_j} \ , \quad \text{with} \quad \Phi_j = \phi_j(0) \ ; \quad \Theta_j' = \partial_x \theta_j(x = 0) \ , \tag{3.6}$$

i.e., uppercase symbols denote *boundary fields* at $x = 0$. For the remainder of our discussion we focus on these variables, where only the *boundary phase fields* Φ_j or *charge densities* Θ_j' enter in the *boundary Hamiltonian* describing tunneling at the islands or junctions. Fermions in each wire experience the outside world only once, namely due to the *boundary coupling* to the box at $x = 0$, and via that island or box also to other leads or islands.
Translating H_λ in Eq. (3.3) into the bosonic language yields

$$H_\lambda = \lambda_{jk} \kappa_j \gamma_k e^{i(\Phi_j - \varphi_k)} \ + \ \text{h.c.} \ . \tag{3.7}$$

For general Majorana islands, in many cases, the separation into charge-neutral fermions and bosonic variables is *not* a tautology. Instead, it elegantly affords the correct *physical* basis for describing transport in strongly-coupled Majorana systems. A prime example is the topological Kondo effect (TKE) (Béri and Cooper, 2012; Altland and Egger, 2013; Béri, 2013), arising in multi-terminal devices contacted by simple lead-Majorana junctions.

A *simple* lead-Majorana junction here means that a MBS γ_k on a given box with phase variable φ_k is contacted by only one lead j, cf. Fig. 3.1 below. At the same time lead j with Klein factor κ_j and boundary phase-field Φ_j only couples to one MBS k, i.e., their relation is monogamous. The combined-fermion parity $i\kappa_j\gamma_k = \pm$ in Eq. (3.7) then is conserved, and tunneling at that contact point becomes a purely bosonic problem. We note

$$H_{\text{simple}} = -i\lambda_{jk} e^{i(\Phi_j - \varphi_k)} \ + \ \text{h.c.} \ = \ \lambda_{jk} \sin(\Phi_j - \Phi_k) \ , \tag{3.8}$$

up to phases. Due to gauge freedom for the lead-j bosons, λ_{jk} can be chosen real positive.

The strategy of combining Majoranas and Klein factors into locally conserved fermion-sites was dubbed *Majorana-Klein fusion* by Béri (2013). It implies the choice of an entangled fermion-basis between coupled leads and island Majoranas. For the Coulomb-blockaded TS wire in Sec. 2.4.2, both the two-Majorana parity on the box (states $n_f = 0,\ 1$) and the combined fermion-parity of the attached QDs/leads are conserved separately. Physically, this results in resonant charge-transport for near charge-degenerate two-terminal islands (Fu, 2010), but Coulomb-blockade at integer gate parameters (Hützen *et al.*, 2012).
The TKE is thus reserved to multi-terminal Majorana boxes with $M \geq 3$ leads, where fermion-parity conservation between any two Majoranas or any two Klein factors (leads) is broken. Resulting low-energy physics and transport features, based on the islands residual fermionic degeneracy under Coulomb-blockade, are discussed below. Since the MFs can

be represented by a SO(M) algebra in Sec. 2.2, making connection to conventional Kondo effects (Gogolin *et al.*, 2004) or quantum-information applications in Chapter 4 is natural.

To exemplify the physics of TKE, consider the co-tunneling regime for a single box (φ, Q) in contact to M leads. Integrating out charge-fluctuations $e^{\pm i\varphi}$ in Eq. (3.8) gives an effective theory in the lead boundary phase-fields $\Phi_{j=1,\ldots,M}$ as (Béri, 2013; Altland and Egger, 2013)

$$H_K = -\sum_{j\neq k} J_{jk} \cos(\Phi_j - \Phi_k) \ . \tag{3.9}$$

Here $J_{jk} \sim \lambda_j \lambda_k / E_c$ are real, positive co-tunneling amplitudes, as in Sec. 2.4.2, Eq. (2.32). The cosine potential for the lead-boundary phase fields $j,\ k$ encodes a phase-exponential $e^{i(\Phi_j - \Phi_k)}$ and its hermitian conjugate, describing charge transport by co-tunneling between the two leads. In Sec. 3.2.1 below, we discuss how couplings J_{jk} renormalize when going to low frequencies or temperatures. Finally, in Sec. 3.2.2, H_K is found to also describe the strong-coupling low-temperature fixed-point of the TKE.

3.2 Effective low-energy description

In this section, we develop a further reduced and effective low-energy theory that captures the most relevant physical aspects of the system. This theory should be justified when going to *low frequencies* ω, that is if reference energies such as the temperature T or applied bias voltages V_j in the leads are small against contributions of the boundary Hamiltonian. In a sense, we then are interested in the "true" quantum-mechanical ground state that is reached at zero temperature, and that is shared between islands and leads. Such a description often is referred to as *strong-coupling theory* or *-solution*, since the boundary coupling between boxes and leads dominates the low-energy physics. In contrast, at high frequencies or weak coupling, the lead-fermion and box variables show weak correlations. Their states then are well described by thermal-, gate- or voltage-controlled distribution functions (Bruus and Flensberg, 2016) that are only weakly altered by tunneling.

3.2.1 Renormalization-group theory

Our first step towards an effective low-energy description is renormalization-group theory (RG) as pioneered by Wilson (1975). The general scheme comprises a renormalization of scales (space, time, fields, ...), and identification of self-similar structures that re-appear on larger scale in a physical system. The idea is that "small-scale" properties are less important or washed out in many physical observables, and instead the coarse-grained "large-scale" description gives an at least qualitatively good understanding of the physics. The particular method we seek to apply is time- or frequency-shell RG, which is a variant of perturbation theory for systems with continuous excitation spectra. For a detailed discussion, we refer to the introductions in Altland and Simons (2010); Gogolin *et al.* (2004).

Here we rather give the broad picture of ideas and concepts behind the RG method, and discuss application recipes in terms of the TKE model mentioned in Sec. 3.1.1.
First, recall that we projected out conserved fermion parities and integrated out charge fluctuations in Sec. 3.1.1, cf. also Sec. 2.4.2. The latter step already reflects a reduction towards an effective theory, where we take the remaining energy scales of lead electrons to be small against charging energy. This equivalently can be seen as a coarse-graining approach, where we forget about virtual occupations of excited charge states that last for short times $\tau_c \sim 1/E_c$. Our ansatz therefore should be justified as *effective low-energy model* at low frequencies $\omega < E_c$, or for slow dynamical time-scales $\delta\tau > \tau_c$.
We now want to focus on the most relevant low-energy degrees of freedom also for the leads. However there is a fundamental problem in applying standard perturbative methods: the leads are normal-conducting (metallic) electron reservoirs, i.e., they have an approximately constant density of states over a wide range of energies (Bruus and Flensberg, 2016). We hence are unable to define a "high-energy" and "low-energy" sector that are separated by a large gap ΔE. This is in contrast to the case of box charge states, cf. Sec. 2.4.2, where in floating islands distinct charge states are energetically split by charging energy, $\Delta E \sim E_c$.

In *time-* or *frequency-shell RG*, the idea now is to define a high-energy cut-off D beyond which all lead-fermion states are regarded to be high-energy states. A-priori the choice of cutoff is arbitrary, though in our TKE setting we pick $D_0 < E_c$ since we already integrated out charge-fluctuations at energies E_c. The reduction to a low-energy theory at small frequencies $\omega < D$ can now be made systematic by investigating how the system behaves under rescaling or *renormalization* of the cutoff $D(\ell)$,

$$D_0 \;\rightarrow\; D(\ell) \;=\; D_0 e^{-\ell} \quad , \tag{3.10}$$

with renormalization flow parameter ℓ. The choice of a logarithmic renormalization scheme turns out to be convenient in the analysis of RG flow equations below. Through downward renormalization of the high-energy cutoff D, we gradually reduce what is seen as low-energy sector of the system. Equivalently, we increase the short-time cutoff $\tau_{c,0} \to \tau_c(\ell) = D_0^{-1} e^{\ell}$, where high-energy fermion states can only be virtually occupied for short times $\delta\tau < \tau_c$. We now are set to integrate out high-energy lead-fermion states that live at energies $\omega > D(\ell)$, blurring out fast processes that happen on time scales $\delta\tau < \tau_c(\ell)$.

For the boundary Hamiltonian with couplings between different leads, cf. Eq. (3.9), under the RG flow in Eq. (3.10), there are two distinct scenarios. First assume we combine two co-tunneling events $\sim J_{jn}, J_{nk}$, at slightly delayed times τ and τ', that comprise an intermediate excitation of high-energy fermion states in lead n. As the intermediate state is only virtually occupied for times $|\Delta\tau| = |\tau - \tau'| < \tau_c$, in our coarse-grained view of time, we are unable to detect this fluctuation. We write a *contraction* of operators

$$J_{jn} e^{i(\Phi_j(\tau) - \Phi_n(\tau))} \times J_{nk} e^{-i(\Phi_n(\tau') - \Phi_k(\tau'))} \;\sim\; J_{jn} J_{nk} e^{i(\Phi_j(\bar\tau) - \Phi_k(\bar\tau))} \;, \tag{3.11}$$

with $\bar\tau = (\tau + \tau')/2$. Since we are interested in slow time-scales $\delta\tau > \tau_c$, we integrated out the intermediate step and obtained an effective process that directly implements the combined co-tunneling event between leads j and k. Instead, if the intermediate state in lead n is at energies $\omega < D$, it can be occupied for long times $|\Delta\tau| > \tau_c$. We then consider the two tunneling processes as independent events in the low-energy sector. In each renormalization step $\ell \to \ell' = \ell + \delta\ell$ in Eq. (3.10), we therefore integrate out virtual excitations only in the *frequency shell* $D(\ell') \leq \omega < D(\ell)$ or *time shell* $\tau_c(\ell) < |\Delta\tau| \leq \tau_c(\ell')$.

The precise way of performing the integrations in Eq. (3.11) involves methods of quantum field theory, including Wick contractions and the operator-product expansion. We delegate these technical aspects to Altland and Simons (2010); Gogolin *et al.* (2004). Due to the contraction of two phase-exponential operators that encode a charge-fluctuation at lead n in Eq. (3.11), for example, phase-field correlation functions like $\sim \langle \Phi_n(\tau)\Phi_n(\tau')\rangle$ enter the evaluation. Expectation values here are taken with respect to the free Hamiltonian $H_{\mathrm{lead},n}$ in Eq. (3.5), i.e., we assume that initially the leads are weakly-coupled via the island.
We note that the integration over high-energy states after a differential reduction of the cutoff $D(\ell)$ proceeds via arbitrarily small steps $\delta\ell$ in Eq. (3.10). The change of coupling parameters due to the feedback mechanism in Eq. (3.11) can then be paraphrased through differential equations. We use the RG flow parameter $\ell = \ln(\tau_c)$, cf. Eq. (3.10), where $\ell \to \infty$ indicates going to low energies (slow dynamics). The RG flow equations for the TKE with boundary Hamiltonian in Eq. (3.9) are (Altland and Egger, 2013; Béri, 2013)

$$\left(\frac{dJ_{jk}}{d\ell}\right)_{j\neq k} = \sum_{n\neq j,k} J_{jn}J_{nk} \quad , \tag{3.12}$$

where we absorbed some constants. The RG equations are understood as discussed above: tunneling between any two leads $j \neq k$ is enhanced upon going to lower energies, as we can combine consecutive co-tunneling events which excite a high-energy intermediate state in some lead $n \neq j,\ k$. Without loss of generality, we can choose $J_{jk} > 0$ as initial parameters in the weak-coupling Hamiltonian in Eq. (3.9). Since all couplings feed back into each other, the RG equations in Eq. (3.12) imply a flow to strong, isotropic couplings $J_{jk} \simeq J$. Taking this simplification, we find growing $dJ/d\ell = (M-2)J^2$ where M is the number of attached leads at the island. For $M = 2$, there is no RG flow as in Eq. (3.12) and the co-tunneling couplings J are not enhanced as one goes to low energies; the TKE only arises in multi-terminal islands with $M \geq 3$, cf. also the discussion in Sec. 3.1.1.

An important aspect for the simplicity of the TKE RG equations in Eq. (3.12) was that the contraction of any two lead boundary-coupling operators, each containing two phase-exponentials in Eq. (3.11), gives back another boundary operator of similar kind. In this sense, the Hamiltonian in Eq. (3.9) already contains all qualitatively distinct, relevant operators that can arise in the boundary-coupling theory of the TKE. There are no new, different operators that are generated in the RG analysis and have to be included.
In fact, our ability to find a closed set or *group* of most relevant operators that enter the RG flow and boundary-coupling Hamiltonian is of crucial importance for the usefulness of the renormalization-group approach. (That's why it enters in the name of the method!)

In general systems, there is no guarantee that there exists a finite number of “relevant” physical processes, described by a closed set of operators (and associated Hamiltonian terms). Only if we identify such a group of operators, we are able to analyze a finite set of RG equations that describe feed-back mechanisms between them via renormalization of their coupling amplitudes, cf. Eq. (3.12). By integrating the RG equations (for $\ell \to \infty$), we can find out which couplings grow large quickest and dominate as we reduce to lower energies. In turn, this allows us to write a tentative strong-coupling theory containing the most relevant physical processes and degrees of freedom, cf. Sec. 3.2.2 below.

This discussion also illustrates why RG methods are so tremendously successful in the analysis of quantum impurity problems (Gogolin *et al.*, 2004). As for TKE, in such systems one or multiple species of fermions or bosons interact at fixed points with an impurity. The latter usually defines a fixed set of rules by which it can interact with the reservoirs; these range from charge- or spin-conservation in tunneling to more exotic symmetries of the problem at hand. Based on such rules, one identifies allowed operators and Hamiltonian terms that couple impurity and reservoirs. For those one can perform the RG analysis, derive flow equations, and find the most relevant low-energy degrees of freedom.
The TKE-impurity is the “spin” defined on a Majorana box, cf. Sec. 2.2, and interactions happen only at the lead-boundaries, at $x = 0$. Allowed processes are defined by the box layout, and any but the simple couplings in Eq. (3.8) are precluded by non-locality and the (topological) protection of Majoranas; hence the name *topological* Kondo effect.
In Plugge *et al.* (2016b); Gau *et al.* (2018), we extend Majorana box transport problems beyond the case where a purely bosonic theory in Eq. (3.8) is applicable. Local multi-junctions between leads and Majoranas allow for less protected couplings, and the ensuing low-energy physics will depend on those parameters. Nevertheless, since these setups are built from coupled Majorana boxes that serve as “quantum impurities”, RG analysis provides powerful insights into the most relevant physics at low energies, cf. Sec. 3.3.

3.2.2 Strong-coupling theory of Majorana boxes

After performing a weak-coupling RG analysis in Sec. 3.2.1, we now are set to write down a tentative strong-coupling theory at low energies. A fixed-point in the weak-coupling RG of Eq. (3.9) is identified as a limit to which the corresponding RG equations (3.11) flow.
In general, tentative strong-coupling fixed-points do not need to be stable. A reason for this can be a lack of information about the “true” low-energy physics in the original weak-coupling theory on which we performed the RG. We recall that the weak-coupling RG approach in Sec. 3.2.1 was based on initially weakly-coupled leads, i.e., in absence of strong correlations between the leads (working in the original decoupled-leads basis).
If we are after strongly-correlated low-energy states like the (topological) Kondo effect, naturally, we then have to perform a separate strong-coupling analysis. To this end, a relation between multi-channel Kondo effects and quantum Brownian motion in periodic potentials by Yi and Kane (1998); Yi (2002) is essential. It shows that the TKE fixed point indeed is stable, and describes a so-called non-Fermi liquid state that reveals itself

in unconventional finite-temperature and -voltage corrections of conductance and other physical observables. Here and in the following we discuss only fixed-point theories, with an understanding that they are stable and indeed describe physical low-energy states of the system. For corrections around the fixed point and further discussion, we refer to the extensive literature on the TKE, e.g. Béri and Cooper (2012); Altland and Egger (2013); Béri (2013); Zazunov *et al.* (2014); Béri (2017) and Plugge *et al.* (2016b); Gau *et al.* (2018).

For the TKE, in Sec. 3.2.1 we have identified the limit of strong, isotropic co-tunneling couplings as tentative fixed point. We reproduce the boundary Hamiltonian in Eq. (3.9),

$$H_K = -J \sum_{j \neq k} \cos(\Phi_j - \Phi_k) \ . \tag{3.13}$$

The energy scale controlling the flow to strong coupling is the so-called Kondo temperature. It can be estimated from the point where couplings J reach magnitude ~ 1 in integration of the flow equations $dJ/d\ell = (M-2)J^2$, and the validity of our weak-coupling RG analysis breaks down. We find $T_K \simeq D_0 e^{-1/(M-2)J}$ with high-energy cutoff $D_0 \leq E_c$ in Eq. (3.10). While we assumed isotropic couplings to obtain this simple form, J can also be taken as mean magnitude in the case of moderately anisotropic initial couplings.
At energy scales below T_K, we observe that H_K defines a strong pinning-potential for the lead phase-field differences in Eq. (3.13). The low-energy solution for the TKE then is accessible by a quasi-classical picture where all phase-differences $\Phi_j - \Phi_k$ are frozen out, and only their center-of-mass (com) variable $\Phi_0 = \frac{1}{\sqrt{M}} \sum_{j=1}^{M} \Phi_j$ stays free. We note that $H_K[\Phi_j]$ is invariant under shifts along the com-direction $\sim \Phi_0$. It then is instructive to switch to a new basis of phase-fields $\tilde{\Phi}_j$ and com-phase Φ_0, where

$$\Phi_0 = g_0 \sum_{j=1}^{M} \Phi_j \quad , \qquad \tilde{g}_j \tilde{\Phi}_j = \Phi_j - g_0 \Phi_0 \quad , \tag{3.14}$$

with prefactors $g_0 = 1/\sqrt{M}$ and $\tilde{g}_j = \sqrt{2(M-1)/M}$. Note that while $\tilde{\Phi}_j$ is orthogonal on Φ_0, the M fields $\tilde{\Phi}_j$ are not orthogonal to each other: the new basis $\{\Phi_0, \tilde{\Phi}_j\}$ is over-complete, and we additionally impose the zero-com constraint $\sum_j \tilde{\Phi}_j = 0$ by construction. Strong couplings J result in quasi-classical pinning of the $M-1$ phase differences $\tilde{\Phi}_j - \tilde{\Phi}_k$, and imply that charges fluctuate freely between leads. The only free quantum variable then is the com-phase Φ_0 that describes simultaneous, collective transport from/to all M leads attached to the Majorana island hosting the TKE. A physical observable reflecting these collective transport processes is given by the zero-bias zero-temperature conductance of a TKE Majorana box (Altland and Egger, 2013; Béri, 2013; Zazunov *et al.*, 2014)

$$G_{jk} = \frac{2e^2}{h} \left(\delta_{jk} - \frac{1}{M} \right) \ . \tag{3.15}$$

Electrons incident from lead j experience resonant, correlated Andreev reflections (AR) due to the residual fermionic degeneracy of the island. A Cooper pair (charge $2e$) absorbed at

lead j upon resonant AR is split democratically among all leads, i.e., each lead participates by absorbing charge $2e/M$. In a sense, at low temperatures the island thus rejects single-electron tunneling or standard AR. Instead it implements processes $e^{\mp i\tilde{g}_j\tilde{\Phi}_j} \sim e^{\mp i(\Phi_j - g_0\Phi_0)}$ that involve balanced splitting of charge among the leads, described by a phase-exponential of their free com-phase variable. The conductance at each lead then is the conductance quantum (e/h) times the net transferred charge, giving the result in Eq. (3.15) above.
Such reduced, collective variables and transport mechanisms are key to our analysis of more general Majorana box networks below. As we will see, it then is instructive to introduce *bosonic subsectors* for simply-coupled Majorana boxes, where transport between distinct subsectors happens only via their respective com-phase variables.

3.3 Non-simple lead-Majorana multi-junctions

In many Majorana devices and networks, there exist local tunnel-junctions between multiple leads and/or Majoranas, see Figure 3.1. We dub these more complicated multi-junction geometries non-simple, in contrast to the simple lead-Majorana junctions of Eq. (3.8). For the design of quantum-computing architectures in Chapter 4, non-simple multi-junctions are unavoidable. They facilitate access to distinct Pauli-operator components in Majorana-based qubits and networks, thus allowing for qubit measurements and manipulations.
In this section we introduce two pedagogical examples of accidental or intentional lead-Majorana multi-junctions, see Fig. 3.1, that are investigated in detail in published works. Apart from providing a comprehensive overview of the main ideas entering the analysis of such junction geometries, we also summarize general results and conclusions for more complicated networks in Sec. 3.4 below. Since the later work Gau *et al.* (2018) revisits the two-Majorana single-lead setup of Plugge *et al.* (2016b), we combine their discussion.

3.3.1 Two Majoranas coupled to single lead: the loop qubit

We start with two Majoranas coupled to a single lead on an otherwise simply-coupled box, see Fig. 3.1. This scenario can model accidental low-energy states at lead-Majorana contacts, dubbed "quasi-particle poisoning" in Plugge *et al.* (2016b), and a similar setup was investigated by Kashuba and Timm (2015). Recently, the *loop qubit* of Karzig *et al.* (2017) is a three-terminal device with a single central lead "c" coupled to two MFs $\gamma_{x,y}$, and two (or more) simply-coupled leads for the rest of the box, cf. Fig. 3.1. Measurements at the central lead (or quantum dot) then should allow to determine the joint-parity eigenvalues $\sigma_z = i\gamma_y\gamma_x = \pm$ of the two central MFs. In turn one can hope to probe topological-qubit features on this Majorana box, cf. Chapter 4. Devices like the loop qubit constitute minimalistic but doable realizations of Majorana physics beyond the simpler two-terminal measurements of Albrecht *et al.* (2016), and are of strong current interest in theory and experiment. It hence is of critical importance to achieve a detailed understanding of the low-energy physics and quantum transport phenomena in lead-Majorana multi-junctions, which was our goal in Plugge *et al.* (2016b); Gau *et al.* (2018).

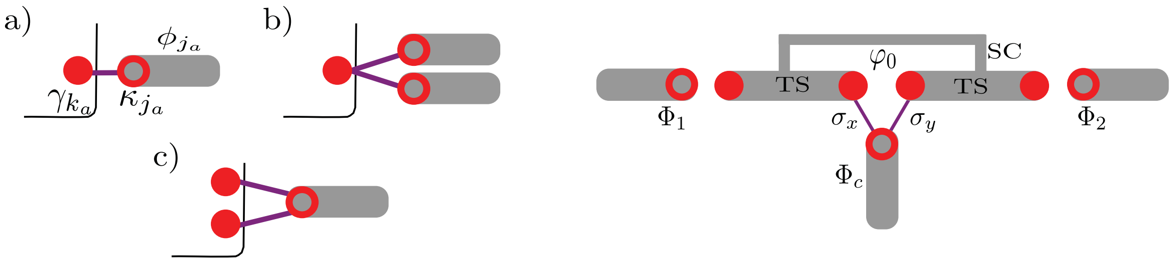

Figure 3.1: Lead-Majorana multi-junctions. a), simple junction between one Majorana γ (red dot) hosted on a box (outlined), and one lead contact (grey) with Klein factor κ (red circle) and lead phase-field ϕ. b) and c), non-simple junctions with one Majorana coupled to two leads, and vice-versa. Right: loop qubit device (Karzig *et al.*, 2017) with a central multi-junction as in c), and two simple outer junctions as in a). A superconducting bridge (SC) connects the TS wire segments into a single box with 4 MFs, and forms a phase-coherent loop in the system. Insertion of magnetic flux φ_0 then allows to tune transport properties of the device. Two MFs and one Klein-MF at the central junction are represented by components of a spin $\vec{\sigma}$, cf. Eq. (3.16). Figures from Gau *et al.* (2018).

Following Sec. 3.1, all simple junctions in Fig. 3.1 afford a purely bosonic description, while for the central multi-junction this is not true anymore. However, any charge out/in-tunneling $e^{\mp i\Phi_c}$ at the central lead c conserves the junctions overall fermion-parity due to simultaneous in/out-tunneling at one of the two MFs. Therefore a representation of the two MFs $\gamma_{x,y}$ and one Klein-MF κ_c of the central lead via a spin becomes possible. For m MFs, the latter corresponds to a SO(m) real spin-object living at the junction, cf. Sec. 2.2. Here, for $m = 3$ MFs that are constrained in their overall parity, we retain a single spin $\vec{\sigma}$. We note the junction Hamiltonian at the central lead in Fig. 3.1 as

$$H_{\text{central}} = \left(\lambda_x\sigma_x + \lambda_y e^{i\varphi_0}\sigma_y\right) e^{i(\varphi-\Phi_c)} \; + \; \text{h.c.} \; , \tag{3.16}$$

with Pauli operators $\sigma_{x,y} = i\kappa_c\gamma_{x,y}$. Amplitudes $\lambda_{x,y}$ are real positive, and we extracted the loop-phase parameter φ_0 that is identified with a magnetic flux piercing the device in Fig. 3.1. It is convenient to switch to Pauli operators $\sigma_\pm = (\sigma_x \pm i\sigma_y)/2$, where

$$H_{\text{central}} = (\lambda_+\sigma_+ + \lambda_-\sigma_-)\, e^{i(\varphi-\Phi_c)} \; + \; \text{h.c.} \; , \quad \text{with} \;\; \lambda_\pm = \lambda_x \mp i\lambda_y e^{i\varphi_0} \; . \tag{3.17}$$

In order to obtain a simplified description, we now employ co-tunneling perturbation theory as in Sec. 2.4.2 and for the TKE above. However, because of the local spin $\vec{\sigma}$ at the central junction, there are qualitatively new terms in the boundary theory. Including all RG-relevant contributions, we then find an effective boundary-coupling Hamiltonian as

$$H_c = -J \sum_{j\neq k\in\mathcal{B}} \cos(\Phi_j - \Phi_k) \; - \frac{1}{\sqrt{2}} \sum_{j\in\mathcal{B}} \left[(L_+\sigma_+ + L_-\sigma_-)e^{i(\Phi_j-\Phi_c)} + \text{h.c.}\right] \; - \Lambda\sigma_z\Theta_c' \; . \tag{3.18}$$

Tunneling within a *bosonic subsector* $\mathcal{B}$ of simply-coupled leads $j = 1, ..., M$ does not affect the spin, and we have terms $\sim J$ connecting leads $j \neq k \in \mathcal{B}$ as before, cf. Eq. (3.13).

Similarly, there are processes that describe co-tunneling from the central lead c to simply-coupled leads $j \in \mathcal{B}$ of the bosonic subsector. However these events now necessarily affect the spin at the central junction, where we have two path-options $L_\pm \sim \lambda\lambda_\pm/E_c$ with distinct spin-operator content $\sigma_\pm$, cf. Eq. (3.17). Finally, because there exists a *closed loop* that permits fluctuations in the spin-sector while leaving lead- and island-charge states invariant, we obtain *spin-density hybridization* terms. In the loop qubit of Fig. 3.1, the closed loop encircles a (virtual) magnetic flux φ_0, which hence becomes a gauge-invariant quantity that affects the low-energy physics of the system. The hybridization term in Eq. (3.18) is qualitatively new compared to the TKE, and comprises an interaction between the Majorana pair $\sigma_z = i\gamma_y\gamma_x$ and the boundary-charge density $\rho_c \sim \Theta_c'$ of lead c.

Detailing the generation of interactions Λ is useful also to understand their renormalization. It here suffices to consider only the central-junction Hamiltonian in Eq. (3.16), where a closed loop is formed by two non-equivalent tunnel paths $\sim \lambda_\pm$ that invoke the same charge dynamics. Upon contraction of two slightly delayed tunneling events $\sim \sigma_{s=\pm}$ at times τ and τ', in time-ordered perturbation theory (Altland and Simons, 2010) we obtain

$$\mathcal{T}\left[\sigma_s(\tau)\cdot\sigma_{-s}(\tau')\right] \;\sim\; 1 + s\,\operatorname{sgn}(\Delta\tau)\sigma_z(\bar{\tau})\;, \tag{3.19}$$

with $\Delta\tau = \tau - \tau'$ and $\bar{\tau} = (\tau+\tau')/2$. Since $\sigma_s^2 = 0$, only above terms $\sim |\lambda_\pm|^2$ contribute. The second term in Eq. (3.19) contains a sign-function, making it odd under integration of the time difference $\Delta\tau$ over the time shell $0 \le |\Delta\tau| \le \tau_c$ with short-time cutoff $\tau_c \sim E_c^{-1}$. (This time-shell integration is a field-theoretical variant of co-tunneling perturbation theory in Sec. 2.4.2; it is identical to a single step of the differential time-shell integration in the RG-analysis of Sec. 3.2.1 and below, with fixed cutoff τ_c.) To obtain a non-vanishing contribution, we then have to produce an odd-in-$\Delta\tau$ dependence also from the bosonic operator-content of the contraction. For boson-dynamics as triggered by Eq. (3.17), an expansion of the phase-exponentials that describe charge-tunneling events gives

$$e^{i(\varphi(\tau)-\Phi_c(\tau))}\cdot e^{i(\Phi_c(\tau')-\varphi(\tau'))} \;\sim\; \left[1+\Delta\tau\cdot i\partial_{\bar{\tau}}\varphi(\bar{\tau})\right]\cdot\left[1-\Delta\tau\cdot i\partial_{\bar{\tau}}\Phi_c(\bar{\tau})\right]\;. \tag{3.20}$$

The leading constant-in-$\Delta\tau$ term does not produce relevant contributions when combined with the first term of the spin-operator contraction in Eq. (3.19) (no left-over operators). Similarly, combined with the sign-function of the second term it vanishes under time-shell integration. Last, matching the two sub-leading time-derivative terms in Eq. (3.20) generates density-density terms that are strongly irrelevant in RG. The only RG-relevant contribution from Eq. (3.20) then comes from pairing terms $\sim \Delta\tau$ with the sign-function in Eq. (3.19), where integration over the time-shell $|\Delta\tau| \le \tau_c$ gives a cutoff-factor $1/E_c$. Using the chiral-boson identity $-i\partial_\tau\Phi_c = \partial_x\Theta_c = \Theta_c'$, relating the above phase-dynamics to a boundary-charge density (Gogolin *et al.*, 2004), we find that one generates spin-density hybridizations $\sim \sigma_z\Theta_c'$ as already noted in the boundary Hamiltonian H_c in Eq. (3.18). Similarly, we have $-i\partial_\tau\varphi(\tau) = Q$ for the box boson-variables in Sec. 2.4. After projection to the charge ground-state $Q \to \langle Q\rangle = \Delta n_g$ with gate-detuning $\Delta n_g \ll 1$, we find a term $\sim \sigma_z\Delta n_g$. The latter does not renormalize under RG, and hence is dropped in H_c.

We note that because of the spin-index s in Eq. (3.19), contributions $\sim |\lambda_{s=\pm}|^2$ come with opposite signs. The initial value of the spin-density hybridization Λ, entering in the RG flow equations below, then follows as $\Lambda(\ell = 0) \sim (|\lambda_+|^2 - |\lambda_-|^2)/E_c \sim (\lambda_x \lambda_y / E_c) \sin(\varphi_0)$. Crucially it depends on the coupling-amplitudes *and* loop-phase in Eqs. (3.16) and (3.17).

We now analyze how couplings of the boundary Hamiltonian in Eq. (3.18) renormalize under RG, employing the same quantum field-theoretical methods as in Sec. 3.2.1. After the above discussion of contractions and time-shell integration for tunneling events with non-commuting spin-operators, the RG flow equations follow as (Gau *et al.*, 2018)

$$
\begin{aligned}
\frac{dJ}{d\ell} &= (M-2)J^2 + |L_+|^2 + |L_-|^2 \ , \\
\frac{dL_\pm}{d\ell} &= \left[(M-1)J \pm \Lambda\right] L_\pm \ , \\
\frac{d\Lambda}{d\ell} &= (M+1)\left(|L_+|^2 - |L_-|^2\right) \ .
\end{aligned}
\tag{3.21}
$$

The flow of subsector-couplings J is as in the TKE, cf. Eq. (3.12), where we now have two additional options $\sim |L_\pm|^2$ of co-tunneling via the central lead c. Likewise, tunneling $\sim L_\pm$ between the central lead c and $j \in \mathcal{B}$ is enhanced due to $M-1$ options of first tunneling from lead c to a different lead $n \neq j \in \mathcal{B}$, followed by subsector-transition $n \to j$ with amplitude $\sim J$. Processes $\sim |L_\pm|^2$, comprising back-and-forth tunneling between leads $j \in \mathcal{B}$ and c, enhance the spin-density hybridization Λ. Due to their spin-operator content, the two contributions enter into Λ with opposite sign, see the discussion above. By a similar analysis as in Eqs. (3.19) and (3.20), the hybridization also feeds back into couplings $L_\pm$, again with opposite signs for spin-flip directions $\sim \sigma_\pm$.

One can now access the systems low-energy physics by the RG flow of the loop phase $\varphi_0(\ell)$. The latter is encoded in couplings $L_\pm \sim \lambda_\pm = \lambda_x \mp i\lambda_y e^{i\varphi_0}$, cf. Eq. (3.17), and we find

$$
\varphi_0(\ell) = \arg[i(L_+ - L_-)/(L_+ + L_-)]_\ell \ . \tag{3.22}
$$

By convention we take $\lambda_{x,y} > 0$ as real and positive, where the only gauge-invariant and physical phase in the system is φ_0. Further it is sufficient to consider bare initial loop phases $\varphi_0 \in [0, \pi)$. Together this implies $|L_+(\ell)| \geq |L_-(\ell)|$ and $\varphi_0(\ell) \in [0, \pi)$ throughout.

Inspecting the RG flow in Eqs. (3.21), we note that the coupling J is independent of φ_0 and grows strong as we go to low energies ($\ell \to \infty$). For $M \geq 3$ it benefits from a TKE-like self-enhancement. The spin-density hybridization is enhanced by couplings $L_\pm$, following $\Lambda(\ell) \sim \sin[\varphi_0(\ell)]$, and grows strong and positive for $\varphi_0 > 0$. Due to spin-selective feedback into $L_\pm$, the hybridization then further enhances L_+ while suppressing the opposite coupling L_-. In total, couplings J, L_+ and Λ become strong, while L_- is suppressed. The phases of couplings $L_\pm$ are fixed, since both J and Λ are real and positive. For the loop-phase $\varphi_0(\ell)$ in Eq. (3.22) this implies a flow to the asymptotic fixed-point value $\varphi_0 \to \pi/2$.

An exception is the fine-tuned value $\varphi_0 = 0$, where the hybridization $\Lambda \to 0$ is absent. Rewriting in terms of couplings $J_x = (L_+ + L_-)$ and $J_y = i(L_+ - L_-)$ to the original central-junction Majoranas $\gamma_{x,y}$, cf. Eqs. (3.16) and (3.17), the flow equations (3.21) translate to

$$\frac{dJ}{d\ell} = (M-2)J^2 + \sum_{a=x,y} J_a^2 \quad , \quad \frac{dJ_a}{d\ell} = (M-1)JJ_a \quad , \tag{3.23}$$

Importantly, while both $J_{a=x,y}$ grow, their ratio $dJ_x/dJ_y = J_x/J_y$ follows from that of the fundamental couplings $\lambda_{x,y}$ in Eq. (3.16) and stays fixed throughout the flow. For $M \geq 3$ the subsector-coupling J experiences a self-enhanced RG flow as before.

For the loop qubit system in Fig. 3.1 and Eq. (3.18) we thus have identified two candidate fixed-points with loop-phase pinning to different values. The latter value $\varphi_0 = 0$ is fine-tuned and unstable against variations of the phase $\delta\varphi_0 \neq 0$. Instead $\varphi_0 = \pi/2$ represents a stable phase-flow fixed point that is approached for arbitrary initial value $\varphi_0 \in (0, \pi)$, where the fixed-point theory was investigated in Plugge *et al.* (2016b).

3.3.2 Low-energy quantum transport in the loop qubit device

After identification of candidate strong-coupling fixed-points in Sec. 3.3.1, we now explore the low-energy physics and quantum transport features of the loop qubit device in Fig. 3.1. To this end we employ simplification strategies as developed by Nayak *et al.* (1999) for resonant tunneling between multiple boson species. Similar ideas were used by Béri (2017) to obtain exact non-equilibrium transport results for the TKE.

In our case, once co-tunneling couplings J between simply-coupled leads $j \neq k \in \mathcal{B}$ grow strong, we can reduce the bosonic subsector $\mathcal{B}$ to its com-phase variable $\Phi_{\mathcal{B}} = g_{\mathcal{B}} \sum_{j\in\mathcal{B}} \Phi_j$. Here $g_{\mathcal{B}} = 1/\sqrt{M}$ indicates effectively attractive interactions for this new collective-boson species (Nayak *et al.*, 1999). All relative shifts between lead boundary phase-fields $\Phi_j - \Phi_k$ in the bosonic subsector are then pinned to zero by the cosine-potentials in Eq. (3.18). A bosonic subsector therefore interacts with its environment – either individual leads or other subsectors – only via collective charge-dynamics $\sim e^{\pm i g_{\mathcal{B}} \Phi_{\mathcal{B}}}$, see also Sec. 3.2.2.

From Eq. (3.18), we write a reduced strong-coupling theory at phase-value $\varphi_0 = \pi/2$ as

$$H_c^{\varphi_0=\pi/2} = -\left[\tilde{L}_+ \sigma_+ e^{i(g_{\mathcal{B}}\Phi_{\mathcal{B}} - \Phi_c)} + \text{h.c.}\right] - \Lambda\sigma_z\Theta_c' \quad , \tag{3.24}$$

with collective coupling $\tilde{L}_+ \sim ML_+$. Terms $\sim L_-\sigma_-$ are dropped and the purely bosonic part in Eq. (3.18) is rendered constant. For the case $M = 1$, in Plugge *et al.* (2016b) we have shown that $H_c^{\varphi_0=\pi/2}$ above maps to a version of the well-known single-channel Kondo model (Gogolin *et al.*, 2004). This becomes possible since lead- and island-fermion parities in a two-terminal version of Fig. 3.1 are conserved separately. The three island-Majoranas then provide a fermion-degeneracy (represented as spin-1/2) even under Coulomb-blockade, and facilitate resonant transport between a single outer and the central lead in Fig. 3.1.

In contrast, for $M \geq 2$ outer leads only local fermion-parities are conserved, cf. Sec. 3.1.1. The spin in Eq. (3.24) then blocks any net transport at the central contact due to an onset of "helicity": each in-tunneling is followed by a subsequent out-tunneling event. However, since charge-fluctuations at the central lead break parity conservation for the remaining M island-Majoranas, Eq. (3.24) facilitates transport resonances between the outer leads. With $M = 2$ outer leads, we observe that their coupling J grows strong only based on this mechanism, cf. Eqs. (3.21). At $M \geq 3$ we instead find an enhanced TKE in the outer sector.

For a strong-coupling solution at fine-tuned $\varphi_0 = 0$, we can make progress by returning to a representation as for the central-junction Hamiltonian in Eq. (3.17). With the Pauli operators $\sigma_{x,y} = i\kappa_c\gamma_{x,y}$, after equivalent steps as those leading to Eq. (3.24), we find

$$H_c^{\varphi_0=0} = -i\kappa_c\left(\tilde{J}_x\gamma_x + \tilde{J}_y\gamma_x\right)e^{i(g_B\Phi_{\mathcal{B}}-\Phi_c)} + \text{h.c.} \quad = \quad -\tilde{J}(i\kappa_c\gamma)e^{i(g_B\Phi_{\mathcal{B}}-\Phi_c)} + \text{h.c.}\,. \tag{3.25}$$

In the last step we defined a combined MF $\gamma = (\tilde{J}_x\gamma_x + \tilde{J}_y\gamma_y)/\tilde{J}$, which together with the Klein-MF κ_c can be removed by Majorana-Klein fusion, $i\gamma\kappa_c \to \pm$. This procedure becomes possible since $\tilde{J}_{x,y}$ are real and have a fixed ratio during the flow, cf. the RG equations (3.23). At fine-tuned magnetic flux, the central lead in the loop qubit of Fig. 3.1 thus behaves like a conventional, simple lead-Majorana junction. The island then undergoes a $M_{\text{eff}} = M + 1$ - lead TKE, where in Eq. (3.25) we have artificially pulled out the central lead c. In fact this mimicks the approach of Béri (2017) to describe low-energy transport for a single biased lead "c" in a Majorana island otherwise hosting an equilibrium TKE. For fine-tuned phase $\varphi_0 = 0$, we hence have access to the full non-equilibrium transport results between lead c and the collective outer sector $\mathcal{B}$ with $M \geq 1$ leads.

Finally we summarize our predictions for the loop qubit device in Fig. 3.1. By tuning the magnetic flux φ_0 piercing its loop (Gazibegovic *et al.*, 2017; Vaitiekėnas *et al.*, 2018), one might reveal drastically different and quite non-trivial quantum transport behavior.

First, since experiments are done at low but non-zero temperatures and voltages, features of the unstable phase-flow fixed-point should widen to a region around $\varphi_0 \approx 0,\ \pi$ with small but non-zero hybridization. Around these flux-values, our theory predicts Coulomb blockade in transport between the central and a single external lead (e.g. no. 1, Fig. 3.1). This case is similar as for standard two-terminal devices (Fu, 2010; Hützen *et al.*, 2012), since the central contact effectively sees a single Majorana in Eq. (3.25). In contrast, for a multi-terminal setting with $M \geq 2$ external leads, we expect formation of the TKE with resonant transport at the central lead (Altland and Egger, 2013; Béri, 2013, 2017).

Conversely, at far-detuned flux values $\varphi_0 \neq 0,\ \pi$ with a single external lead, we predict a single-channel Kondo effect with resonant transport between leads 1 and c in Fig. 3.1. Instead now the multi-terminal setting with $M \geq 2$ external leads facilitates a strong blocking at the central contact, but allows for resonant transport between the outer leads.

3.3.3 Single Majorana with multiple leads

As second example, we briefly run through the case of a single Majorana γ coupled to multiple (two or three) leads on an otherwise simply-coupled island, cf. Fig. 3.1. Again all simple lead-Majorana junctions afford a purely bosonic description. Further since any charge-tunneling $e^{\mp i\varphi}$ at island Majorana γ conserves the junctions fermion-parity $\mathcal{P} = \gamma\kappa_x\kappa_y\kappa_z$ due to simultaneous in/out-tunneling at leads x, y or z, representation of MFs plus Klein factors by a spin is possible. The junction Hamiltonian at Majorana γ reads

$$H_\gamma = \left(\lambda_x\sigma_x e^{i\Phi_x} + \lambda_y\sigma_y e^{i\Phi_y} + \lambda_z\sigma_z e^{i\Phi_z}\right) e^{-i\varphi} \; + \; \text{h.c.} \; , \tag{3.26}$$

with Pauli operators $\sigma_a = i\gamma\kappa_a$ and Klein factor κ_a of lead $a = x, y, z$ with boundary phase-field Φ_a. Employing co-tunneling perturbation theory as before, we find the effective boundary-coupling Hamiltonian at energies $\omega \ll E_c$ as

$$H_b = -J\sum_{j\neq k=1}^{M}\cos(\Phi_j - \Phi_k) \; - \sum_{a=x,y,z} J_a\sigma_a \sum_{j=1}^{M}\cos(\Phi_j - \Phi_a) \; . \tag{3.27}$$

We assume isotropy for couplings J within the bosonic subsector $\mathcal{B}$ with leads $j = 1, ..., M$. Similarly, one can take isotropic couplings J_a from the bosonic subsector $\mathcal{B}$ to outer leads $a = x, y, z$. Since this setup does not contain any closed loops, by gauge-invariance shifts, all couplings $J_a \sim \lambda\lambda_a/E_c$ and $J \sim \lambda^2/E_c$ can be chosen real and positive.

In order to derive RG equations for couplings in H_b, we follow the same strategies as for the TKE and loop qubit, paying due attention to the presence of Pauli operators σ_a. In the contraction of two tunneling operators, pairs of anti-commuting Pauli-operators give a sign-factor, cf. Eq. (3.19), and the corresponding RG contribution vanishes. Since the setting in Eq. (3.27) does not contain closed loops, a generation of hybridizations is not possible and the resulting RG equations are simplified. We obtain (Gau *et al.*, 2018)

$$\frac{dJ}{d\ell} = (M-2)J^2 + \sum_{a=x,y,z} J_a^2 \quad , \qquad \frac{dJ_a}{d\ell} = (M-1)JJ_a \quad . \tag{3.28}$$

In absence of spin-density hybridizations, the RG equations can be understood on a purely combinatorial basis. Though in completely different context of two or three leads coupled to one Majorana, cf. (3.26), these RG equations are equivalent to those for the loop qubit at $\varphi_0 = 0$, cf. Eq. (3.23). We note that while all couplings J and $J_{x,y,z}$ grow strong, the coupling ratios $dJ_x/dJ_y = J_x/J_y$ and $dJ_y/dJ_z = J_y/J_z$ are fixed throughout the flow.
For subsector $\mathcal{B}$ with $M \geq 3$ simply-coupled leads, coupling J benefits from a self-enhanced RG flow similar to that in the TKE. Instead for $M = 2$ one recovers a multi-component version of the celebrated Kosterlitz-Thouless RG equations (Gogolin *et al.*, 2004), where $dJ/d\ell = \sum_a J_a^2$ and $dJ_a/d\ell = JJ_a$. In this case, coupling J renormalizes only due to growing $J_{a=x,y,z}$, where it also feeds back into the RG equations of these couplings.

Simplification of the boundary theory again is possible by reduction of bosonic subsectors to their center-of-mass phases. This approximation is justified at energies well below the Kondo temperature in $\mathcal{B}$, cf. Sec. 3.2.2, or for energy below J in the case of $M = 2$ leads. The reduced low-energy Hamiltonian then contains only the com-phase $\Phi_{\mathcal{B}} = g_{\mathcal{B}} \sum_{j\in\mathcal{B}} \Phi_j$, with $g_{\mathcal{B}} = 1/\sqrt{M}$, and the individual lead-phase fields Φ_a as dynamic variables. We write

$$H_b' = -\sum_{a=x,y,z} \bar{J}_a \sigma_a \cos(g_{\mathcal{B}}\Phi_{\mathcal{B}} - \Phi_a) \ , \tag{3.29}$$

where the first term in Eq. (3.27) was dropped. In each contribution $\sim J_a$ we summarized the terms for different fields $j \in \mathcal{B}$ after projection to their com-phase content, leading to the collective tunneling strength $\bar{J}_a \simeq M J_a$. H_b' in Eq. (3.29) describes tunneling from any of the three leads $a = x, y, z$ to a collective chiral boson with boundary phase-field $\Phi_{\mathcal{B}}$, formed by the M strongly-coupled leads in the bosonic subsector $\mathcal{B}$.

While drastically simpler than the full theory, H_b' in Eq. (3.29) is still a complicated problem. To make analytical progress, we consider the case $\bar{J}_z = 0$ with only two leads coupled to one MF, cf. Fig. 3.1. By rotating to new phase-field combinations $\Phi_{c,s} = (\Phi_x \pm \Phi_y)/\sqrt{2}$ for the two multi-junction leads, and after combining $g\Phi = (g_{\mathcal{B}}\Phi_{\mathcal{B}} - \Phi_c/\sqrt{2})$, we find

$$\bar{H}_b = -\frac{1}{2}\left(\Gamma_b + \Gamma_b^\dagger\right) \quad , \quad \text{with } \ \Gamma_b = \left(\bar{J}_x\sigma_x e^{-i\Phi_s} + \bar{J}_y\sigma_y e^{i\Phi_s}\right) e^{ig\Phi} \ . \tag{3.30}$$

Note the interaction parameter $g = \sqrt{g_{\mathcal{B}}^2 + 1/2}$. We observe that only the relative phase-field combination Φ_s couples to the spin in an essential way, while the new field Φ describes collective charge transport between sector $\mathcal{B}$ and the two non-simple contacts x, y. Following Emery and Kivelson (1992), a unitary rotation $U = e^{i\sigma_z\Phi_s}$ with subsequent rotating-wave approximation allows to decouple Φ_s from the boundary-coupling term Γ_b. As trade-off, since U also acts on the lead Hamiltonian $H_{\text{lead}}[\phi_s, \theta_s]$ in Eq. (3.5), we introduce interactions between σ_z and the boson species s at the junction. We finally obtain

$$H_{b,\text{full}} = H_{\text{leads}} - \frac{1}{2}\left(\Gamma_b' + \Gamma_b'^\dagger\right) + \Lambda_s\sigma_z\Theta_s' \quad , \quad \text{with } \ \Gamma_b' = \left(\bar{J}_x\sigma_+ + i\bar{J}_y\sigma_-\right) e^{ig\Phi} \ . \tag{3.31}$$

At general M this is an interacting boson problem because of $g = \sqrt{(M+2)/2M} \leq 1$. However for $M = 2$ ($g = 1$), refermionization of the spin and phase-exponential operators ($\Psi \sim \kappa e^{i\Phi}$, reverting Eq. (3.4)) allows for an exact solution. The theory in $H_{b,\text{full}}$ then describes an asymmetric two-channel Kondo model (Fabrizio *et al.*, 1995; Gogolin *et al.*, 2004). It captures collective transport between two simple leads in $\mathcal{B}$ and the two leads x, y coupled to one Majorana, cf. Fig. (3.1), in a four-lead three-terminal geometry.

3.4 Summary: Quantum transport in Majorana boxes

We now summarize the main strategies and results for tackling quantum transport problems in coupled Majorana boxes, as published in Plugge *et al.* (2016b); Gau *et al.* (2018). Of course some of the results listed below were known before, and we gave the most relevant references to our work throughout the chapter. This overview also serves as convenient step-by-step guide for the understanding of transport in complicated Majorana network settings that are relevant in quantum-information processing applications of Chapter 4. There we apply insights on the transport processes in Majorana networks to engineer current- and charge-based protected manipulation schemes for Majorana qubits.
As instructive examples, we discussed the TKE hosted in simply-coupled multi-terminal islands, cf. Secs. 3.1 and 3.2, as well as more complicated multi-junction setups in Sec. 3.3.

- Field-theoretical bosonization drastically simplifies the analysis of tunnel-coupled Majorana boxes. This technique separates bosonic charge- and phase dynamics from fermionic statistics encoded in charge-neutral Majoranas and Klein factors.

- By inspection of junction geometries and the device layout, one may employ local fermion-parity constraints. Phase-coherent tunneling that connects leads and boxes necessarily is local, unless facilitated by additional islands (see Chapter 4).

- Isolated pairs of MFs and Klein factors can be removed from the low-energy theory, their joint fermion-parities are conserved. Local sets of m MFs and Klein-MFs can be viewed as real spin-objects of group SO(m), cf. Sec. 2.2. One can represent the associated Majorana operators by $\sim m/2$ sets of Pauli-operators.

- After projecting to box charge ground-states, the theory reduces to a set of 1D boson fields coupled via several spin-objects at their junction. Near charge-degenerate boxes behave as "charge spins", cf. Herviou *et al.* (2016); Michaeli *et al.* (2017), and do not fundamentally change the theoretical description. In fact one may decouple center-of-mass boson variables attached to such islands by Emery-Kivelson-style rotations. As with many quantum-impurity problems, renormalization-group analysis provides useful tools for finding the most relevant low-energy degrees of freedom.

- Groups of leads that couple without affecting the spin-sector, i.e. their interactions are purely bosonic, can be identified as bosonic subsectors. At low energies they enter the effective description only as collective degrees of freedom, through their center-of-mass phases; such collective bosons generally harbor attractive interactions. Corrections on top of this can be included as for the TKE, see e.g. Béri (2013); Altland and Egger (2013). From a general set of coupled leads and boxes, we arrive at a theory containing only the independent bosonic subsectors and sets of Pauli operators by which those couple.

- In a setup with tunnel-loops that harbor gauge-invariant physical phases, tunneling between two subsectors can occur by path-options with anti-commuting spin-operator content. For leads in these subsectors, one generates a hybridization between the spin causing anti-commutation and the attached lead boundary-charge densities. Unless one fine-tunes hybridizations to vanish, e.g. by inserting magnetic fluxes in tunnel-loops, at low energies the associated boson-fields tend to decouple.

- After orthogonal rotations for lead-boson fields that employ the "correct" strong-coupling basis of the problem, for remaining non-hybridized spins we may perform Emery-Kivelson rotations. This allows to decouple one relative phase-field per spin, traded off against a hybridization with the boundary charge-density of the decoupled boson species. (In contrast, "charge spins" decouple center-of-mass bosons.)

- Consider a problem with M independent bosonic subsectors and m local fermion-groups forming spin-variables. At low energies, after Emery-Kivelson rotations that decouple center-of-mass or relative phases, this system reduces to coupling of $M-m$ possibly interacting boson species at their junction. In addition, for each of the m spins we have interactions with an independent boson-species that was decoupled.

- Even at a "Toulouse point" with quenched interactions, coupling of interacting bosons via impurities is a rich and complicated problem. Further progress then is possible by numerics, or in some special cases also by analytical calculation. The analytically tractable cases often correspond to well-known multi-channel Kondo models, but in starkly different context of quantum transport through coupled Majorana boxes.

Naturally we urge caution in application of the above strategies to more general cases. Systems of coupled Majorana boxes harbor rich and complex transport phenomena, as we have seen throughout this Chapter. Not all approximations are always equally justified, and which steps are best to take depends on the problem and physical question at hand.

Chapter 4

Topological Quantum Computation with Majorana fermions

In this Chapter we discuss implementations of measurement-based topological quantum computation (TQC) with Majorana fermions. As core part of the thesis this includes a rich variety of topics, from experiments- and application-driven design of topological qubits to large-scale quantum error-correcting codes (QECCs) in Majorana networks. In fact, a major motivation behind research on Majoranas is their potential for highly-protected (topological) quantum computations, both on the fundamental-qubit level and towards code-based quantum-information processing (QIP) and quantum error-correction (QEC).

The main ideas behind measurement-based quantum gates and computation are discussed in Sec. 4.1. From there we develop practical schemes for measurement-based protected QIP and TQC with Majoranas in Sec. 4.2 and Plugge *et al.* (2017); Karzig *et al.* (2017). After introducing the basal *Majorana box qubit*, including the access hardware for its operation, we then sketch concepts of QEC in Sec. 4.3. The design of Majorana network architectures towards the implementation of QECCs is subject of Sec. 4.4. Here we mention the general code networks of Karzig *et al.* (2017), and a particular promising QECC as realized in the so-called *Majorana surface code* (MSC) of Landau *et al.* (2016); Plugge *et al.* (2016a).
In Sec. 4.5 we give a short summary of our main results, and review some of the most relevant previous works and interesting recent theoretical efforts on measurement-based TQC. An outlook on the current experimental progress towards a realization of Majorana-based qubits and networks is given in the concluding Chapter 5 of this thesis

While we motivate basic principles of QEC and discuss some ingredients needed for its implementation, from there it is still a long shot to an understanding of full-fledged QECCs. Aside from our short introduction, we hence refer to the excellent books by Nielsen and Chuang (2010); Lidar and Brun (2013), lecture notes by Preskill (2018) and review articles of Gottesman (1997, 2010); Fowler *et al.* (2012); Terhal (2015) which we follow throughout.

4.1 Quantum gates and measurements

We here introduce the basic concepts of quantum gates, circuits and computation along with their possible measurement-based implementation. For an extensive overview, see e.g. the book by Nielsen and Chuang (2010) and lecture notes of Preskill (2018). During our discussion we freely switch between the action of quantum operators and circuits on states (Schrödinger picture) and on the corresponding qubit operators (Heisenberg picture), cf. Gottesman (1998), depending on which picture is convenient and offers more clarity.
In contrast to adiabatic quantum computation that describes the manipulation of quantum information stored in the Hilbert space of a system with Hamiltonian $H[\lambda(t)]$ by a gradual change of Hamiltonian parameters $\lambda(t)$ (cf. the braiding of Majoranas in Sec. 2.3), we here consider *digital* quantum computers. These rely on the circuit model for quantum computation, where a small *universal set of quantum gates* allows to manipulate input states of the computation efficiently and in an arbitrary manner. Clearly this approach is motivated from the functionality of classical computers, where similar circuit logic allows to construct arbitrary (classical) computations – using a fixed set of rules implemented on a corresponding "computationally-universal" hardware. For many quantum computing protocols and algorithms of interest, e.g., in quantum cryptography, we then do not need the ability to perform unitary simulations of a physical quantum system. Rather it is advantageous to consider a digitized, abstract quantum-circuit "programming language" that works hardware-independent on any complete "programmable" quantum computer, i.e., given it supplies a basal universal set of quantum gates.

4.1.1 A universal set of quantum gates

We now discuss the most commonly used quantum gates that re-appear below, up to and including a universal gate set. Note that such a set never represents a unique choice. Rather there is an infinite manifold of different minimal sets that allow to achieve quantum-computational universality; which ones are best to take or easiest to implement depends on the quantum-computing hardware under consideration.
We follow the notation of Nielsen and Chuang (2010), denoting all operators with "hats" and their eigenvalues as bare symbols. The single-qubit Pauli operators $\hat{X}$, $\hat{Y}$ and $\hat{Z}$ are

$$\hat{X} = \begin{pmatrix} 0 & 1 \\ 1 & 0 \end{pmatrix} \quad , \quad \hat{Y} = \begin{pmatrix} 0 & -i \\ i & 0 \end{pmatrix} \quad , \quad \hat{Z} = \begin{pmatrix} 1 & 0 \\ 0 & -1 \end{pmatrix} \quad . \tag{4.1}$$

We write the corresponding Pauli-eigenstates as $|0\rangle$ and $|1\rangle$ (with eigenvalues $Z = \pm 1$), $|+\rangle$ and $|-\rangle$ ($X = \pm 1$), $|y\rangle$ and $|\bar{y}\rangle$ ($Y = \pm 1$). Note the Pauli operator identity $i\hat{X}\hat{Z} = \hat{Y}$. Next the single-qubit Clifford gates, in addition to Pauli-flips $\hat{X}, \hat{Y}, \hat{Z}$ above, also include more general qubit rotations of Hadamard $\hat{H}$ and phase- or S-gates $\hat{S}_z$ and $\hat{S}_x$. We have

$$\hat{H} = \frac{1}{\sqrt{2}} \begin{pmatrix} 1 & 1 \\ 1 & -1 \end{pmatrix} \quad , \quad \hat{S}_z = e^{-i\pi \hat{Z}/4} \simeq \begin{pmatrix} 1 & 0 \\ 0 & i \end{pmatrix} \quad , \quad \hat{S}_x = e^{-i\pi \hat{X}/4} = \frac{1}{\sqrt{2}} \begin{pmatrix} 1 & -i \\ -i & 1 \end{pmatrix} \quad . \tag{4.2}$$

Remark the identities $\hat{H} = (\hat{X}+\hat{Z})/\sqrt{2} \simeq \hat{S}_z\hat{S}_x\hat{S}_z$, $\hat{S}_z^2 = \hat{Z}$ and $\hat{S}_x^2 = \hat{X}$. (Writing "$\simeq$" here means equivalence up to irrelevant global phases.) Therefore the two phase-gates $\hat{S}_z$ and $\hat{S}_x$ that describe $\pi/4$-rotations around Z- and X-Pauli axis of the qubit, respectively, span the full single-qubit Clifford group. The commonly-used Hadamard gate $\hat{H}$ corresponds to an exchange of x- and z-eigenstates (or $\hat{X}$ and $\hat{Z}$ Pauli operators) on the affected qubit, and can be implemented by consecutive $\pi/4$-rotations as noted above.
To achieve single-qubit universality, we additionally consider a single non-Clifford gate that goes beyond the simple rotations in Eq. (4.2). We write two more general phase gates

$$\hat{P}(\theta) = e^{-i\theta\hat{Z}} \quad , \quad \hat{T} = \begin{pmatrix} 1 & 0 \\ 0 & e^{i\pi/4} \end{pmatrix} \simeq \hat{P}(\theta = \pi/8) \quad . \tag{4.3}$$

Here $\hat{P}(\theta)$ is called (general) phase gate and describes arbitrary rotations with angle θ around the z-axis of the qubit. A popular choice for a non-Clifford phase gate is given by the phase-angle $\theta = \pi/8$ above, which often is referred to as $\pi/8$- or T-gate. We note that $\hat{T}^2 = \hat{S}_z$ and $\hat{T}^4 = \hat{Z}$, which is useful in practical implementations; in this sense the T-gate is the simplest extension of the single-qubit Clifford group to a universal gate set.
Last, for quantum-computational universality we need the ability to couple different qubits and to generate entanglement between them. The most common way to do this is by a two-qubit entangling gate, in this case the controlled-NOT or controlled-X gate

$$\hat{C}_x = \frac{1}{2}\left(1+\hat{Z}\right)_C \otimes 1_T + \frac{1}{2}\left(1-\hat{Z}\right)_C \otimes \hat{X}_T = \begin{pmatrix} 1_T & 0 \\ 0 & X_T \end{pmatrix}_C \quad . \tag{4.4}$$

The CNOT gate $\hat{C}_x$ acts between a control qubit C and a target qubit T. It applies a Pauli-X flip to the target qubit, $\hat{X}_T\,|0_T\rangle = |1_T\rangle$ (i.e., it implements the NOT-operation), if and only if the control qubit is in the $|1_C\rangle$-state (eigenvalue $Z_C = -1$). Hence the matrix representation in Eq. (4.4) acts on the 4-dimensional Hilbert space of the two qubits.

Subscripts for Pauli eigenstates (operators) indicate the qubit or subspace they belong to (act on). Pauli operator eigenvalues often are simply denoted as $X = \pm$ etc., and also referred to as parities of the corresponding Majorana pair (or subspace), cf. Sec. 2.2. A particular set of universal quantum gates that we consider below is given by the four basal gates $\{\hat{S}_x, \hat{S}_z, \hat{T}, \hat{C}_x\}$; we note that $\hat{S}_z = \hat{T}^2$ can be discarded, but having more than minimal operations – including also the Pauli flips of Eq. (4.1) – is very convenient in practice. For now, we continue with an understanding that the ability to perform such operations between nearby qubits, hosted e.g. in a 2D lattice, allows for universal quantum computations using the full system. Quantum gates between distant qubits then are performed by iteration of elementary two-qubit operations. Here we first aim to develop measurement-based quantum gate routines without considering an explicit hardware, and later show how to implement them for Majorana-based qubits in Sec. 4.2. We discuss further details on qubit networks and the necessary basal code-operations in context of QECCs in Sec. 4.4, where our few-qubit approaches indeed scale towards 2D network architectures.

4.1.2 Measurement-based quantum computation

In this section we introduce measurement-based quantum gates and circuits, cf. Nielsen and Chuang (2010); Preskill (2018). Anticipating the detailed discussion of their design in Majorana-based TQC or QECCs, Secs. 4.2 and 4.4, we here only give a short overview.
Rather than a pure measurement-only approach that operates on large and complicated input states supplying resources for the full computation (Briegel *et al.*, 2009), we here consider a mix of direct quantum-gate applications and measurement-based gates. To this end, we remark that in many (useful) qubit platforms one can naturally implement some minimal set of quantum gates, given e.g. by the Pauli gates $\{\hat{X}, \hat{Y}, \hat{Z}\}$, with high fidelity. In addition one usually has the ability to measure in (at least) two qubit bases $\hat{X}$ and $\hat{Z}$.

Rotations $\hat{S}_{x,z}$ (or $\hat{H}$) and the two-qubit CNOT $\hat{C}_x$ often are more difficult to implement than elementary Pauli-flips. Even more so this is true for non-Clifford gates (T-gate $\hat{T}$) that one needs to reach computational universality. We can then ask whether – given the ability to perform some specific two-qubit entangling measurements – it is possible to provide resource input states to the computation that allow to implement the above universal gates $\{\hat{S}_x, \hat{S}_z, \hat{T}, \hat{C}_x\}$ in a simpler fashion. The preparation of resource or *ancilla states*, hosted on additional *ancilla qubits* entering the quantum circuit, then is delegated to some special routines that happen "offline" (i.e., independent of "computational" qubits that host the quantum information we wish to process). This suggestive question constitutes the basic idea behind measurement-based quantum circuits and gate routines.

We start by discussing a measurement-based implementation of the CNOT $\hat{C}_x$ in Eq. (4.4). This gate acts between two qubits, flipping the state of target T (applying $\hat{x}_T$) if and only if control C is in state $|1_C\rangle$. In a measurement-based approach we need at least one additional ancilla qubit $A1$ by which the two logical qubits can interact, allowing us to perform measurements in the enlarged Hilbert space that do not collapse the logical states.
Running the circuit in Fig. 4.1, we note that after initial preparation of $|0_{A1}\rangle$ it contains two two-qubit entangling measurements between T and $A1$ as well as C and $A1$. These measurements act in $\hat{x}$- and $\hat{z}$-bases of the participating qubits, respectively, and are followed by a final control measurement on ancilla $A1$. Last one applies Pauli flips $\hat{z}_C$ or $\hat{x}_T$ as recovery operations, conditioned on intermediate measurement outcomes. The protocol is guaranteed to give a CNOT gate between control and target, as indicated in the inset of the figure. For illustration purposes one may consider the action of the CNOT-gate circuit in quantum-state representation, assuming measurement outcomes "+" in all steps. It then is easy to verify that the circuit in Fig. 4.1 indeed performs the CNOT in Eq. (4.4).

A second important quantum gate circuit, often referred to as phase-teleportation circuit, serves for implementation of an arbitrary phase gate $\hat{P}(\theta) = e^{-i\theta\hat{Z}}$ in Eq. (4.3). This circuit is also shown in Fig. 4.1, where initial preparation of an ancilla state

$$|A_\theta\rangle = P(\theta)\,|+_A\rangle = \frac{1}{\sqrt{2}}\left(e^{-i\theta}\,|0_A\rangle + e^{i\theta}\,|1_A\rangle\right) \tag{4.5}$$

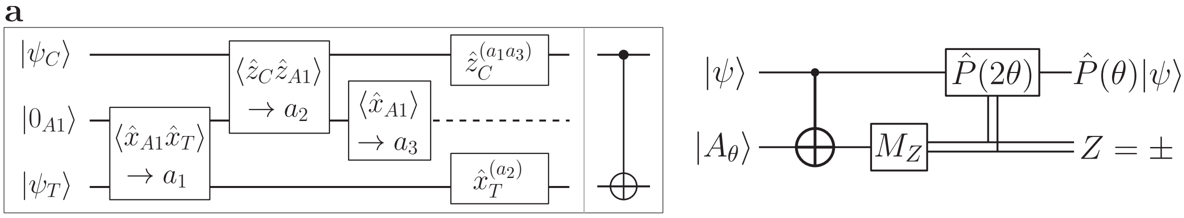

Figure 4.1: Measurement-based implementation of Clifford gates, cf. Preskill (2018). Left: CNOT gate. After initializing qubit $A1$ in $|0\rangle_{A1}$, one measures joint parities $\langle \hat{x}_{A1}\hat{x}_T\rangle$ and $\langle \hat{z}_C\hat{z}_{A1}\rangle$ with respective results $a_1 = \pm$ and $a_2 = \pm$. Finally, qubit $A1$ is read out, $\langle \hat{x}_{A1}\rangle = a_3 = \pm$, followed by controlled Pauli flips on qubits C and T. The flips are conditioned on intermediate outcomes $a_{1,2,3}$, where $\hat{z}_C$ and $\hat{x}_T$ is not applied (is applied) for $a_1a_3 = +(-)$ and $a_2 = +(-)$, respectively. With these recovery operations, the protocol gives a CNOT gate between qubits C and T, cf. the inset. Right: phase gate $\hat{P}(\theta)$. After preparing an ancilla state $|A_\theta\rangle$ in Eq. (4.5) on the bottom ancilla qubit, a CNOT-gate entangles both qubits. Subsequently, readout of the $\hat{Z}$-eigenvalue (measurement M_Z) collapses the state of the ancilla. With recovery $\hat{P}(2\theta)$ not applied (applied) for outcome $Z = +(-)$, the protocol implements a phase gate $\hat{P}(\theta) = e^{-i\theta\hat{Z}}$ on the top qubit hosting state $|\psi\rangle$. Figures from Plugge *et al.* (2017) (left) and Plugge *et al.* (2016a) (right).

on the ancilla qubit "A" becomes necessary. The circuit affects two qubits, one hosting the computational state $|\psi\rangle$ and another the ancilla state $|A_\theta\rangle$ (top and bottom in Fig. 4.1). After an entangling CNOT-gate beween computational (control) and ancilla (target) qubits, with outcome $Z = +$ of the ancilla measurement M_Z, we find (up to normalization)

$$\begin{aligned} \text{initial}: &\quad |\psi\rangle \otimes |A_\theta\rangle \;\simeq\; (\alpha\,|0\rangle + \beta\,|1\rangle) \otimes \left(e^{-i\theta}\,|0_A\rangle + e^{i\theta}\,|1_A\rangle\right) \\ \text{CNOT}: &\quad \alpha\,|0\rangle \left(e^{-i\theta}\,|0_A\rangle + e^{i\theta}\,|1_A\rangle\right) \;+\; \beta\,|1\rangle \left(e^{-i\theta}\,|1_A\rangle + e^{i\theta}\,|0_A\rangle\right) \\ Z_A = +: &\quad \left(\alpha e^{-i\theta}\,|0\rangle + \beta e^{i\theta}\,|1\rangle\right) \otimes |0_A\rangle \;=\; \left(\hat{P}(\theta)\,|\psi\rangle\right) \otimes |0_A\rangle \end{aligned} \tag{4.6}$$

A similar result is achieved for measurement outcome $Z_A = -$, but with opposite rotation $\hat{P}(-\theta)$ on the logical-qubit state $|\psi\rangle$. A recovery operation $\hat{P}(2\theta)$ can then restore the desired phase gate $\hat{P}(\theta)$, cf. Fig. 4.1. Double-lines here indicate classical information that conditions whether or not to apply a correction, similar as in the CNOT-gate circuit.

We now give important examples for phase-teleportation circuits that re-appear below. With phase $\theta = \frac{\pi}{4}$, we can implement the S-gate $\hat{S}_z = e^{-i\pi\hat{Z}/4}$ in Eq. (4.2). The recovery operation $\hat{P}(2\theta) = [\hat{P}(\theta)]^2 = \hat{S}_z^2 = \hat{Z}$ corresponds to a Pauli-flip $\hat{Z}$, which is simpler than the original gate. The resource state for S-gate application is given by $|y_A\rangle = \hat{S}_z\,|+_A\rangle$ in Eq. (4.5), which can be obtained by a Pauli-$\hat{Y}$ measurement. Further, with essentially the same routines one may also implement $\pi/4$-rotations around the $\hat{X}$-axis, i.e., $\hat{S}_x = e^{-i\pi\hat{X}/4}$ in Eq. (4.2). Last, for a measurement-based version of the $\pi/8$- or T-gate $\hat{T} \simeq e^{-i\pi\hat{Z}/8}$, the recovery operation in the phase-teleportation circuit becomes a S-gate with $\hat{S}_z = \hat{T}^2$. However this circuit requires a more complicated ancilla state given by $|A_{\pi/8}\rangle = \hat{T}\,|+_A\rangle$.

We find that by use of ancilla states in Eq. (4.5) and the phase-teleportation circuit in Fig. 4.1, one can reduce the need for phase gate applications to a correction in form of *twice* the original phase-value. This also highlights why the universal set of single-qubit phase gates $\{\hat{S}_x, \hat{S}_z, \hat{T}\}$ in measurement-based gate implementations is a particularly convenient choice: corrections in their corresponding phase-teleportation circuits reduce to simpler Pauli-flips or Clifford phase gates $\{\hat{X}, \hat{Z}, \hat{S}_z\}$, respectively.

To conclude, we require ancilla qubits and -states in order to execute gates in a measurement-based way. If we were to perform direct measurements on the logical qubits, we would collapse their encoded states and lose parts of the stored quantum information. The full computational Hilbert space will thus grow (significantly) larger than that of the logical, information-encoding qubits only, in particular for the QECCs in Secs. 4.3 and 4.4.
For the ancilla states to enter in a useful way, we need entangling measurements between ancillas and logical/computational qubits, which we tacitly assumed as given in Fig. 4.1. Otherwise, e.g., the ancillary phase-content of a state in Eq. (4.5) cannot be transferred into and used in the computational logic circuit. Overall, the performance of measurement-based quantum computations thus crucially depends on a supply of high-fidelity ancilla states, and on our ability to generate entangling two- or multi-qubit measurements.

Here we would like to caution that the ideas introduced above of course can not magically solve all challenges that appear in the implementation of universal quantum computation. However the fact that ancilla preparation can be done “offline”, independent of the logical computations we want to perform, is a powerful tool in QECCs. Much effort has been put in the development of so-called magic-state distillation schemes, e.g. to prepare states $|A_{\pi/8}\rangle$ as input for the T-gate, pioneered in seminal work by Bravyi and Kitaev (2005). Nevertheless, as extensively discussed in literature (Fowler *et al.*, 2012; Terhal, 2015), the preparation of ancillary input states becomes a serious bottleneck in code-based QIP.

4.2 Majorana box qubits and beyond

In this section we discuss elements of *Majorana box qubits* as example for partially protected, measurement-based topological quantum computation with Majorana fermions. The core of these devices are qubits encoded in mesoscopic four-Majorana islands (boxes), cf. the introduction in Sec. 2.2. With basic knowledge of quantum gates and circuits in Sec. 4.1 and a detailed discussion of basal Majorana systems, qubit-encoding and transport in Majorana boxes in Chapters 2 and 3, in principle our work Plugge *et al.* (2017) should be self-contained. Nevertheless, inspecting the Majorana box qubit (MBQ) in more detail allows us to introduce most ideas, concepts and setups used extensively in other works. In particular the more exhaustive publication Karzig *et al.* (2017) deals with more general Majorana qubit- and code-networks. Majorana boxes and their extensions also re-appear as fundamental units in Majorana-based QECCs, e.g. in the *Majorana surface code* of Landau *et al.* (2016); Plugge *et al.* (2016a), cf. Sec. 4.4.

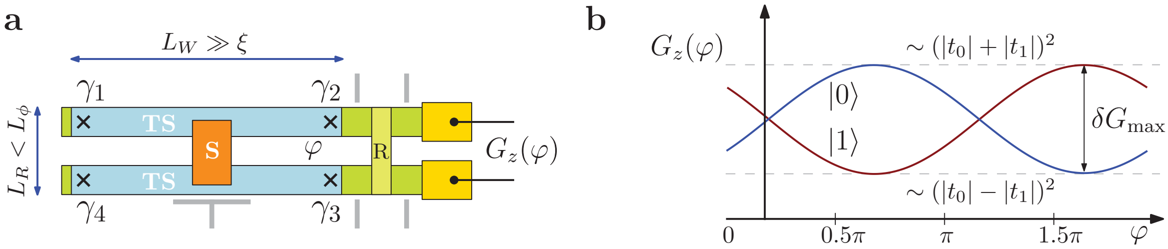

Figure 4.2: Majorana box qubit and readout based on conductance interferometry. (a) Two long TS wires (blue) are shunted by a superconducting bridge (S, orange) to form a floating island hosting four Majoranas γ_j (crosses). With electrostatic gates (gray) one can adjust the box charge state and tunnel-couplings through semiconductor segments (green). A semiconducting reference arm (R) forms an interference loop with the box, enclosing a magnetic flux φ. Readout of the MBQ Pauli operator $\hat{z} = i\gamma_2\gamma_3$ is possible via conductance interferometry between two normal leads (yellow). (b) The conductance $G_z(\varphi)$ is 2π-periodic in φ, with a relative π-shift for the two qubit states $|0\rangle$ and $|1\rangle$ with $z = +(-)$, respectively. Figure from Plugge *et al.* (2017).

4.2.1 Basic hardware and readout schemes

We start by introducing the basic central unit of the Majorana box qubit: a mesoscopic four-Majorana island with large charging energy, cf. Sec. 2.4, which hereafter is referred to as *Majorana box*. Such a device with some access hardware is shown in Fig. 4.2, where we recall the encoding of a single qubit into a Majorana box, cf. Sec. 2.2, as

$$\hat{z} = i\gamma_2\gamma_3 \;\simeq i\gamma_1\gamma_4 \;, \quad \hat{x} = i\gamma_1\gamma_2 \;\simeq i\gamma_3\gamma_4 \;, \quad \hat{y} = i\gamma_3\gamma_1 \;\simeq i\gamma_2\gamma_4 \;. \tag{4.7}$$

The representation of Pauli operators by complementary Majorana contents is possible due to the box parity constraint $\mathcal{P}_{\text{box}} = \gamma_1\gamma_2\gamma_3\gamma_4 = \pm$. Based on the design of a Majorana box in Fig. 4.2, the encoded qubit in Eq. (4.7) has highly unusual but very useful properties.

First, MBSs on the device are far-separated, meaning that Pauli operators defined from Majoranas are highly nonlocal and the box qubit has a protected ground-state degeneracy inherited from the MZMs (wires much longer than MBSs localization length, $L_W \gg \xi$). Second, different qubit operators are distributed in spatially distinct ways, with Pauli-$\hat{x}$ and -$\hat{z}$ operators encoded along horizontal and vertical dimension of the device in Fig. 4.2, respectively. Measurements and manipulations of such operators are then identified with spatially distinct access operations: topological protection of the MZMs enters our protocols and computations in precisely this way, also in the Majorana-based QECCs of Sec. 4.4.

Non-locality of access points in Majorana boxes and networks is a virtue (and challenge) which was already present in our analysis of charge transport, see Chapter 3. It prohibits “erroneous” processes of tunneling through MZMs which are not meant to be coupled at a given lead or quantum dot, but also implies that multi-junctions or loops necessary for

QIP applications need to be formed by hardware that allows for phase-coherent electron-transport over long distances. To this end, note that experiments finding highly degenerate MBSs employ TS wires that are several micrometers in length, cf. Albrecht *et al.* (2016). Coherent transport on such scales can be facilitated by using additional mesoscopic TS wires, or via low-density semiconductors (Gazibegovic *et al.*, 2017; Vaitiekėnas *et al.*, 2018) that also form the basis to implement TSs. This allows for reference arms with sufficient phase-coherence length L_ϕ in Fig. 4.2, while also keeping MZMs far-distant.

The first access operation we discuss is a measurement of the Pauli-$\hat{z}$ operator. To this end we consider two leads or QDs attached at the right side of the device in Fig. 4.2. Tunneling between the contact points in the co-tunneling regime, cf. Chapter 3, is described by

$$H_t = d_2^\dagger (t_0 + t_1 \hat{z}) d_3 + \text{h.c.} \;, \tag{4.8}$$

where $d_{2,3}$ are lead fermion operators tunnel-coupled to MZMs $\gamma_{2,3}$. Co-tunneling between the leads (QDs) here can proceed either via the box ($\sim t_1 \hat{z}$), picking up the two Majorana operators $\hat{z} = i\gamma_2\gamma_3$ in the process, or via the reference arm in Fig. 4.2 (amplitude $\sim t_0$). An interferometric conductance measurement between the lead contacts in Fig. 4.2 gives

$$G_z(\varphi) = \frac{e^2}{h} \nu_2 \nu_3 |t_z|^2 \quad , \qquad \text{with} \;\; t_z = t_0 + t_1 z \;. \tag{4.9}$$

Here $\nu_{2,3}$ is the density of states in the leads. More importantly, the conductance depends on the total inter-lead transfer amplitude t_z of the cotunneling Hamiltonian in Eq. (4.8), and therefore also on the MBQ state. The dependence of transport on the magnetic flux $\varphi = \arg(t_1/t_0)$, piercing a phase-coherent loop of the system, goes back to the celebrated gauge-invariance effect first unveiled by Aharonov and Bohm (1959). Electrons tunneling through the Majorana pair $\hat{z} = i\gamma_2\gamma_3$ now experience a relative π phase-shift depending on the fermion-parity state $z = \pm$, cf. Fu (2010). In Plugge *et al.* (2017) we show that the conductance measurement in Eq. (4.9) and Fig. 4.2 then indeed implements a projective measurement of the MBQ state, collapsing the MBQ towards states $|0\rangle$ or $|1\rangle$.

An alternative and likely less invasive readout mode is implemented by coupling Majorana boxes via quantum dots. These are also highly useful in the manipulation of MBQs, and described by the same effective Hamiltonian as in Eq. (4.8), but where $d_{2,3}$ are fermion operators for single-level QDs. This setup is shown in Fig. 4.3 for a device with two MBQs.

We first focus on single-qubit operation of the right MBQ "a" coupled by QDs 1, 2 and 3 in Fig. 4.3. A measurement of the Pauli operator $\hat{z}_a$ is implemented by tuning QDs 2 and 3 close to resonance and activating the reference arm connecting those two dots, while all other dots are far-detuned and cut off. The effective Hamiltonian of this setting reads

$$H_{\text{QDs},23} = \frac{\varepsilon}{2} \left(d_2^\dagger d_2 - d_3^\dagger d_3 \right) + d_2^\dagger (t_0 + t_1 \hat{z}_a) d_3 + \text{h.c.} \;, \tag{4.10}$$

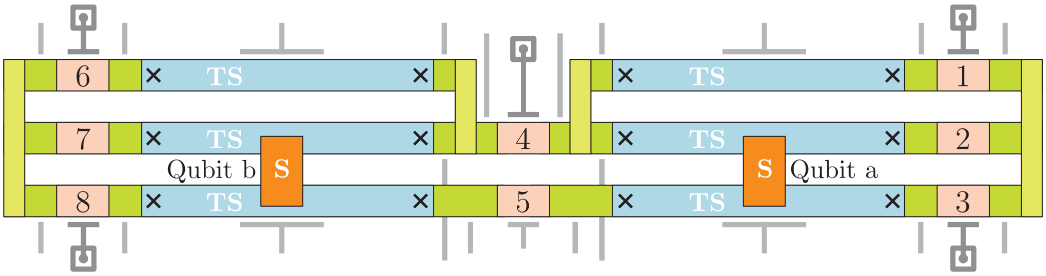

Figure 4.3: Device hosting two MBQs a and b, with QD-based readout and manipulation. Quantum dots (light red) are formed on semiconducting wire segments (green), where dot levels and tunnel couplings can be adjusted by gates (gray). Dark squares indicate e.g. charge sensors or resonator systems used for qubit readout via the QDs. Removing the central dots, a single MBQ a with three QDs 1, 2, 3 and interference links allows for readout of all Pauli operators and full single-qubit control, see text. Similar for qubit b. The full device with MBQs a and b, connected by dots 4 and 5, allows for readout of their joint parity via a MBQ product operator. Figure from Plugge *et al.* (2017)

where we add a dot-detuning energy ε to Eq. (4.8). Diagonalization yields the double-QD (DQD) hybridization energies $\omega_{z_a} = \sqrt{\varepsilon^2 + |t_{z_a}|^2}$ that depend on the MBQ state $z_a = \pm$. Detection of the MBQ state is possible by a measurement of the DQD spectrum $\sim \omega_{z_a}$ via photons in a microwave resonator that is capacitively coupled to one of the dots, cf. Fig. 4.3 and Plugge *et al.* (2017). Similarly one may detect spectral-derivative properties, e.g. differential charge or quantum-capacitance shifts on the dots, cf. Karzig *et al.* (2017).

By using different combinations of QDs one may now access all single-qubit operators of MBQ a (or b) in Fig. 4.3. To this end one simply identifies which Pauli operators are picked up in tunneling around a loop of the Majorana device coupled by QDs. In fact we learned in Chapter 3, e.g. for the loop qubit in Fig. 3.1, that a spin-charge coupling sets in only based on closed loops in the system; such hybridizations are exactly what is reflected in the dependence of spectral- or charge-shifts of the QDs on MBQ Pauli operators.
As discussed above, QDs 2 and 3 allow readout of the Pauli-$\hat{z}$ operator, cf. also Fig. 4.2. Similarly, QDs 1 and 2 allow readout of the horizontal Majorana-pair $\hat{x} = i\gamma_1\gamma_2$, if phase-coherent electron transfer on the long side of the MBQ is facilitated by another single TS wire with fixed fermion-parity (the top TS wire(s) in Fig. 4.3), cf. Sec. 2.4.2 and Fu (2010). Last, QDs 1 and 3 allow readout of the diagonal combination $\hat{y} = i\gamma_3\gamma_1$, also employing the single TS wire as coherent link while detuning or cutting off QD 2. Similar combinations with dots 6, 7 and 8 allow for measurements of all Pauli operators on qubit b in Fig. 4.3.

4.2.2 Joint-parity measurement and single-qubit rotations

The central QDs 4 and 5 facilitate a two-qubit entangling measurement between two MBQs a and b in Fig. 4.3. The total tunneling amplitude here reads $t_{z_a z_b} = t_a \hat{z}_a + t_b \hat{z}_b$, where the first (second) term refers to co-tunneling through qubit a (b). The corresponding Hamiltonian is as in Eq. (4.10) but with the new inter-dot tunneling, where the DQD hybridization frequency $\omega_{z_a z_b} = \sqrt{\varepsilon^2 + |t_{z_a z_b}|^2}$ now depends on the *joint-parity state* $\langle \hat{z}_a \hat{z}_b \rangle = \pm$.

Loop-coupling and measurement via QDs hence allows to implement highly protected and ancilla-free entangling measurements, in particular also of stabilizers in the context of QECCs, cf. Secs. 4.3 and 4.4. Any perturbation to the joint-parity measurements above has to be non-local, i.e., coupling the distant QDs 4 and 5 via an additional route other than co-tunneling through the MBQs or interference links. In contrast, decay and dephasing of the quantum dots (acting diagonally in QD-space) does not affect the above projection to a joint-parity eigenstate, but may reduce readout fidelity in measurement due to blurring of the QD spectra and charges, cf. Plugge *et al.* (2017); Karzig *et al.* (2017).

We now show how controlled charge-pumping allows to *apply* Pauli flips (Flensberg, 2011). Such operations are used in measurement-based gate circuits, cf. Sec. 4.1, in addition to the single-qubit and entangling two-qubit measurements above. Taking again QDs 2 and 3 in Fig. 4.3, and decoupling all interference links, a controlled charge pumping can be performed by sweeping the dot energy levels encoded in ε. With inter-dot transfer amplitude $t_{z_a} = t_1 \hat{z}_a$ (interference link $t_0 \to 0$) in Eq. (4.10), once a charge has been transferred between the dots, this operation necessarily applies the Pauli-flip $\hat{z}_a$ on MBQ a.

Similar but less protected, by tuning the magnetic flux piercing interferometric loops, i.e. $\varphi = \mathrm{Re}(t_1/t_0) = 0$, a geometric phase gate $\hat{P}(\theta) = e^{-i\theta\hat{z}_a}$ with $\theta = -\arctan\left[\mathrm{Im}(t_1/t_0)\right]$ can be performed. While this protocol includes some fine-tuning, it is protected on a Clifford-level in the sense that we only act on the Pauli-$\hat{z}$ axis of MBQ a. Errors due to non-ideal execution hence also only act on this qubit component, since effects on other Pauli operators or qubits would involve spatially distinct, quenched tunneling paths.
In QIP context, one can understand the phase gate as a QD-steered rotation in the coupled two-qubit Hilbert space of MBQ a and a double-dot charge qubit hosted in QDs 2 and 3. Here the fine-tuning $\varphi = 0$ of coupling between both qubits allows to avoid any dynamical phases, and steering the DQD along $|1_2 0_3\rangle \to |0_2 1_3\rangle$ (dot-occupations $|n_2 n_3\rangle$) by adjusting the dot detuning ε employs a coupled evolution of both qubits. After confirming the transferred charge on dot 3 (state $|0_2 1_3\rangle$) by measurement, the $z_a = \pm$ states of MBQ a have encircled a geometric phase-angle $\pm\theta$, undergoing the phase gate $\hat{P}(\theta)$.

Last, Majorana fermions only supply a Clifford algebra and corresponding Clifford-group rotations in a protected way. Any non-Clifford gate for Majoranas involves fine-tuning, and there has been a substantial effort to find optimal routines for such protocols, see e.g. Karzig *et al.* (2016); Knapp *et al.* (2016). Even though an arbitrary phase gate is not fully protected, it should at least be partially protected on the Clifford-level as discussed above. Rotations on other qubit axes $\hat{x}$ and $\hat{y}$ can be performed using the corresponding QDs. Similar protocols are available for encoded qubits in QECCs, cf. Plugge *et al.* (2016a).

a

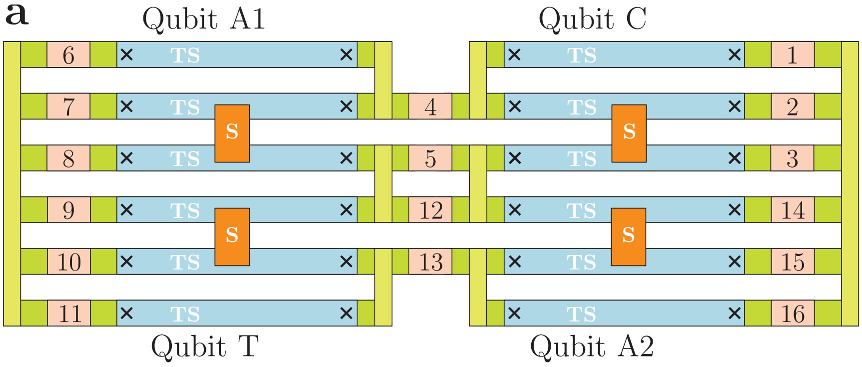

b

$1 \to 2$: $\hat{x}_C$	$6 \to 7$: $\hat{x}_{A1}$	$9 \to 10$: $\hat{z}_T$	$14 \to 15$: $\hat{z}_{A2}$
$2 \to 3$: $\hat{z}_C$	$7 \to 8$: $\hat{z}_{A1}$	$10 \to 11$: $\hat{x}_T$	$15 \to 16$: $\hat{x}_{A2}$
$1 \to 3$: $\hat{y}_C$	$6 \to 8$: $\hat{y}_{A1}$	$9 \to 11$: $\hat{y}_T$	$14 \to 16$: $\hat{y}_{A2}$
$4 \to 5$: $\hat{z}_C\hat{z}_{A1}$	$8 \to 9$: $\hat{x}_{A1}\hat{x}_T$	$12 \to 13$: $\hat{z}_T\hat{z}_{A2}$	$3 \to 14$: $\hat{x}_{A2}\hat{x}_C$

Figure 4.4: Four-qubit device. (a) Similar to Fig. 4.3, but with four MBQs allowing for measurement-based implementation of a two-qubit protected Clifford quantum computer. Two data qubits, denoted target (T) and control (C) for the CNOT-operation in Fig. 4.1, are coupled and manipulated via two ancillas $A1$ and $A2$. Using the ancillas one can also implement $\pi/4$-rotations around both qubit axes $\hat{x}$ and $\hat{z}$ on both data qubits C and T. (b) Protocols for the four-qubit device. With the indicated dot pairs, any single-qubit and the product operators of adjacent qubits can be addressed. Figure from Plugge *et al.* (2017).

4.2.3 A Clifford quantum computer: towards code networks

The two-qubit device in Fig. 4.3 does not yet allow implementation of the full two-qubit Clifford group in a protected way. To this end, a simple extension with two additional qubits in the 2×2 qubit array of Fig. 4.4 suffices to implement a two-qubit protected Clifford quantum computer. We here consider an operation of the device with two data qubits C and T, and two ancilla qubits $A1$ and $A2$. The measurement-based CNOT gate circuit in Fig. 4.1 can then directly be implemented, using pairs of QDs for measurements and application of Pauli-flips as incicated in Fig. 4.4(b). A flipped CNOT, with exchanged control and target qubits as compared to the figures, can also be implemented using ancilla $A2$ instead of $A1$. The $\hat{S}_{x,z}$-gates, employing $\pi/4$-rotations around $\hat{x}$- and z-axis of qubits C or T, can be generated from a simplified phase-teleportation circuit compared to that in Fig. 4.1. Instead of a CNOT-gate between ancilla- and data-qubit one can use a simple two-qubit entangling measurement that is available in our architecture (Plugge *et al.*, 2017).

4.2.4 Summary and discussion: Majorana box qubits

We conclude that the MBQ architecture allows for (topologically) protected Clifford-group operations and a semi-protected geometric phase gate. The latter could serve as a simple

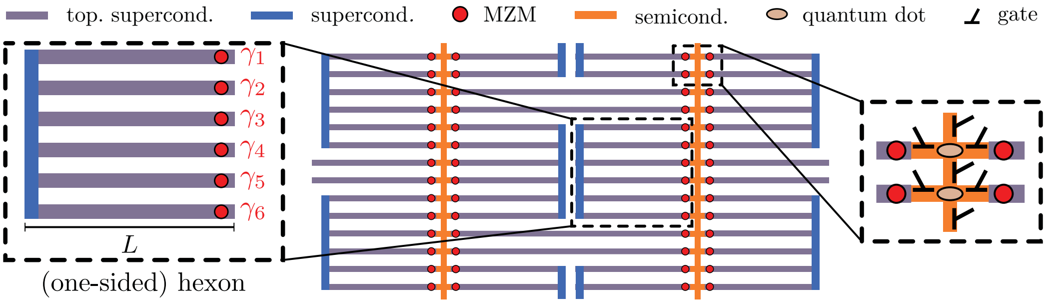

Figure 4.5: Hexons and their embedding into a network architecture. A one-sided hexon (left) is a comb-shaped six-Majorana island that can host one data- and one ancilla-qubit. Quantum dots in the underlying semiconductor network (right) are defined by local gates, and coupled to or decoupled from hexons as needed, cf. Fig. 4.3. Two-Majorana measurements on the hexon facilitate measurement-based braiding of Majoranas, and thus allow to locally generate the full single-qubit Clifford group. The network graph of this architecture is hexagonal, i.e., each hexon has one horizontal and two diagonal neighbors. Further details and discussion, see Karzig *et al.* (2017). Figure from Karzig *et al.* (2017).

approximate universal-gate implementation in small networks, or as a good starting point to ancilla distillation (Bravyi and Kitaev, 2005; Terhal, 2015) in the larger QEC-networks of Secs. 4.3 and 4.4. The simple single-qubit Pauli gates $\{\hat{x}, \hat{y}, \hat{z}\}$ can be directly implemented by controlled charge-pumping protocols. Instead the phase gates $\hat{S}_{x,z}$ with resulting Hadamard $\hat{H}$ and the two-qubit CNOT $\hat{C}_x$ are constructed from standard measurement-based gate routines (Nielsen and Chuang, 2010; Preskill, 2018), given our capability to perform high-fidelity two-qubit entangling measurements in Sec. 4.2.2.
We note that the MBQ architecture is scalable and can be extended to linear arrays as in Fig. 4.3, and by stacking rows into a 2D array similar to Fig. 4.4. As shown in Karzig *et al.* (2017), with Pauli-flips on all qubits, Pauli measurements on ancilla qubits and $\hat{z}-\hat{z}$ ($\hat{x}-\hat{x}$) entangling joint-parity readouts between horizontal (vertical) neighbors, the resulting 2D network is *Clifford-complete*. This means that the architecture allows for all Clifford-group operations between nearby qubits of the network, and thus has sufficient capabilities to run an arbitrary quantum error-correcting code (Terhal, 2015).

Several alternative Clifford-complete architectures are discussed in Karzig *et al.* (2017). There we also consider six-Majorana devices, see Fig. 4.5, that in addition to the data qubit directly host an ancilla qubit on the box. Such a strategy and encoding is slightly more complicated on the elemental-qubit level, but overall may be more versatile since it allows for all single-qubit Clifford operations to be performed locally, using only the on-box ancilla. Entangling measurements between different boxes then exclusively are used to perform two-qubit gates such as the CNOT, and there are no separate ancilla-boxes. In contrast, in the MBQ architecture of Fig. 4.4, half of the box qubits are used as ancillas.
Last, let us also mention the interesting parallel work of Vijay and Fu (2016b) on braiding of Majoranas in TS wire-networks as facilitated by the measurement-based approach.

4.3 Quantum error-correction

As last part of the thesis, we turn to the concept of quantum error-correction (QEC) and quantum error-correcting codes (QECCs). While of course we hope that Majorana-based qubits – the Majorana box qubit of Plugge *et al.* (2017) or tetron- and hexon-designs in Karzig *et al.* (2017) – will outperform other platforms already on the basic hardware level, for serious QIP tasks involving many qubits and quantum gates, error correction becomes inevitable. We here seek to design stabilizer measurement and code operation protocols that benefit from the inherent protection of qubits, basal protected Clifford-gate operations and high-fidelity entangling measurements in the Majorana architectures of Sec. 4.2.

For reviews on QEC and QECCs see Gottesman (2010); Fowler *et al.* (2012); Terhal (2015), books by Nielsen and Chuang (2010); Lidar and Brun (2013) and lectures by Preskill (2018). We here motivate basic requirements for a QEC hardware-platform and QECC operations, and introduce some of the fundamental ideas of QEC following Nielsen and Chuang (2010) and Preskill (2018). All further details are delegated to our works Landau *et al.* (2016) and Plugge *et al.* (2016a) on the *Majorana surface code* as one example QECC, and to Karzig *et al.* (2017) for more general Clifford-complete networks that can run arbitrary QECCs.

4.3.1 Quantum error-correcting codes: basics

Following Nielsen and Chuang (2010), we introduce two simple example (Q)ECCs that can be implemented with few qubits, e.g., in the systems of Sec. 4.2. Nevertheless they serve to illustrate general principles that re-appear in more complicated codes, cf. Sec. 4.4 below.

The three-qubit bit-flip code is a classical code that allows to correct a single bit-flip error $\hat{x}_{j=1,2,3}$ on any of its qubits 1, 2 or 3. It describes encoding of a single *logical qubit* ($k = 1$) into the larger Hilbert space of three qubits ($n = 3$), employing the *logical qubit states*

$$|0_L\rangle = |0_1 0_2 0_3\rangle \quad , \quad |1_L\rangle = |1_1 1_2 1_3\rangle \quad , \tag{4.11}$$

with associated *logical qubit operators* $\hat{Z}_L = \hat{z}_1\hat{z}_2\hat{z}_3$ and $\hat{X}_L = \hat{x}_1\hat{x}_2\hat{x}_3$. We here denote code- and logical-qubit operators with uppercase, and physical-qubit operators by lowercase symbols. This code can be implemented and checked by the two *stabilizers* ($n - k = 2$)

$$\hat{Z}_1 = \hat{z}_1\hat{z}_2 \quad , \quad \hat{Z}_2 = \hat{z}_2\hat{z}_3 \quad , \tag{4.12}$$

which for a measurement on the logical state $|\psi_L\rangle = \alpha\,|0_L\rangle + \beta\,|1_L\rangle$ always return the *trivial syndrome* $\langle Z_1, Z_2\rangle = \langle +, +\rangle$, indicating no error. A readout of the two stabilizers does not collapse the encoded state $|\psi\rangle$, and logical qubit operators $\hat{Z}_L$ and $\hat{X}_L$ commute with all elements of the *stabilizer group* $\mathcal{S} = \{\hat{Z}_j\}$. By this property, the logical qubit states and associated operators form the *code space* of the QECC that is *stabilized by* $\mathcal{S}$.
We now want to understand the error-correction capabilities of the code. With a bit-flip error $\hat{x}_{j=1,2,3}$ on any of the three physical qubits, we find the associated *error syndromes*

$$\hat{x}_1 : \ \langle -, +\rangle \quad , \quad \hat{x}_2 : \ \langle -, -\rangle \quad , \quad \hat{x}_3 : \ \langle +, -\rangle \quad . \tag{4.13}$$

Since the syndromes of all three errors are distinct, we can identify which bit-flip error has happened and subsequently correct it. Applying bit-flips $\hat{x}_{j=1,2,3}$ according to the above syndromes, thus giving $\hat{x}_j^2 = 1$ in total, we finally recover the correct logical state $|\psi_L\rangle$. The next more complicated error is a simultaneous bit-flip on two qubits. We find

$$\hat{x}_2\hat{x}_3 : \ \langle -,+\rangle \quad , \quad \hat{x}_3\hat{x}_1 : \ \langle -,-\rangle \quad , \quad \hat{x}_1\hat{x}_2 : \ \langle +,-\rangle \quad . \tag{4.14}$$

The error syndromes pairwise are the same as for single-qubit bit-flips $\hat{x}_j$ above, hence we are unable to distinguish the two cases. For any reasonable (correctable) source of errors, we assume that low-weight errors acting on fewer qubits are more likely than high-weight errors. The *weight* of an error (or operator) here corresponds to the number of physical qubits it affects. Hence our decoding for error $\hat{x}_2\hat{x}_3$ (weight 2) would read $\hat{x}_1$ (weight 1), and cyclic permutations. If we apply bit-flips $\hat{x}_{j=1,2,3}$ to fix the two-qubit errors in Eq. (4.14), we generate a *logical qubit error* $\hat{x}_1 \cdot (\hat{x}_2\hat{x}_3) \rightarrow \hat{X}_L$ (and cyclic permutations).

While we cannot be pleased with the existence of a logical error, this example allows us to deduce general rules for (quantum) error correction. Our approach in (Q)ECCs is to transform back the system, such that the error syndrome revealed by the code stabilizers S_j goes back to the code-space configuration with trivial syndrome, $\langle S_1, S_2, \cdots\rangle \rightarrow \langle +,+,\cdots\rangle$. The strategy fails if we deduce the wrong error from a given syndrome, where the actual error and our correction add up to a logical error. The two errors are said to differ by logical qubit operators, and have the same syndrome since the latter necessarily commute with all elements of the stabilizer group $\mathcal{S} = \{S_j\}$. In contrast, two operators that differ by elements of $\mathcal{S}$ are regarded as equivalent, since they have the same action on the code space. A QECC can correct errors up to weight t, with *code distance* $d = 2t + 1$ bound by the minimum weight of its encoded Pauli operators (for linear codes).

The three-qubit bit-flip code serves as instructive example, but it is a classical code that lacks the capability to correct arbitrary single-qubit errors. While the above representation of operators $\hat{X}_L$ and $\hat{Z}_L$ is appealing and elegant, it may mislead to overestimate the code distance as $d_{\text{wrong}} = 3$. The logical bit-flip $\hat{X}_L$ has weight 3, and we are able to correct one single-qubit bit-flip error in Eq. (4.13). The logical phase-flip, however, can also be represented as the weight-1 operator $\hat{Z}'_L = \hat{Z}_L\hat{Z}_2 = \hat{z}_1$, equivalent up to the stabilizer $\hat{Z}_2$ in Eq. (4.12). Phase-flip errors $\hat{z}_{1,2,3}$ commute with the stabilizers $\hat{Z}_{1,2}$, and therefore cannot be detected. A combined bit-phase-flip $\hat{y}_{j=1,2,3}$ is misidentified as bit-flip error, $\hat{y}_j = i\hat{x}_j\hat{z}_j$, where a phase-flip $\hat{z}_j$ goes unnoticed. For our purposes it is sufficient to consider single-qubit bit- and phase-flip errors $\hat{x}_j$ and $\hat{z}_j$, since the combined bit-phase-flip is their product and all higher-weight errors can be represented by products of single-qubit Pauli operators.

As seen above, and as used extensively below and in our publications, to describe a QECC it is sufficient to specify its stabilizers and logical qubit operators. The action of quantum gates and errors on the code and its operators then is captured by using the Heisenberg representation of QECCs and associated quantum gate circuits, cf. Gottesman (1998).

We now discuss the Steane or 7-qubit code (Nielsen and Chuang, 2010) as basic example of a functional QECC that can correct an arbitrary single-qubit error. The so-called *generators* of the Steane code, similar to those of the bit-flip code in Eq. (4.12), are given as

$$\begin{aligned} \hat{X}_1 &= \hat{x}_4\hat{x}_5\hat{x}_6\hat{x}_7 \ , \quad & \hat{X}_2 &= \hat{x}_2\hat{x}_3\hat{x}_6\hat{x}_7 \ , \quad & \hat{X}_3 &= \hat{x}_1\hat{x}_3\hat{x}_5\hat{x}_7 \ , \\ \hat{Z}_1 &= \hat{z}_4\hat{z}_5\hat{z}_6\hat{z}_7 \ , \quad & \hat{Z}_2 &= \hat{z}_2\hat{z}_3\hat{z}_6\hat{z}_7 \ , \quad & \hat{Z}_3 &= \hat{z}_1\hat{z}_3\hat{z}_5\hat{z}_7 \ . \end{aligned} \tag{4.15}$$

The stabilizer group $\mathcal{S} = \{\hat{X}_j, \hat{Z}_j\}$ is equivalently generated by any other six independent stabilizers that are obtained after multiplication of the ones in Eq. (4.15). Since we start with $n = 7$ qubits and employ $k = |\mathcal{S}| = 6$ constraints on their Hilbert space in form of the stabilizers above, the code space contains only a single qubit ($n - k = 1$). The associated logical qubit operators can be written as $\hat{X}_L = \prod_{j=1}^{7} \hat{x}_j$ and $\hat{Z}_L = \prod_{j=1}^{7} \hat{z}_j$, and evidently commute with all stabilizers. They are equivalently represented by $\hat{X}'_L = X_L X_1 = \hat{x}_1\hat{x}_2\hat{x}_3$ and $\hat{Z}'_L = Z_L Z_1 = \hat{z}_1\hat{z}_2\hat{z}_3$, making more apparent the actual (minimal) code distance $d = 3$. Note that here even the logical qubit states can directly be identified as $|0_L\rangle = \bigotimes_j |0_j\rangle$ and $|1_L\rangle = \bigotimes_j |1_j\rangle$, which for larger codes in Sec. 4.4 is not practical anymore.

The Steane code hence can correct one arbitrary single-qubit error. By checking (anti-) commutativity of all $3 \cdot 7 = 21$ Pauli operators $\hat{x}_j$, $\hat{y}_j$ and $\hat{z}_j$ with stabilizers $\hat{X}_j$ and $\hat{Z}_j$, one may identify their associated error syndromes $\langle X_1, X_2, X_3, Z_1, Z_2, Z_3\rangle = \langle \pm, \pm, \cdots\rangle$. Evidently, the $2^6 - 1 = 63$ available non-trivial syndromes (excluding $\langle +, \cdots\rangle \to$ no error) are significantly more than the minimum 21 needed to distinguish the single-qubit errors. In this sense, the Steane 7-qubit code is not optimal and comprises a significant overhead. The slightly more complicated but efficient 5-qubit code (Nielsen and Chuang, 2010) can also correct an arbitrary single-qubit error and is optimal, employing four stabilizers with $2^4 - 1 = 15$ non-trivial error syndromes to detect $3 \cdot 5 = 15$ independent Pauli errors.

4.3.2 Fault-tolerant quantum computation

After learning how to *store* quantum information in a well-protected way using QECCs in Sec. 4.3.1, we now discuss fault-tolerance of measurements, gates and computations.
Since we have encoded logical states in blocks of physical qubits, e.g. using the Steane 7-qubit code above, our measurements, quantum gates and other manipulations now have to work on the encoded logical qubit operators. Roughly speaking, if this was an easy task, also the environment could achieve it and trigger logical errors. Hence we should revisit and reconsider the design of logical qubit operations and quantum gates in Sec. 4.1 very carefully for the case of QECCs. However, luckily, there are systematic approaches to the design of fault-tolerant operations, cf. Nielsen and Chuang (2010) and Preskill (2018).

Following Nielsen and Chuang (2010), fault-tolerant quantum gates usually will consist of multiple operations, manipulations or measurements on individual or groups of physical qubits. They then should be designed such that at as many intermediate points as possible,

during and between execution of logical gates, we can run QEC by employing the stabilizers of our QECC. This prevents an accumulation of errors simply because the execution of gates or a computation takes long, and allows to spread operations over multiple *rounds of error-correction*, in each of which we measure the stabilizers. However, simply employing error-correction during or between the effective logical gates is not sufficient.
Another criterion for fault-tolerant operations is how they affect the *propagation of errors* in a quantum circuit. An action on single or groups of qubits that spreads an individual correctable error on one physical qubit into multiple errors that become non-correctable, i.e., they are turned into logical errors by subsequent QEC protocols, is not fault-tolerant. Hence our second requirement for good quantum gates and operations is that a single initial error is spread into at most one error per participating block of encoding qubits. Therefore the additional induced errors can still be coped with by QEC in each block.
Further, errors can not only spread, but also be introduced into the code by the physical operations implementing quantum gate circuits. These include physical-qubit gates, measurements or classical communication in Sec. 4.1 that are noisy. We hence also require that each faulty operation or component of a logical quantum gate circuit, beyond propagation of existing errors, generates at most one output error per block that encodes a logical qubit. Again, in this case the resulting errors should be correctable for each of the encoded qubits, i.e., by performing QEC on each qubit block after the gate circuit has finished.

Other operations that have to be performed fault-tolerantly are the measurement of stabilizers, preparation of ancillas and readout of logical qubit states. Again, measurements performed on the code should not introduce a substantial amount of errors to the system. Therefore any components used in these protocols have to be fault-tolerant with reasonably high fidelity. For stabilizer and qubit measurements to be conclusive, they are performed and kept track of over as many individual rounds of error correction as the code distance d prescribes. In a sense, QEC then does not only track the spatial, but also the time-evolved propagation of errors. This allows to discard *measurement errors*, e.g., based on majority-voting with outcomes over a few rounds, which otherwise introduce faulty corrections in the resulting QEC. More sophisticated algorithms are discussed in Terhal (2015).

The simplest and best-case example for fault-tolerant gate implementations are so-called *transversal gates*. To this end, some QECCs allow to perform a logical gate by parallel implementation of physical-qubit gates on each unit in a logical-qubit encoding block, i.e., gates can be applied in a bit-wise fashion. Recalling the Steane code, its simple logical operators indicate a potential for transversal gates. Here the Hadamard gate $\hat{H}$ can be constructed similar as the logical qubit operators $\hat{X}_L$, $\hat{Z}_L$, i.e., by taking individual-qubit Hadamards $\hat{H}_L = \prod_{j=1}^{7} \hat{H}_j$. With $\hat{H}^\dagger = \hat{H}$, cf. Sec. 4.1, it exchanges qubit operators as

$$\hat{H}_L \hat{X}_L \hat{H}_L = \prod_{j=1}^{7} \left(\hat{H}_j \hat{X}_j \hat{H}_j \right) = \prod_{j=1}^{7} \hat{Z}_j = \hat{Z}_L \ , \tag{4.16}$$

and $\hat{H}_L \hat{Z}_L \hat{H}_L = \hat{X}_L$. Since different qubits j in the encoding block do not communicate

with each other, error propagation between qubits is precluded. Further there is only one gate with error probability p_H applied to each qubit, and the probability for simultaneous errors on n qubits is suppressed as $p_n \sim (p_H)^n$. This exponential protection against errors in the number of affected qubits indicates a sufficient degree of fault-tolerance.
For the Steane code one can similarly implement Pauli-flips, S-gates and the two-qubit CNOT in a transversal fashion, but there is no fault-tolerant transversal non-Clifford gate. In fact, there exists no QECC with fault-tolerant implementation of a simultaneous fully transverse *and* universal gate set (Nielsen and Chuang, 2010; Terhal, 2015).

4.4 Quantum error-correction in Majorana networks

In this section, we summarize the central results of our works on quantum error correction and -correcting codes in Majorana-based qubits and network architectures. The Majorana box qubits of Plugge *et al.* (2017), cf. Sec. 4.2, and various designs of Karzig *et al.* (2017) allow to construct Clifford-complete code networks. They therefore can implement in principle arbitrary QECCs, including the Steane code introduced in Sec. 4.3.

The motivation behind the Majorana surface code (MSC) of Landau *et al.* (2016); Plugge *et al.* (2016a) is different. We here aim to implement the surface code approach to QEC in a maximally efficient way, using a network architecture with readout and manipulation routines tailored specifically to the needs of this QECC (Fowler *et al.*, 2012). To contrast the idea, the MSC networks discussed below may perform poorly when implementing a Steane code or any other QECC. But they should outperform the general-purpose Clifford-complete networks of Karzig *et al.* (2017) when it comes to running the surface code.
In taking this route, all the semiconductor-electronics hardware we want to utilize should be readily accessible to experiments. We recall that the Majorana box qubits in Sec. 4.2 rely on hardware and measurement- or manipulation-protocols that are commonly used in a non-topological qubit context. Since the MSC employs MBQs as fundamental units, the hardware for most of its operations can be directly adapted. Further discussion on experimental realizations of general code networks are given in the outlook to this thesis.

4.4.1 Majorana surface code: architecture and access hardware

We now introduce the basic hardware platform of the Majorana surface code architecture. Many QEC aspects such as the form of stabilizers and logical qubit operators follow rather directly from this construction, where the MSC employs a hybrid Hamiltonian- and digital stabilizer-measurement approach. We also discuss aspects of earlier work on this system, cf. Terhal *et al.* (2012), or for a different platform, cf. Xu and Fu (2010); Vijay *et al.* (2015).

The basal hardware architecture of the MSC is shown in Fig. 4.6. By connecting a square lattice of MBQs via tunnel-coupling t between MBSs on adjacent boxes, after projection to the charge ground state on each box as in Sec. 2.4.2 and Chapter 3, fourth-order tun-

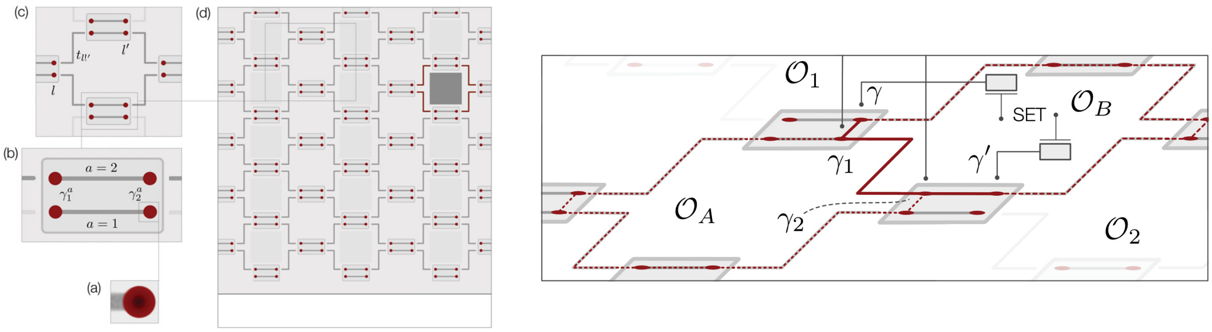

Figure 4.6: MSC architecture and access hardware. Left: MBSs (a, red dots) hosted on four-Majorana boxes (b) implement MBQs, cf. Sec. 4.2. By connecting boxes into loops via tunnel-couplings $t_{ll'}$, one enables ring-exchange processes involving the eight Majoranas surrounding each plaquette (c). Gray and white plaquettes in the ensuing checkerboard-lattice (d) implement stabilizers of the surface code. Right: Pairs of normal leads (indicated by vertical lines) are tunnel-coupled to adjacent MBSs $\gamma_{1,2}$ located on neighboring boxes. A two-terminal conductance measurement then provides information about plaquettes $\mathcal{O}_A$ and $\mathcal{O}_B$. Using SETs (quantum dots) connected to MBSs γ and γ', plaquettes $\mathcal{O}_{1,2}$ can be flipped and manipulated. Further discussion, see text. Figures from Landau *et al.* (2016).

neling processes define the ring-exchange amplitudes $c_n \sim t^4/E_c^3$. For plaquette number n, the plaquette operator $\mathcal{O}_n = \prod_{j=1}^{8} \gamma_j^{(n)}$ picked up during loop-tunneling is defined by the surrounding eight MBSs $\gamma_j^{(n)}$. Equivalently these are represented by four Pauli operators $\hat{x}_j$ or $\hat{z}_j$, one for each of the participating MBQs, cf. Secs. 2.2 and 4.2. In our convention, $\hat{z}_j$ ($\hat{x}_j$) is defined from vertical (horizontal) pairs of MBSs on MBQs in every even row, and vice versa for odd rows. One then obtains a checkerboard-pattern in Fig. 4.6, where every other plaquette is similar while neighboring plaquettes implement distinct types of stabilizers $\hat{Z}_a = \prod_{j=1}^{4} \hat{z}_j^{(a)}$ and $\hat{X}_b = \prod_{j=1}^{4} \hat{x}_j^{(b)}$ in the ensuing surface code below.

The low-energy Hamiltonian of the MSC then reads (Kitaev, 2006; Terhal *et al.*, 2012)

$$H_{\text{code}} = -\sum_n \text{Re}(c_n)\mathcal{O}_n = -\sum_a J_a \hat{Z}_a - \sum_b J_b \hat{X}_b \quad , \tag{4.17}$$

which as ground state admits the code space $\langle Z_a, X_b\rangle = \langle +, +\rangle$ with stabilizers $\{\hat{Z}_a, \hat{X}_b\}$, assuming $J_{a,b} > 0$. Since excitations in form of flipped stabilizers can propagate freely once created, unfortunately, H_{code} does not implement a self-correcting quantum memory (Brown *et al.*, 2016). We hence have to employ active measurements to fight the generation and propagation of errors, i.e., to implement QEC. Nevertheless, with stabilizers that are directly encoded in a Hamiltonian, stabilizer measurements in the MSC can be implemented by a single-shot readout operation (Vijay *et al.*, 2015). This is to be contrasted against the complicated entangling-gate quantum circuits using ancilla qubits, necessary to employ stabilizers, e.g., in superconducting qubit architectures (Fowler *et al.*, 2012).

We have discussed practical approaches to joint-parity and stabilizer readout for MBQs in Sec. 4.2. Taking for example a conductance measurement between leads contacting neighboring MBSs γ_1 and γ_2 in Fig. 4.6, due to interfering tunneling paths, one is able to determine the state of neighboring plaquettes $\mathcal{O}_1$ and $\mathcal{O}_2$ (Landau *et al.*, 2016). These correspond to $\hat{Z}$- and $\hat{X}$-type stabilizers of the MSC, respectively. A MSC network with N MBQs thus is fully stabilized by readout at $\sim N$ suitably chosen pairs of leads.

Controlled Majorana-flips facilitate the application of physical and logical Pauli operators in the MSC, and can be employed by controlled charge-pumping via quantum dots, cf. Sec. 4.2 and Flensberg (2011). In Fig. 4.6, a variant of QDs is denoted “SET”, where each individual Majorana can selectively be coupled to its own access hardware. The action of a charge-pumping protocol is most transparently analyzed in the Majorana representation. For example, the setup in Fig. 4.6 allows to insert one charge at MBS γ under extraction of another charge at different MBS γ'. Inter-code tunnelings between adjacent MBSs then restore equilibrium charges on all MBQs. Since these commute with the plaquettes they generate, the full operator action on the code is described by the Majorana pair (γ, γ'). The latter pairs are uniquely identified by the contact points we choose, and controlled Majorana-flips implement topologically protected operations on the code, cf. Sec. 4.2.

A charge pumping now flips zero, two or four stabilizers if the pair (γ, γ') shares two, one or no plaquettes. The case of zero flips and two shared plaquettes was employed for stabilizer readout with contacts (γ_1, γ_2). With (γ, γ') in Fig. 4.6 we show the case of a single shared plaquette $\mathcal{O}_B$, where two stabilizers of same type, hosted on plaquettes $\mathcal{O}_{1,2}$, are flipped. In surface code language, a Majorana pair (γ, γ') can thus equivalently be represented as the product of four Pauli operators $\hat{X}_a^{(\gamma/\gamma')}$ and $\hat{Z}_b^{(\gamma/\gamma')}$ that are conjugate to the stabilizers $\hat{Z}_a^{(\gamma/\gamma')}$ and $\hat{X}_b^{(\gamma/\gamma')}$ on plaquettes that are flipped by γ/γ', respectively. We note

$$i\gamma\gamma' \;\simeq\; \hat{X}_a^{(\gamma)}\hat{Z}_b^{(\gamma)} \;\cdot\; \hat{X}_a^{(\gamma')}\hat{Z}_b^{(\gamma')} \quad , \tag{4.18}$$

where in contrast to stabilizers these objects are often referred to as (Pauli) *string operators*. As with any QECC operator, their representation is unique up to stabilizers $\{\hat{Z}_a, \hat{X}_b\}$. For MSC networks that encode multiple qubits and hence are not fully stabilized, see below, path-information about the intermediate intra-code tunneling events becomes important.

4.4.2 Measurements and basal gate operations

As last part, we discuss how measurements and quantum gate operations are performed in the MSC. This involves adaptation or clever extension of methods used in conventional surface codes (Fowler *et al.*, 2012; Terhal, 2015), and for a MSC based on different hardware in Vijay *et al.* (2015). We hence only give a short overview of our main contributions in Plugge *et al.* (2016a), for the MSC architecture in Sec. 4.4.1 and Landau *et al.* (2016).

We start with a short general introduction to surface code operation (Fowler *et al.*, 2012). First, unfortunately, surface codes do not afford transversal applications of quantum gates. We discussed the appealing simplicity of such gates in Sec. 4.3. As trade-off, surface codes have rather high error-thresholds for both measurement and gate-induced errors, and are based on particularly simple four-qubit stabilizers in Eq. (4.17). Many advanced codes have lower error-thresholds and/or comprise high-weight stabilizers that in practice are more difficult to access. For a discussion of more general Majorana fermion codes that could be implemented in the Clifford-complete Majorana networks of Karzig *et al.* (2017), see e.g. Vijay and Fu (2017); Litinski and von Oppen (2018). In any case, the MSC should be seen as an example QECC that can efficiently be implemented with Majoranas.

From our introduction of small-scale Majorana-TQC networks in Sec. 4.2, we know that single-qubit Clifford gates and two-qubit entangling measurements can be performed in a (topologically) protected fashion. Similarly, the implementation of a non-Clifford phase gate is at least partially protected, i.e., its constituent operations for the preparation of ancilla states are protected on the Clifford level. As minimum ask, all good, high-fidelity operations in Majorana-based QECCs should therefore afford a (topological) protection on the Clifford level, i.e., to the degree that Majoranas and measurement-based TQC permit. This basic rule is overlooked in surprisingly many works which do not utilize the underlying topological Majorana hardware to its fullest.

A few aspects of QEC in the MSC are shown in Fig. 4.7. We here focus on basic functionality, where larger code distances and fault-tolerance can be achieved as outlined in Plugge *et al.* (2016a). While individual patches of surface code can also encode qubits, for practical applications, we consider a virtually infinite system in which logical qubits are embedded. This is possible by omitting select stabilizers from the otherwise complete cyclic measurement of syndromes in each round of QEC (Fowler *et al.*, 2012). In addition, we cut the tunnel-couplings which give rise to their plaquette energy in Eq. (4.17). All surface code operations in the MSC can then be implemented by weight-4 stabilizers, weight-2 string operator measurements and controlled charge-pumping between QDs.

A double-cut qubit is based on two stabilizers $\hat{Z}_{a1}$ and $\hat{Z}_{a2}$ that redundantly encode a quantum state, e.g., in their even-parity subspace $\langle \hat{Z}_{a1}\hat{Z}_{a2}\rangle = +$, as

$$|\Psi_a\rangle = \alpha\,|0_a\rangle + \beta\,|1_a\rangle \equiv \alpha\,|0_{a1}0_{a2}\rangle + \beta\,|1_{a1}1_{a2}\rangle \ . \tag{4.19}$$

The Pauli operators of double-cut qubit a are given as $\hat{Z}_a = \hat{Z}_{a1} \simeq \hat{Z}_{a2}$ and $\hat{X}_a = \hat{X}_{a1}\hat{X}_{a2}$, and contain only Pauli-$\hat{z}$ and -$\hat{x}$ operators of MBQs, respectively. We usually note only one stabilizer and the connecting string operator. In Fig. 4.7, the first stabilizer is highlighted and the emanating string attached, while the second stabilizer – if at all – is shown with a dashed outline. The same principles apply to the X-type double-cut qubit b in Fig. 4.7.

Measurement and initialization now are possible by measuring the stabilizer $\hat{Z}_a$, or by bitwise readout of the string $\hat{X}_a$ that contains the Pauli-$\hat{x}$ operators of all MBQs it crosses.

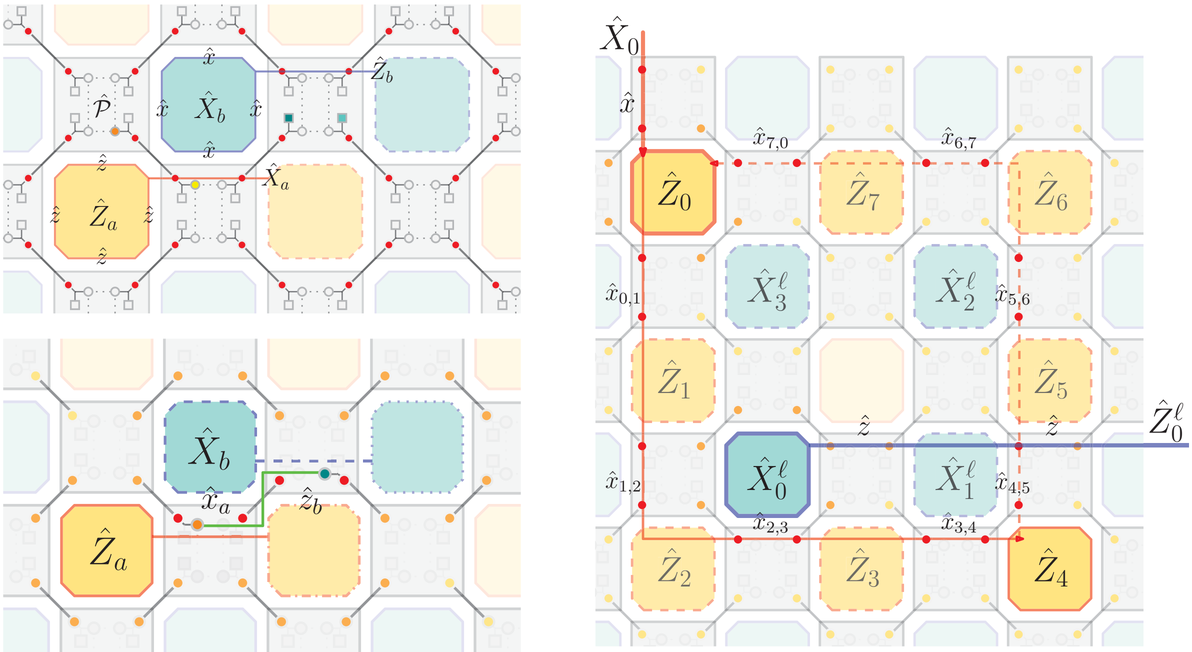

Figure 4.7: Elements of QEC in the MSC. Top left: MSC hardware, cf. Fig. 4.6. MBSs on adjacent MBQs are tunnel-coupled to form a checkerboard of Z- and X-type stabilizers (in yellow and blue, respectively). Boxes and circles on MBQs are QDs and lead-contacts, with interference links (dashed) for MBQ readout. A pair of $Z(X)$-type stabilizers, one highlighted and other with dashed outline, is omitted from measurement. It encodes a $Z(X)$-type double-cut qubit $a(b)$, with Pauli operators $(\hat{Z}_a, \hat{X}_a)$ (resp. $(\hat{X}_b, \hat{Z}_b)$). Bottom left: a two-box interference link (green line) connects the orange and blue lead contacts (filled circles), allowing readout of the string operator $\hat{x}_a\hat{z}_b$. Right: Braiding of qubits. Initially, qubits A and B are hosted in $(\hat{Z}_A, X_A) = (\hat{Z}_0, X_0)$ and $(\hat{X}_B, Z_B) = (\hat{X}^\ell_0, Z^\ell_0)$. By a sequence of moves, qubit A encircles the X-type plaquette hosting qubit B. The string of qubit A then is transformed as $\hat{X}_A \to \hat{X}'_A \simeq \hat{X}_A \cdot \hat{X}_B$, where $\hat{X}^\ell_0$ is the only non-measured stabilizer of those tiling the loop $\hat{X}_\ell = \prod_j \hat{X}^\ell_j$. Figures adapted from Plugge *et al.* (2016a).

Movement of qubits between plaquettes of same kind is possible by measurement of MBQ Pauli operators, followed by a readout of stabilizers. To this end, consider two stabilizers $\hat{Z}_{a1}$ and $\hat{Z}_{a2}$ connected by a string operator $\hat{X}_a = \hat{X}_{a1}\hat{X}_{a2}$ in Fig. 4.7 as independent. With qubit $a1$ hosting an encoded state, both qubits can be entangled by a readout of the intermediate MBQ operator $\hat{x}_{a1,a2} = \hat{X}_{a1}\hat{X}_{a2}$. Activating (omitting) the stabilizer readout of $\hat{Z}_{a1}$ ($\hat{Z}_{a2}$) in the next code cycle then shifts the encoded logical state onto qubit $a2$.

Next, consider a measurement of the weight-2 string operator $\hat{x}_a\hat{z}_b$ in Fig. 4.7. Equivalently, this two-MBQ operator comprises the product of string operators $\hat{X}_a\hat{Z}_b$ on the two double-cut qubits a and b. Its measurement requires an additional interference link beyond single-MBQ measurements, and allows to entangle the Z- and X-type qubits. We

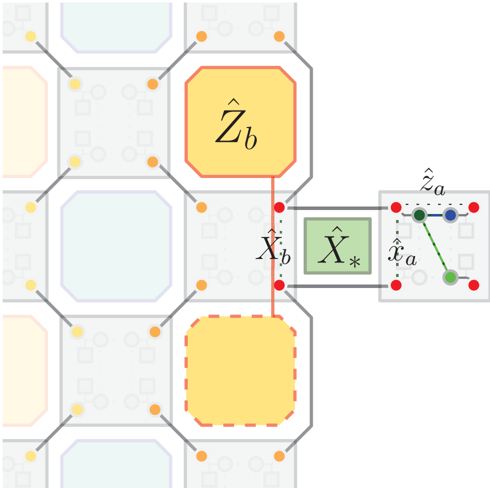

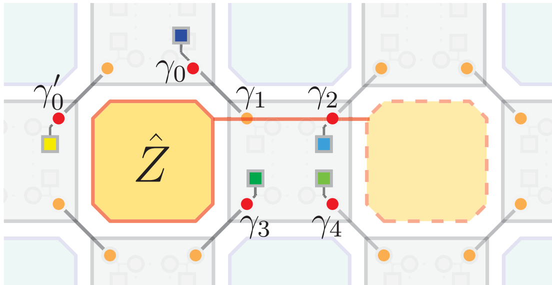

Figure 4.8: Ancilla preparation for phase gates in the MSC. Left: An auxiliary MBQ a is tunnel-coupled to a MBQ belonging to the MSC, but located at the boundary. Arbitrary ancilla states $|\psi_a\rangle$ may be prepared on the decoupled MBQ a, using the methods of Sec. 4.2. Subsequently, by employing a joint-parity readout via operator $\hat{X}_* = \hat{x}_a \hat{X}_b$, the ancilla MBQ and a double-cut qubit $(\hat{Z}_b, \hat{X}_b)$ of the code can be entangled. The ancilla state $|\psi_a\rangle$ can thereby be injected into the code. Right: Controlled charge-pumping between quantum dots, e.g. connected to MBSs γ_0 (dark blue) and γ_2 (light blue), allows to implement semi-protected qubit rotations on a double-cut qubit $(\hat{Z}, \hat{X})$. Figures from Plugge *et al.* (2016a).

hence are able to move logical states *between* distinct-type qubits. Since their definitions of Pauli-$\hat{Z}$ and -$\hat{X}$ operators are inverted, such inter-species moves implement a Hadamard gate $\hat{H}$ on the logical encoded state (Fowler *et al.*, 2012; Vijay *et al.*, 2015).

Last, Fig. 4.7 shows how to braid different-type qubits. Here a sequence of single-step qubit moves allows a Z-type qubit $(\hat{Z}_A, \hat{X}_A)$ to encircle the plaquette that encodes a different X-type qubit $(\hat{X}_B, \hat{Z}_B)$. Since we perform a closed loop movement, the string operators of both qubits necessarily have crossed at some point, and non-trivial transformations can take place. Usually, additional loops in string operators $\hat{X}_A \to \hat{X}'_A \simeq \hat{X}_A \hat{X}_\ell$ can be removed by employing the syndromes of stabilizers tiling the loop. For the situation in Fig. 4.7, we find $\hat{X}_\ell = \prod_j \hat{X}_j^\ell = \hat{X}_B \cdot (\hat{X}_1^\ell \hat{X}_2^\ell \hat{X}_3^\ell) \simeq \hat{X}_B$, where all stabilizers but $\hat{X}_0^\ell = \hat{X}_B$ are in known eigenstates. Hence the string of qubit A is multiplied by the stabilizer of qubit B, and after changing perspective, the opposite is also true. The braid transformation reads

$$(\hat{Z}_A, \hat{X}_A) \;\to\; (\hat{Z}'_A, \hat{X}'_A) = (\hat{Z}_A, \hat{X}_A \hat{X}_B) \quad , \quad (\hat{X}_B, \hat{Z}_B) \;\to\; (\hat{X}'_B, \hat{Z}'_B) = (\hat{X}_B, \hat{Z}_A \hat{Z}_B) \quad , \tag{4.20}$$

which is nothing but the Heisenberg representation of a CNOT gate with control qubit A and target qubit B, cf. Sec. 4.1. Similarly, by using ancilla qubits as intermediaries, CNOT gates between same-type qubits become possible (Fowler *et al.*, 2012).

Finally, the setups in Fig. 4.8 show how ancilla states can be injected into or directly generated in the MSC. First, by coupling individual or small networks of auxiliary MBQs to the code boundaries, ancilla states and computations as in Sec. 4.2 can be supplied to the MSC. Such setups also establish how the MSC platform can interact with other types of Majorana architectures or qubits. Alternatively, charge-pumping protocols that employ superpositions of non-equivalent tunneling paths $\sim (t_x\hat{X} + t_y\hat{Y})$ in Eq. (4.18) allow to implement qubit rotations directly on double-cut qubits of the MSC. They are similar to those discussed for MBQs, cf. Sec. 4.2, and semi-protected on the Clifford-level. For details, see Plugge *et al.* (2016a). In order to obtain arbitrarily good, high-fidelity ancilla states towards phase gate implementation in extended and fault-tolerant quantum computations, the use of ancilla distillation becomes unavoidable. Given the availability of high-fidelity Clifford group operations and good approximate ancilla states in the MSC, standard distillation schemes (Bravyi and Kitaev, 2005; Fowler *et al.*, 2012; Terhal, 2015) should find a reasonable starting point with the routines discussed above.

4.5 Summary: quantum computing with Majoranas

We now shortly summarize the final chapter of this thesis. After a basic introduction to measurement-based quantum gates and gate circuits in Sec. 4.1, we discussed their possible realization in the Majorana-based topological qubits and small-scale networks of Sec. 4.2. Measurement-based TQC here comes with an inherent high level of protection due to the non-locality of MBQs that are encoded in the mesoscopic Majorana islands of Sec. 2.2. These devices do not only function as hosts for highly degenerate qubit ground states, but also facilitate topologically protected access operations due to the select and non-local addressing of distinct Majoranas in the network by charge transport, cf. Chapter 3.
In the context of QIP and QEC, this translates to the select addressing of individual or groups of Pauli operators in Sec. 4.2, and of stabilizers in the QECCs of Secs. 4.3 and 4.4. Using two-terminal conductance measurements, or by coupling the topological hardware to auxiliary charge qubits in form of quantum dots, a direct single-shot readout of MBQ Pauli operators, joint-parities or stabilizers in the MSC becomes possible. Majorana-based qubits and code networks hence show a potential for high-fidelity stabilizer measurements and Clifford group operations, which form the backbone of any QECC, cf. Terhal (2015). In combination with protocols for the semi-protected preparation of approximate ancilla states, they may then incite hope for a reduced overhead of QEC in Majorana-based QIP.

A wealth of related research has investigated TQC in different anyon systems or using other approaches to QEC, and for a detailed discussion we refer to our published works.
Starting from ideas of Freedman *et al.* (2003); Kitaev (2003), measurement-based TQC and interferometric readout for general anyons was studied by Bonderson *et al.* (2007, 2008a,b, 2009). These works are abstract, and mostly focus on the mathematical and quantum-information theoretical foundations of anyon-based TQC, reviewed in Nayak *et al.* (2008).

For Majorana fermions (or general anyons), the parity-readout discussed in Sec. 4.2.1 can also be achieved by flux- instead of charge-tunneling, inspired by gauge invariance effects of Aharonov and Casher (1984). A setup was suggested by Hassler *et al.* (2010), where the topological charge (parity) of an encircled group of anyons (MFs) in an interferometric setting imprints a phase-shift on the flux that is tunneling around it. The converse effect of Aharonov and Bohm (1959), entering in the interferometric conductance (Fu, 2010) and quantum dot spectral readouts of MBQs, experimentally is more robust. A phase-gate implementation, similar to our charge-pumping protocols, is also possible by a tunneling of flux vortices, cf. Clarke *et al.* (2016); Dua *et al.* (2018).

Majorana devices interacting with charge, spin or superconducting qubits are discussed in Flensberg (2011), Leijnse and Flensberg (2011, 2012a) and Bonderson and Lutchyn (2011); Jiang *et al.* (2011). The top-transmon of Hassler *et al.* (2011) is a Majorana qubit coupled with a superconducting transmon, and an extension of this hybrid architecture to networks is investigated in Hyart *et al.* (2013). Here for readout purposes the charge states on an otherwise grounded Majorana island are energetically split by reducing the Josephson-coupling with a bulk superconductor, and the Majorana sector is read out by a parity-to-charge conversion. Further, large-scale Majorana and spin-qubit hybrid systems are discussed in detail by Hoffman *et al.* (2016).

MBQ networks and the Majorana surface code are adaptations of our hardware platform for quantum error correction, and up to date with current experimental challenges and opportunities in the implementation of MBSs. Here the strongly related MSC platforms of Terhal *et al.* (2012); Vijay *et al.* (2015); Vijay and Fu (2016a) are of particular relevance. Motivated by our work, Li (2016) showed that MSCs can have substantially higher error thresholds compared to conventional-qubit code realizations. Further, Litinski *et al.* (2017) consider a color code that affords transversal Clifford gates, and Bravyi *et al.* (2010); Vijay and Fu (2017); Hastings (2017); Litinski and von Oppen (2018) discuss Majorana fermion codes beyond standard (bosonic) QECCs. While box charging energies for locally-encoded Majorana qubits are useful to suppress quasi-particle poisoning (Karzig *et al.*, 2017), such devices utilize only the emergent bosonic qubit degrees of freedom on a box.

Last, our proposals are in-line with the device development for ad-hoc simpler Majorana-fusion experiments (Aasen *et al.*, 2016), which operate on tunable-interaction setups similar to those of Sau *et al.* (2011); van Heck *et al.* (2012). MBQs were also adapted to other material platforms (Manousakis *et al.*, 2017) and to parafermions (Snizhko *et al.*, 2018).

Chapter 5

Conlusions and outlook

In the last Chapter of this thesis, we conclude with a short summary of our contributions to the fields of quantum transport and topological quantum computation in Majorana boxes. Afterwards we give an outlook on interesting recent experimental progress towards the realization of Majorana qubits and network devices, and possible future directions of research.

In Chapter 2, we introduced basic Majorana systems that afford the topologically protected storage and manipulation of quantum information. Corrections to toy models and ideal braiding statistics were investigated for interacting Kitaev chains in Sekania *et al.* (2017). Next, the inclusion of charging energy effects on *mesoscopic Majorana islands* allows charge transport to access the non-local character of Majorana bound states in topological superconductors. In Plugge *et al.* (2015), we discussed how correlations and entanglement spread between distant quantum dots that are coupled by such Majorana boxes. Phase-coherent transport in the coupled Majorana box devices of Chapter 3 facilitates the formation of a *topological Kondo effect* in simply-coupled islands, and we investigated related quantum transport phenomena in multi-junction setups of Plugge *et al.* (2016b); Gau *et al.* (2018). In the *Majorana box qubit* of Plugge *et al.* (2017) and *loop qubit* of Karzig *et al.* (2017), see Chapter 4, simple conductance or spectroscopic measurements can characterize the performance of the ensuing Majorana-based topological qubits. Extension of these devices to small networks allows for measurement-based protected quantum computations with Majoranas, including *Clifford-complete code networks* that can run arbitrary quantum error-correcting codes. One particular promising example for Majorana-based quantum error correction is the *Majorana surface code* of Landau *et al.* (2016); Plugge *et al.* (2016a).

Experiments on mesoscopic TS wires (Albrecht *et al.*, 2016), including systems coupled by quantum dots (Deng *et al.*, 2016, 2017), have shown promising signatures of MBSs. Further, experimental progress towards the realization of phase-coherent transport in the semiconductor-superconductor platforms hosting Majorana devices was motivated also by our work, and has been achieved by Gazibegovic *et al.* (2017); Vaitiekėnas *et al.* (2018). This includes directly-grown, complex 1D TS wire network systems (Zhang *et al.*, 2018), MBSs hosted in effective 1D channels that are gate-defined in a 2D hybrid architecture

(Nichele *et al.*, 2017), and a selectively grown 2D semiconductor network platform that can be extended essentially indefinitely (Krizek *et al.*, 2018). Our qubit and code network designs can freely be adapted to such settings, cf. the discussion of the 2D materials platform in Hell *et al.* (2017b,a). With these and further near-term experimental advances, an integrated-circuit version of Majorana devices moves into closer reach. If the fundamental units work reasonably well, a fully scalable Majorana code network based on selectively-grown 2D architectures may thus be realized in the not-too-far future.

Depending on results of ongoing experiments, many avenues of future research are open and further work is to be done. Certainly, a more detailed analysis of realistic Majorana hardware platforms is needed towards the realization of Majorana-based topological qubits. Hybrid semiconductor-superconductor systems generally are difficult to simulate in numerics, but guidance from theory is needed for the engineering of advanced network systems. In order to make useful quantitative predictions, the necessary level of detail in materials and hardware simulation is far beyond analytical methods. Examples for such simulations include the decay- and dephasing-mechanisms in Majorana boxes, and the characterization of these qubit properties from conductance or spectroscopic measurements.

As an outlook, we hope to extend insights from our detailed investigations of transport in Majorana devices to further useful applications in Majorana-based qubits. An interesting task for future research is the engineering of protected, passive mechanisms that suppress the generation of errors in Majorana-based QECCs. Similar ideas were put forward by Bardyn and Karzig (2016), but in a rather abstract setting and using a complicated driven-dissipate mechanism with additional coupled ancilla qubits. A relevant question is how far one can simplify their scheme, e.g., using leads or quantum dots (with resonators) that are selectively coupled to Majorana boxes in a code network. If it is possible to achieve passive error-suppression that reduces the need for active stabilizer readout in the MSC architecture, this would be a major step towards feasibility of large-scale QECCs.
Thermodynamic properties of the isolated Majorana surface code system were discussed in Terhal *et al.* (2012); Roy *et al.* (2017), and aspects of error correction for quantum memories at finite temperature are reviewed in Terhal (2015); Brown *et al.* (2016).

Bibliography

Aasen, D., M. Hell, R. V. Mishmash, A. Higginbotham, J. Danon, M. Leijnse, T. S. Jespersen, J. A. Folk, C. M. Marcus, K. Flensberg, and J. Alicea (2016), Phys. Rev. X **6**, 031016.

Aharonov, Y., and D. Bohm (1959), Phys. Rev. **115**, 485.

Aharonov, Y., and A. Casher (1984), Phys. Rev. Lett. **53**, 319.

Albrecht, S. M., A. P. Higginbotham, M. Madsen, F. Kuemmeth, T. S. Jespersen, J. Nygård, P. Krogstrup, and C. M. Marcus (2016), Nature **531** (7593), 206.

Alicea, J. (2012), Reports on Progress in Physics **75** (7), 076501.

Alicea, J., Y. Oreg, G. Refael, F. Von Oppen, and M. P. Fisher (2011), Nature Physics **7** (5), 412.

Altland, A., and R. Egger (2013), Phys. Rev. Lett. **110**, 196401.

Altland, A., and B. D. Simons (2010), *Condensed matter field theory* (Cambridge University Press).

Amorim, C. S., K. Ebihara, A. Yamakage, Y. Tanaka, and M. Sato (2015), Phys. Rev. B **91**, 174305.

Bardyn, C.-E., and T. Karzig (2016), Phys. Rev. B **94**, 094303.

Beenakker, C. (2013), Annual Review of Condensed Matter Physics **4** (1), 113.

Béri, B. (2013), Phys. Rev. Lett. **110**, 216803.

Béri, B. (2017), Phys. Rev. Lett. **119**, 027701.

Béri, B., and N. R. Cooper (2012), Phys. Rev. Lett. **109**, 156803.

Bonderson, P., M. Freedman, and C. Nayak (2008a), Phys. Rev. Lett. **101**, 010501.

Bonderson, P., M. Freedman, and C. Nayak (2009), Annals of Physics **324** (4), 787 .

Bonderson, P., and R. M. Lutchyn (2011), Phys. Rev. Lett. **106**, 130505.

Bonderson, P., K. Shtengel, and J. Slingerland (2008b), Annals of Physics **323** (11), 2709 .

Bonderson, P., K. Shtengel, and J. K. Slingerland (2007), Phys. Rev. Lett. **98**, 070401.

Bravyi, S., D. P. DiVincenzo, and D. Loss (2011), Annals of physics **326** (10), 2793.

Bravyi, S., and A. Kitaev (2005), Phys. Rev. A **71**, 022316.

Bravyi, S., B. M. Terhal, and B. Leemhuis (2010), New Journal of Physics **12** (8), 083039.

Briegel, H. J., D. E. Browne, W. Dür, R. Raussendorf, and M. Van den Nest (2009), Nature Physics **5** (1), 19.

Brown, B. J., D. Loss, J. K. Pachos, C. N. Self, and J. R. Wootton (2016), Rev. Mod. Phys. **88**, 045005.

Bruus, H., and K. Flensberg (2016), *Many-body quantum theory in condensed matter physics: an introduction* (Oxford university press).

Cheng, M., V. Galitski, and S. Das Sarma (2011), Phys. Rev. B **84**, 104529.

Clarke, D. J., J. D. Sau, and S. Das Sarma (2016), Phys. Rev. X **6**, 021005.

Clarke, D. J., J. D. Sau, and S. Tewari (2011), Phys. Rev. B **84**, 035120.

Deng, M., S. Vaitiekénas, E. Prada, P. San-Jose, J. Nygård, P. Krogstrup, R. Aguado, and C. Marcus (2017), arXiv preprint arXiv:1712.03536 .

Deng, M. T., S. Vaitiekenas, E. B. Hansen, J. Danon, M. Leijnse, K. Flensberg, J. Nygård, P. Krogstrup, and C. M. Marcus (2016), Science **354** (6319), 1557.

Dirac, P. A. M. (1934), Mathematical Proceedings of the Cambridge Philosophical Society **30** (2), 150–163.

Dua, A., B. Malomed, M. Cheng, and L. Jiang (2018), arXiv preprint arXiv:1803.05886 .

Emery, V. J., and S. Kivelson (1992), Phys. Rev. B **46**, 10812.

Fabrizio, M., A. O. Gogolin, and P. Nozières (1995), Phys. Rev. B **51**, 16088.

Fendley, P. (2012), Journal of Statistical Mechanics: Theory and Experiment **2012** (11), P11020.

Flensberg, K. (2011), Phys. Rev. Lett. **106**, 090503.

Fowler, A. G., M. Mariantoni, J. M. Martinis, and A. N. Cleland (2012), Phys. Rev. A **86**, 032324.

Freedman, M., A. Kitaev, M. Larsen, and Z. Wang (2003), Bulletin of the American Mathematical Society **40** (1), 31.

Fu, L. (2010), Phys. Rev. Lett. **104**, 056402.

Fu, L., and C. L. Kane (2008), Phys. Rev. Lett. **100**, 096407.

Gangadharaiah, S., B. Braunecker, P. Simon, and D. Loss (2011), Phys. Rev. Lett. **107**, 036801.

Gau, M., S. Plugge, and R. Egger (2018), Phys. Rev. B **97**, 184506.

Gazibegovic, S., D. Car, H. Zhang, S. C. Balk, J. A. Logan, M. W. de Moor, M. C. Cassidy, R. Schmits, D. Xu, G. Wang, *et al.* (2017), Nature **548** (7668), 434.

Gogolin, A. O., A. A. Nersesyan, and A. M. Tsvelik (2004), *Bosonization and strongly correlated systems* (Cambridge university press).

Gottesman, D. (1997), *Stabilizer codes and quantum error correction*, Ph.D. thesis (California Institute of Technology).

Gottesman, D. (1998), arXiv preprint quant-ph/9807006 .

Gottesman, D. (2010), in *Quantum information science and its contributions to mathematics, Proceedings of Symposia in Applied Mathematics*, Vol. 68, pp. 13–58.

Haldane, F. (1981a), Journal of Physics C: Solid State Physics **14** (19), 2585.

Haldane, F. D. M. (1981b), Phys. Rev. Lett. **47**, 1840.

Hassler, F., A. R. Akhmerov, and C. W. J. Beenakker (2011), New Journal of Physics **13** (9), 095004.

Hassler, F., A. R. Akhmerov, C.-Y. Hou, and C. W. J. Beenakker (2010), New Journal of Physics **12** (12), 125002.

Hastings, M. B. (2017), ArXiv e-prints arXiv:1703.00612 [quant-ph] .

van Heck, B., A. R. Akhmerov, F. Hassler, M. Burrello, and C. W. J. Beenakker (2012), New Journal of Physics **14** (3), 035019.

Heisenberg, W. (1934), Zeitschrift für Physik **90** (3), 209.

Hell, M., K. Flensberg, and M. Leijnse (2017a), Phys. Rev. B **96**, 035444.

Hell, M., M. Leijnse, and K. Flensberg (2017b), Phys. Rev. Lett. **118**, 107701.

Herviou, L., K. Le Hur, and C. Mora (2016), Phys. Rev. B **94**, 235102.

Hoffman, S., C. Schrade, J. Klinovaja, and D. Loss (2016), Phys. Rev. B **94**, 045316.

Horodecki, R., P. Horodecki, M. Horodecki, and K. Horodecki (2009), Rev. Mod. Phys. **81**, 865.

Hützen, R., A. Zazunov, B. Braunecker, A. L. Yeyati, and R. Egger (2012), Phys. Rev. Lett. **109**, 166403.

Hyart, T., B. van Heck, I. C. Fulga, M. Burrello, A. R. Akhmerov, and C. W. J. Beenakker (2013), Phys. Rev. B **88**, 035121.

Ivanov, D. A. (2001), Phys. Rev. Lett. **86**, 268.

Jiang, L., C. L. Kane, and J. Preskill (2011), Phys. Rev. Lett. **106**, 130504.

Karzig, T., C. Knapp, R. M. Lutchyn, P. Bonderson, M. B. Hastings, C. Nayak, J. Alicea, K. Flensberg, S. Plugge, Y. Oreg, C. M. Marcus, and M. H. Freedman (2017), Phys. Rev. B **95**, 235305.

Karzig, T., Y. Oreg, G. Refael, and M. H. Freedman (2016), Phys. Rev. X **6**, 031019.

Karzig, T., F. Pientka, G. Refael, and F. von Oppen (2015a), Phys. Rev. B **91**, 201102.

Karzig, T., A. Rahmani, F. von Oppen, and G. Refael (2015b), Phys. Rev. B **91**, 201404.

Karzig, T., G. Refael, and F. von Oppen (2013), Phys. Rev. X **3**, 041017.

Kashuba, O., and C. Timm (2015), Phys. Rev. Lett. **114**, 116801.

Kitaev, A. (2003), Annals of Physics **303** (1), 2 .

Kitaev, A. (2006), Annals of Physics **321** (1), 2 .

Kitaev, A. Y. (2001), Physics-Uspekhi **44** (10S), 131.

Knapp, C., M. Zaletel, D. E. Liu, M. Cheng, P. Bonderson, and C. Nayak (2016), Phys. Rev. X **6**, 041003.

Krizek, F., J. E. Sestoft, P. Aseev, S. Marti-Sanchez, S. Vaitiekenas, L. Casparis, S. A. Khan, Y. Liu, T. Stankevic, A. M. Whiticar, A. Fursina, F. Boekhout, R. Koops, E. Uccelli, L. P. Kouwenhoven, C. M. Marcus, J. Arbiol, and P. Krogstrup (2018), ArXiv e-prints arXiv:1802.07808 [cond-mat.mtrl-sci] .

Landau, L. A., S. Plugge, E. Sela, A. Altland, S. M. Albrecht, and R. Egger (2016), Phys. Rev. Lett. **116**, 050501.

Leijnse, M., and K. Flensberg (2011), Phys. Rev. Lett. **107**, 210502.

Leijnse, M., and K. Flensberg (2012a), Phys. Rev. B **86**, 104511.

Leijnse, M., and K. Flensberg (2012b), Semiconductor Science and Technology **27** (12), 124003.

Li, J., T. Yu, H.-Q. Lin, and J. You (2014), Scientific reports **4**, 4930.

Li, Y. (2016), Phys. Rev. Lett. **117**, 120403.

Lidar, D. A., and T. A. Brun (2013), *Quantum error correction* (Cambridge University Press).

Litinski, D., M. S. Kesselring, J. Eisert, and F. von Oppen (2017), Phys. Rev. X **7**, 031048.

Litinski, D., and F. von Oppen (2018), ArXiv e-prints arXiv:1801.08143 [cond-mat.mes-hall] .

Lutchyn, R., E. Bakkers, L. Kouwenhoven, P. Krogstrup, C. Marcus, and Y. Oreg (2017), arXiv preprint arXiv:1707.04899 .

Lutchyn, R. M., J. D. Sau, and S. Das Sarma (2010), Phys. Rev. Lett. **105**, 077001.

Majorana, E. (1937), Il Nuovo Cimento **14** (4), 171.

Manousakis, J., A. Altland, D. Bagrets, R. Egger, and Y. Ando (2017), Phys. Rev. B **95**, 165424.

Michaeli, K., L. A. Landau, E. Sela, and L. Fu (2017), Phys. Rev. B **96**, 205403.

Mourik, V., K. Zuo, S. M. Frolov, S. R. Plissard, E. P. A. M. Bakkers, and L. P. Kouwenhoven (2012), Science **336** (6084), 1003.

Mukunda, N., and R. Simon (1993), Annals of Physics **228** (2), 205 .

Nayak, C., M. P. A. Fisher, A. W. W. Ludwig, and H. H. Lin (1999), Phys. Rev. B **59**, 15694.

Nayak, C., S. H. Simon, A. Stern, M. Freedman, and S. Das Sarma (2008), Rev. Mod. Phys. **80**, 1083.

Nichele, F., A. C. C. Drachmann, A. M. Whiticar, E. C. T. O'Farrell, H. J. Suominen, A. Fornieri, T. Wang, G. C. Gardner, C. Thomas, A. T. Hatke, P. Krogstrup, M. J. Manfra, K. Flensberg, and C. M. Marcus (2017), Phys. Rev. Lett. **119**, 136803.

Nielsen, M. A., and I. Chuang (2010), *Quantum computation and quantum information* (AAPT).

Nilsson, J., A. R. Akhmerov, and C. W. J. Beenakker (2008), Phys. Rev. Lett. **101**, 120403.

Oreg, Y., G. Refael, and F. von Oppen (2010), Phys. Rev. Lett. **105**, 177002.

Pedrocchi, F. L., and D. P. DiVincenzo (2015), Phys. Rev. Lett. **115**, 120402.

Plugge, S., L. A. Landau, E. Sela, A. Altland, K. Flensberg, and R. Egger (2016a), Phys. Rev. B **94**, 174514.

Plugge, S., A. Rasmussen, R. Egger, and K. Flensberg (2017), New Journal of Physics **19** (1), 012001.

Plugge, S., A. Zazunov, E. Eriksson, A. M. Tsvelik, and R. Egger (2016b), Phys. Rev. B **93**, 104524.

Plugge, S., A. Zazunov, P. Sodano, and R. Egger (2015), Phys. Rev. B **91**, 214507.

Preskill, J. (2018), *Lecture notes for physics 229: Quantum information and computation* (California Institute of Technology).

Read, N., and D. Green (2000), Phys. Rev. B **61**, 10267.

Roy, A., B. M. Terhal, and F. Hassler (2017), Phys. Rev. Lett. **119**, 180508.

Samuel, J., and R. Bhandari (1988), Phys. Rev. Lett. **60**, 2339.

Sau, J. D., D. J. Clarke, and S. Tewari (2011), Phys. Rev. B **84**, 094505.

Scheurer, M. S., and A. Shnirman (2013), Phys. Rev. B **88**, 064515.

Sekania, M., S. Plugge, M. Greiter, R. Thomale, and P. Schmitteckert (2017), Phys. Rev. B **96**, 094307.

Snizhko, K., R. Egger, and Y. Gefen (2018), Phys. Rev. B **97**, 081405.

Stoudenmire, E. M., J. Alicea, O. A. Starykh, and M. P. Fisher (2011), Phys. Rev. B **84**, 014503.

Terhal, B. M. (2015), Rev. Mod. Phys. **87**, 307.

Terhal, B. M., F. Hassler, and D. P. DiVincenzo (2012), Phys. Rev. Lett. **108**, 260504.

TU Delft, ., A. Akhmerov, J. D. Sau, *et al.* (2018), TU Delft, Topology in Condensed Matter (TOPOCMx) online course .

Vaitiekėnas, S., A. Whiticar, M. Deng, F. Krizek, J. Sestoft, S. Marti-Sanchez, J. Arbiol, P. Krogstrup, L. Casparis, and C. Marcus (2018), arXiv preprint arXiv:1802.04210 .

Vijay, S., and L. Fu (2016a), Physica Scripta **2016** (T168), 014002.

Vijay, S., and L. Fu (2016b), Phys. Rev. B **94**, 235446.

Vijay, S., and L. Fu (2017), ArXiv e-prints arXiv:1703.00459 [cond-mat.mes-hall] .

Vijay, S., T. H. Hsieh, and L. Fu (2015), Phys. Rev. X **5**, 041038.

Von Delft, J., and H. Schoeller (1998), arXiv preprint cond-mat/9805275 .

Wang, Z., X.-Y. Hu, Q.-F. Liang, and X. Hu (2013), Phys. Rev. B **87**, 214513.

Wilson, K. G. (1975), Rev. Mod. Phys. **47**, 773.

Xu, C., and L. Fu (2010), Phys. Rev. B **81**, 134435.

Yi, H. (2002), Phys. Rev. B **65**, 195101.

Yi, H., and C. L. Kane (1998), Phys. Rev. B **57**, R5579.

Zazunov, A., A. Altland, and R. Egger (2014), New Journal of Physics **16** (1), 015010.

Zazunov, A., A. L. Yeyati, and R. Egger (2011), Phys. Rev. B **84**, 165440.

Zee, A. (2016), *Group theory in a nutshell for physicists* (Princeton University Press).

Zhang, H., C.-X. Liu, S. Gazibegovic, D. Xu, J. A. Logan, G. Wang, N. van Loo, J. D. S. Bommer, M. W. A. de Moor, D. Car, R. L. M. Op het Veld, P. J. van Veldhoven, S. Koelling, M. A. Verheijen, M. Pendharkar, D. J. Pennachio, B. Shojaei, J. S. Lee, C. J. Palmstrøm, E. P. A. M. Bakkers, S. D. Sarma, and L. P. Kouwenhoven (2018), Nature , EP .

Acknowledgements

I would like to thank the following persons for supervision, guidance and collaborations during my time as PhD student at HHU Düsseldorf and my stay at NBI/QDev Copenhagen.

- Prof. Dr. Reinhold Egger, for his close supervision and guidance not only during my PhD, but also as Bachelor and Master student. Equally for his useful advice, and for the patience whenever I ignored this advice and sought my own way to understand a problem. Most of all, for the academic and personal freedom in pursuing a PhD under his watch, including him making possible an extended stay in Copenhagen and exceedingly many visits to interesting conferences and meetings all over the world.

- All present and former members of the Institut für Theoretische Physik IV at HHU, where I completed my PhD. Dr. Alex Zazunov and Dr. Francesco Buccheri, for many helpful discussions on technical aspects of condensed-matter theory. Also Dr. Laura Cohnitz, a long-term fellow PhD student, for sharing the struggles of academic life.

- The members of Institut für Theoretische Physik III at HHU, for many interesting discussions on quantum information theory. Especially Dr. Hermann Kampermann, for his mentorship before and during all of my PhD, for time invested in lectures on advanced quantum information theory, and for reminding that quantum computers in all likeliness will not work out in the end.

- Prof. Dr. Alexander Altland, Dr. Eran Sela and Aviad Landau, for many interesting and lively discussions during our great collaborations and beyond.

- Prof. Karsten Flensberg, Prof. Charles Marcus, and the whole team at NBI/QDev, for welcoming me during an extended research stay in Copenhagen, and for allowing me to participate in many fun social events. In particular Karsten for his close guidance and supervision, and Charlie for adopting me as a quasi-experimentalist in many interesting meetings of his great research team. Also Esben Bork-Hansen and the lunch club at NBI for great food and a relaxing atmosphere.

- The team at Station Q Santa Barbara et al., for several pleasant visits, meetings and discussions, during which I learned much about topological quantum computation.

- My parents Inge and Heinz Plugge, and my sister Christina Plugge (Dr. Tinti), most importantly, for invaluable support throughout my studies and in all aspects of life.

Selbstständigkeitserklärung

Ich versichere an Eides Statt, dass die Dissertation von mir selbständig und ohne unzulässige fremde Hilfe unter Beachtung der “Grundsätze zur Sicherung guter wissenschaftlicher Praxis an der Heinrich-Heine-Universität Düsseldorf” erstellt worden ist.
Weiterhin erkläre ich, dass ich die Dissertation keiner anderen Fakultät bereits vorgelegt habe und keinerlei vorherige erfolglose Promotionsversuche vorliegen. Darüber hinaus ist mir bekannt, dass jedweder Betrugsversuch zum Nichtbestehen oder zur Aberkennung der Prüfungsleistung führen kann.

Düsseldorf, den 15.06.2018

(Stephan Plugge)

Publications

Here I append references to all publications that are included in this thesis. For each work, I give the full bibliographical information and a short description of my contributions to the research.
The papers are sorted according to their appearance in the main body of the thesis:

- Appendix A.1, with Sekania *et al.* (2017), discussed in Chapter 2.3,
- Appendix A.2, with Plugge *et al.* (2015), discussed in Chapter 2.4,
- Appendices B.1,B.2, with Plugge *et al.* (2016b); Gau *et al.* (2018), in Chapter 3.3,
- Appendices C.1,C.2, with Plugge *et al.* (2017); Karzig *et al.* (2017), in Chapter 4.2,
- Appendices C.3,C.4, with Landau *et al.* (2016); Plugge *et al.* (2016a), in Chapter 4.4.

A.1 Braiding errors in interacting Majorana quantum wires

M. Sekania, S. Plugge, M. Greiter, R. Thomale, and P. Schmitteckert, *Braiding errors in interacting Majorana quantum wires*, Phys. Rev. B **96**, 094307 (2017).
Journal: Physical Review B; Impact Factor 2016: 3.836
Contribution: co-author, scientific work/discussions, preparation of the manuscript [20%]
Detailed analysis of braiding in interacting Kitaev chain Y-junctions, including calculation of geometric phases on numerically exact basis. My contributions include analysis of numerical data, reaching an effective understanding of where errors and deviations from naively expected results originate from, and discussion of the implications for Majorana-based qubits and quantum information processing in preparation of the manuscript.

A.2 Majorana entanglement bridge

S. Plugge, A. Zazunov, P. Sodano, and R. Egger, *Majorana entanglement bridge*, Phys. Rev. B **91**, 214507 (2015). [Selected as *Editors' Suggestion*]
Journal: Physical Review B; Impact Factor 2015: 3.718
Contribution: first author, scientific work and preparation of the manuscript [80%/20%]
Introductory work on mescoscopic Majorana fermion devices and their potential for quantum information processing - related applications. Most of the work was performed during my master thesis project. Finalizing the project, and the writing and submission of the manuscript took part during my time as doctoral student (estimated 20% of total work).

B.1 Kondo physics from quasiparticle poisoning in Majorana devices

S. Plugge, A. Zazunov, E. Eriksson, A.M. Tsvelik, and R. Egger, *Kondo physics from quasiparticle poisoning in Majorana devices*, Phys. Rev. B **93**, 104524 (2016).
Journal: Physical Review B; Impact Factor 2016: 3.836
Contribution: first author, scientific work and preparation of the manuscript [50%]
Investigation of quantum transport phenomena in multi-terminal Majorana islands connected by normal-conducting leads, in particular including spurious low-energy states ("quasi-particle poisoning") on the island. My contribution includes analysis of the low-energy properties of the system via renormalization-group methods, followed by numerical simulation and solution of the renormalization-group equations. Finally, we confirmed the perturbative results by an explicit strong-coupling solution.

B.2 Quantum transport in coupled Majorana box systems

M. Gau, S. Plugge, and R. Egger, *Quantum transport in coupled Majorana box systems*, Phys. Rev. B **97**, 184506 (2018). [Selected as *Editors' Suggestion*]
Journal: Physical Review B; Impact Factor 2016: 3.836
Contribution: shared first author, scientific work, preparation of the manuscript [40%]
General investigation of quantum transport in coupled Majorana boxes contacted by normal-conducting leads, including several examples with direct relevance for near-term topological qubit and code network implementations. My contributions include analysis of the system via renormalization-group methods, numerical simulation and solutions of the RG equations, and the formulation of a strong-coupling approach and solutions. Further I performed transport calculations for one example device, including the use of the full counting statistics method. Also I supervised M. Gau during all stages of the project.

C.1 Majorana box qubits

S. Plugge, A. Rasmussen, R. Egger, and K. Flensberg, *Majorana box qubits*, New J. Phys. **19** 012001 (2017). [Fast-Track Communication; selected for "Highlights of 2017" collection]
Journal: New Journal of Physics; Impact Factor 2016: 3.786
Contribution: first author, scientific work and preparation of the manuscript [70%]
Hardware- and application-oriented work on Majorana-based topological qubits and quantum computation, including hands-on recipes for experimental implementation of such "Majorana box qubits". My contributions include the design, analysis and discussion of all presented readout schemes and multi-qubit networks. All layouts were drafted in close feedback and collaboration with experimentalists in Copenhagen.

C.2 Scalable Designs for Quasiparticle - Poisoning - Protected Topological Quantum Computation with Majorana Zero Modes

T. Karzig, C. Knapp, R. Lutchyn, P. Bonderson, M. Hastings, C. Nayak, J. Alicea, K. Flensberg, S. Plugge, Y. Oreg, C. Marcus, and M. H. Freedman, *Scalable Designs for Quasiparticle-Poisoning-Protected Topological Quantum Computation with Majorana Zero Modes*, Phys. Rev. B **95**, 235305 (2017). [Featured in *Physics*]
Journal: Physical Review B; Impact Factor 2016: 3.836
Contribution: co-author, scientific work/discussions, comments on the manuscript [5%]
Extensions of Majorana-based topological quantum computation and error correction, beyond Majorana surface code or simple qubit networks. In particular, including a comparison of various qubit design, readout and network construction approaches, and a resource-cost/gain analysis depending on system properties. My contributions include design suggestions and discussion for the topological qubits and readout modes, and of the "experimental next steps" in form of minimal proof-of-principle Majorana experiments.

C.3 Towards realistic implementations of a Majorana surface code

L.A. Landau, S. Plugge, E. Sela, A. Altland, S.M. Albrecht, and R. Egger, *Towards realistic implementations of a Majorana surface code*, Phys. Rev. Lett. **116**, 050501 (2016).
Journal: Physical Review Letters; Impact Factor 2016: 8.462
Contribution: shared first author, scientific work and preparation of the manuscript [40%]
High-impact article on practical readout and manipulation schemes of Majorana-based

qubit networks, with direct applicability towards topological quantum error correction schemes (here: surface code). My contributions include the development and analysis of conductance readout and SET/quantum-dot manipulation schemes, connecting these to topological properties of the code and to higher-level quantum-information-processing concepts, and finding near-term viable ideas for experimental integration (with Sven Albrecht).

C.4 Roadmap to Majorana surface codes

S. Plugge, L.A. Landau, E. Sela, A. Altland, K. Flensberg, and R. Egger, *Roadmap to Majorana surface codes*, Phys. Rev. B **94**, 174514 (2016). [Selected as *Editors' Suggestion*]
Journal: Physical Review B; Impact Factor 2016: 3.836
Contribution: first author, scientific work and preparation of the manuscript [75%]
Extension of earlier work (Landau et al., PRL 2016), including detailed discussion of quantum-information processing prospects in networks of mesoscopic Majorana islands. My contribution includes the detailed analysis, adaptation and implementation of quantum computation and quantum error-correction concepts on basis of the surface code approach. Additionally, I designed the tailored routine of how to prepare approximate T-gate ancilla states which are necessary to implement a universal gate set, and contributed to discussion of possible error sources in Majorana-based error correcting codes.